University of California
Santa Barbara

The Influence of High Doping on Electronic and Optical Properties in Tungsten Oxide

A dissertation submitted in partial satisfaction
of the requirements for the degree

Doctor of Philosophy
in
Materials

by

Wennie Wang

Committee in charge:

Professor Chris G. Van de Walle, Chair
Professor S. James Allen
Professor Ram Seshadri
Professor Susanne Stemmer

June 2018

The Dissertation of Wennie Wang is approved.

Professor S. James Allen

Professor Ram Seshadri

Professor Susanne Stemmer

Professor Chris G. Van de Walle, Committee Chair

June 2018

The Influence of High Doping on Electronic and Optical Properties in Tungsten Oxide

Acknowledgements

I would like to express my sincere gratitude to those who made this work possible. First is my advisor, Prof. Chris G. Van de Walle, from whom I have learned so much in the past few years since starting my graduate studies. Chris has taught me many valuable skills, such as approaching research with attention to fine details, looking out for inconsistencies, and always having a healthy amount of skepticism. He has pushed me to become a better scientist, researcher, communicator, and writer, and for that I am deeply grateful to have had the opportunity to work with and learn from him.

Additionally, I would like to thank my research committee for their feedback and advice; especially to Prof. Ram Seshadri for always keeping me on my toes and having research insights every time I visit; to Prof. Susanne Stemmer for serving as the Committee Co-chair; and to Prof. S. James Allen for always having an open office door, and giving guidance and wisdom on various research challenges we encountered along the way.

I am also particularly grateful to Prof. Anderson Janotti and Dr. Cyrus Dreyer who provided much in mentorship and encouragement when I started, especially when I did not have the confidence to believe in my own abilities. Both were always welcoming, ready to answer questions and help with day-to-day challenges.

On a day-to-day basis, I have had the great fortune to interact with a great number of extraordinary researchers and people. All the postdocs I have met had so much to share, and I always learn a considerable amount each time I talk with them. This has lead to productive collaborations with Drs. Hartwin Peelaers, Xie Zhang, Youngho Kang, and Burak Himmetoglu, who have helped me become more knowledgeable in a variety of condensed matter concepts. Due recognition goes to also Drs. Daniel Steiauf, John L. Lyons, Darshana Wickramarante, Zhen Zhou, Leigh Weston, Audrius Alkauskus,

Khang Hoang, and José Padilha who have given me invaluable advice both in and out of research.

Current and past students have also significnatly enriched my time at UCSB. They have been integral to the my graduate experience. Especially thanks to Karthik Krishnaswamy and Jimmy-Xuan Shen, who mentored me as older students and with whom I have had the privlege of collaborating. Special thanks for the fruitful and lively discussions to: Lars Bjaalie, Luke Gordon, Patrick McBride, Nicholas Adamski, Andrew Rowberg, Michael Swift, Mark Turiansky, and Azzedin "Azi" Jackson.

I would also like to express my gratitude to Dr. Yingge Du, Prof. Martin Moskovits, and Katherine Kanipe who took the time to help with and teach me about Raman measurements of oxide heterostructures. Through them I was given the opportunity to experience being an experimentalist.

My PhD would not have been possible without the support of funding agencies and supercomputing facilities. Thank you to the Department of Energy, National Science Foundation Graduate Research Fellowship Program, UCSB Institute of Energy Efficiency, and UCSB Materials Research Laboratory for providing financial support. Thank you to also those at UCSB CSC, NERSC, XSEDE, and Department of Defense for providing the computational infrastructure and clusters.

I would next like to acknowledge the various student organizations, which have given me a great deal of encouragement and sense of community here at UCSB. First is the UCSB ScienceLine coordinator Claudia Mazzotti, who always has words of encouragement and positivity, and who tirelessly gives educational access to local schools. Second are people I had the opportunity to travel with for the TMS DMMM1 and DMMM2 conference on diversity in the STEM fields: Gesine Veits, Victoria Miller, Chandra Macauley, and Natalie Larson. They became role models for me in not only becoming a scientific expert, but also mentoring to shape and encourage future scientists. Particular

thanks to also Prof. Tresa Pollock, who provided the faculty and financial support that made attending even possible and who always has an open office and ears to student input. Third are my peers who joined me in the endeavor to create and teach MAT 188, an undergraduate course on energy in materials technologies: Chandra Macauley, Mandi Buffon, and Michael Ford. I could not have done it without them, and am extremely proud of the class we created.

Next, I would like to express my gratitude to those in the organizing committees of UCSB Graduate Students for Diversity in Science (GSDS): Matthew Gebbie, Saemi Oh-Poelma, and Niva Ran who encouraged me to take on leadership roles and grow GSDS into a more prominent student organization on campus. This of course would not have been possible without the dedication and efforts of those with whom I had the pleasure of working: Emre Discekici, Anna Melker, Clayton Cozzan, Doug Fabini, Menaka Wilhelm, Megan Butala, Chelsea Catania, David Cao, among others whose names would fill many pages.

I am deeply grateful for my time with the UCSB Beyond Academia organizing committee for being one of the most functional, organized, and rewarding groups to work with: Steve Brown, Tanya Das, Rebecca Reitz, Philip Vieira, Emma Parker, Shawn Warner-Garcia, Chris Freeze, Christina Shin, Jessica LeClair, David Hwang, Leihua Ye, Vicky Ballmes, Brandon Isaac, Daniel Boulos, Noreen Balos, Rafael Melendez-Rios, and the next generation, Matthew Wong and Rhiannon Kennard. Particular thanks to Robert Hamm, Arica Lubin, and Lana Smith-Hale for creating the opportunity and providing constant support, insight, and advice.

Finally, I am forever grateful to my family and especially parents, Hankun Wang who taught me early to appreciate STEM before passing away and Xiaonan Yin who has since been a beacon of strength, support, and encouragement; and my sister Wenjia who will always be my favorite sister and role model.

Curriculum Vitæ

Wennie Wang

Education

2018	Ph.D. in Materials, University of California, Santa Barbara (UCSB).
2013	B.S in Materials Science and Engineering, Massachusetts Institute of Technology.

Publications

1. W. Wang, H. Peelaers, J.X. Shen, C.G. Van de Walle. "Carrier-Induced Absorption as a Mechanism for Electrochromism in WO_3." *Submitted*.
2. W. Wang, Y. Kang, H. Peelaers, K. Krishnaswamy, C.G. Van de Walle. "First-principles study of transport in WO_3." *In preparation*.
3. X. Zhang, J.X. Shen, W. Wang, C.G. Van de Walle. "Radiative recombination in halide perovskites." *Submitted*.
4. W. Wang, H. Peelaers, J.X. Shen, A. Janotti, C.G. Van de Walle, "First-principles characterization of defects in WO_3", Proc. SPIE 10533, Oxide-based Materials and Devices IX, 105332C (23 February 2018)
5. W. Wang, A. Janotti, C.G. Van de Walle. "Phase transformations upon doping in WO_3." J. Chem. Phys., **146**, 214504 (2017).
6. W. Wang, A. Janotti, C.G. Van de Walle. "Role of oxygen vacancies in crystalline WO_3." J. Mat Chem. C, **4**, 6641 6648 (2016).
7. F. Kaule, W. Wang, S. Schoenfelder. "Modeling and Testing the Mechanical Strength of Solar Cells." Solar Energy Materials and Solar Cells. **120A**, 441-447 (2014).
8. S.S. Wicks, W. Wang, M.R. Williams, B.L. Wardle. "Multi-scale interlaminar fracture mechanisms in woven composite laminates reinforced with aligned carbon nanotubes." Composites Science and Technology. **100**, 128-135 (2014).

Awards

2018	March Meeting of the American Physical Society (APS) Ken Hass Outstanding Student Paper Award Runner-up
2017-2018	Excellence in Research Fellowship, UCSB Institute for Energy Efficiency

2018	SPIE/MKS Instruments Research Excellence Travel Award
2017	Materials Research Society Fall 2017 Graduate Student Award finalist (Silver)
2016	UCSB Graduate Student Association Excellence in Teaching Award (nominated)
2016	APS Ovshinsky Travel Award Honorable Mention
2015, 2016	UCSB ScienceLine Certificate of Excellence
2015-2018	UCSB Materials Research Laboratory Travel Grant
2014-2018	National Science Foundation Graduate Research Fellowship
2013-2014	Holbrook Foundation Fellowship, UCSB Institute for Energy Efficiency

Invited Talks

2018	W. Wang. "Tuning the optical properties of complex oxides for energy applications." March Meeting of the American Physical Society, March 5-9, 2018. Los Angeles, CA, USA.
2018	W. Wang, H. Peelaers, J.X. Shen, C.G. Van de Walle. "Impact of point defects on electrochromism in WO_3." The International Society for Optics and Photonics (SPIE) OPTO, January 27-February 1, 2018. San Francisco, CA, USA.
2016	W. Wang. "MISTI-Germany: A student's perspective on international internships." Materials Science and Engineering Congress, 27-29 September 2016. Darmstadt, Germany.
2016	N.M. Larson, W. Wang, D. Hwang. "Highlights from the Transforming the Diversity Landscape Symposium: The Importance of Empathy on the Individual and Program Level." The Minerals, Metals and Materials Society (TMS) DMMM2, July 25-26, 2016. Northwestern University, Evanston, IL, USA.

Contibuted Talks

2018	W. Wang, Y. Kang, K. Krishnaswamy, C.G. Van de Walle. "Influence of spin-orbit coupling in transport of WO_3." March Meeting of the American Physical Society. March 5-9, 2018. Los Angeles, CA.
2017	W. Wang, H. Peelaers, J.X. Shen, C.G. Van de Walle. "Influence of Structural Distortions on Optical Absorption in WO_3." Materials Research Society Fall Meeting. November 26 December 2, 2017. Boston, MA.

2017	W. Wang, Y. Kang, K. Krishnaswamy, B. Himmetoglu, C.G. Van de Walle. "Electron-phonon interactions in transport properties of WO_3." March Meeting of the American Physical Society. March 13-18, 2017. New Orleans, LA.
2016	W. Wang, A. Janotti, C.G. Van de Walle. "Phase Transformations upon doping in WO_3." March Meeting of the American Physical Society. March 13-18, 2016. Baltimore, MD.
2016	W. Wang, A. Janotti, C.G. Van de Walle. "Impact of oxygen vacancies on electrochromic behavior in WO_3." 145th TMS Annual Meeting & Exhibition. Nashville, TN. February 14-18, 2016.
2015	W. Wang, A. Janotti, C.G. Van de Walle. "Insights into the oxygen vacancy in WO_3." 28th International Conference on Defects in Semiconductors. Espoo, Finland. July 27-31, 2015.
2015	W. Wang, A. Janotti, C.G. Van de Walle. "Uncovering the connection between dopants and defects in WO_3." Materials Research Society Spring Meeting. San Francisco, CA. April 6-10, 2015.
2014	W. Wang, A. Janotti, C.G. Van de Walle. "Understanding the Oxygen Vacancy in WO_3." March Meeting of the American Physical Society, San Antonio, TX. March 2-6, 2015.

Seminars/Workshops

2017	W. Wang and J.X. Shen. "Rapid fire MPI/OpenMP: A brief introduction to code parallelization." UCSB Graduate Simulation Seminar Series Workshop. September 2017.
2016	W. Wang. "Atom by atom: Understanding defects using first-principles calculations." UCSB Graduate Simulation Seminar Series. August 2016. Awarded and voted top seminar given.

Volunteering and Outreach

2014-2018	UCSB Graduate Students for Diversity in Science; President (2016-2017), Outreach Director (2015-2016)
2014-2018	UCSB ScienceLine
2016	TMS 2016 Annual Meeting and Exhibition: "Transforming the Diversity Landscape," Co-organizer and session chair
2015-2017	UCSB Beyond Academia co-founder, organizer, and finance committee chair

Abstract

The Influence of High Doping on Electronic and Optical Properties in Tungsten Oxide

by

Wennie Wang

Perovskites are a well-known class of materials with rich physics and a wide variety of applications. One such perovskite is tungsten oxide (WO_3), which is a well-known chromogenic material used in smart windows and other display technologies. Due to its open crystal structure, it is possible to incorporate high concentrations of dopants. In this dissertation, we seek to understand the influence of dopants on atomic and electronic structure, as well as transport and optical properties using density functional theory.

First, we examine alkali doping and incorporating the oxygen vacancy in cubic and monoclinic WO_3. We investigate the relative stabilities of different charge states and its implications on electrical properties, such as conductivity and electrochromism. Our results suggest that both alkali dopants and oxygen vacancies are shallow donors, and we discuss its implications for device development.

Next, we study the effect of charge doping. Tungsten trioxide has been experimentally shown to transform from the monoclinic symmetry to cubic symmetry with increasing monovalent doping. Our calculations show that electron doping primarily drives the phase transformation. We characterize the phase transformation from low to high symmetry, quantify the energetics of this transformation, and elucidate on the mechanism of these structural changes.

Building on our insights on the electronic behavior of dopants and defects, we study the influence of doping concentration on transport. Understanding the transport properties of these carriers is critical in many of the device applications for which WO_3 is

used. We investigate the role of electron-phonon scattering in electron transport, and discuss the effects of spin-orbit coupling.

Finally, we examine the influence of doping concentration and structural distortions on optical absorption. We explore crystalline and disordered structures to demonstrate why these structural changes can enhance absorption at a microscopic level. Carrier-induced direct absorption is shown to wholly explain the drop in transmittance and coloration in electrochromism. Our findings shed light on how electronic features can be optimized for improved display and energy technologies.

Contents

List of Figures

List of Tables

Chapter 1

Into the World of Complex Oxides

Discovering and understanding novel materials is a key tenet in materials science and engineering. This is particularly true for electronic materials, as electronic devices move beyond silicon and traditional III-V compounds into novel materials [1].

A large driving force for materials discovery and characterization is computation. Modern day computational materials science culminated with the development of quantum mechanics in the 1930s and computers in the late 20th century. The end of the 20th century saw the emergence of massively parallel supercomputers that broke the teraflop barrier, and just over a decade later, the petaflop barrier. These *in-silico* studies have lead to unprecedented computational insight into materials properties, allowing for a multitude of complex physical phenomena to be studied. Such computational advances have allowed for the accelerated exploration of many new materials with fascinating properties. This has allowed for extraordinary insight into materials, bridging theory and experiment.

In this dissertation, we study the subset of materials known as complex oxides. Complex oxides are called so, not necessarily because of their chemical composition so much as the rich and varied physics they exhibit. Displaying a variety of phenomena and

properties, such as sustaining unusually large charge densities [2, 3, 4], superconductivity [5], multiferroism [6], and metal-insulator transitions [7, 8], complex oxides hold substantial promise as next-generation materials in electronic devices. This dissertation contributes a small sliver to the ever-growing body of discoveries and understanding of complex oxides.

We consider oxides that can sustain high levels of dopant and carrier concentrations, and explore how such concentrations affect materials properties. One such perovskite oxide, tungsten oxide (WO_3), is the focus of this dissertation. We study the influence of defects and dopants on the transport and optical properties using first-principles methods based on density functional theory. In each chapter, we explore the atomistic origins of the observed trends and behaviors to come to a general understanding of how atomic, electronic, and vibronic structure interact and contribute to material properties.

The outline of this dissertation is constructed based on the following topics. We begin with a brief overview of the computational methodologies used, namely density functional theory (DFT) and *ab-initio* molecular dynamics in Chapter 2. This is followed by an overview of select topics on electronic behavior, including polaron formation and spin-orbit coupling, in Chapter 3. The remaining chapters are dedicated to the study and characterization of electronic and vibronic phenomena in WO_3. We start with a study on native and extrinsic point defects in Chapter 4, followed by an investigation of the effects of charge doping on structural phase transitions in Chapter 5. Building off these findings, the impact of spin-orbit coupling on transport is explored in Chapter 6 and the influence of structural distortions on optical absorption is presented in Chapter 7. Finally, we conclude with general insights and advancements in methodology and future prospects for further study. From this extended study of WO_3, we construct a broad understanding of the influence of doping on electronic, transport, and optical properties, which contributes to the general knowledge of complex oxides for electronic devices.

1.1 A Closer Look at WO_3

Perovskites are materials of the general chemical composition ABO_3, in which the A and B sites are occupied with metal cations. Of note are the transition metal perovskites, of which WO_3 is one example. A detailed account of the electronic structure of *d*-band perovskites with emphasis on using tight-binding for bonding intuition and representation of electronic states based on symmetry may be found in Ref. [9].

WO_3 is a perovskite in which the A-site atom is missing. It has been extensively studied for its electrochromic property [10, 11, 12, 13, 14], in which the transmittance in the infrared and visible frequencies can be controlled by intercalation of donor ions, such as Li, Na [15, 16, 17] and H [18]. It has also been considered as a functional material in gas sensing [19, 20], photocatalysis applications [21, 22], and as an electrode material in lithium-ion batteries [23]. More recently, it has been utilized in high-efficiency solar cells, where WO_3 serves as the electron transport layer [24].

We explore a variety of optical and electronic properties of WO_3. These include the influence of native and extrinsic defects, electronic transport, and optical absorption. While the results presented here are specific to WO_3, the insights and analyses are expected to cross-apply to related oxides and materials. The reader is encouraged to turn to Refs. [25, 26, 27, 28] as valuable resources for fundamentals in solid-state physics that will be used in the remainder of the dissertation.

1.2 Bulk Description of Properties in WO_3

We describe common calculation parameters in Section 2.6 and parameters specfic to each topic in each of the respective chapters. A short overview of density functional theory may be found in Chapter 2. Here, we begin with a description of the bulk

structural and electronic properties of WO_3, which serves as the starting context that the remaining chapters shall build upon.

WO_3 has essentially an ABO_3 perovskite structure but with the A site vacant (see Fig. 1.2). The B metal cation is surrounded octahedrally by oxygens, and these octahedra are allowed to distort and rotate. These distortions and rotations are intimately connected with the electronic structure and materials properties that manifest from that structure. A more in-depth study on the intimate connection between atomic and electronic properties is presented in Chapter 5, which elucidates the role of electron doping in phase transformations.

WO_3 exists in several phases at different temperatures. WO_3 is of Pc monoclinic symmetry below 230 K, at which point it becomes the $P\bar{1}$ triclinic phase. At room temperature, WO_3 takes on a different monoclinic phase with $P2_1/n$ symmetry until 600 K. Between 600 K and 1000 K, it has $Pmnb$ ($Pnma$) orthorhombic symmetry. Above 1000 K, WO_3 is tetragonal ($P4/ncc$ until 1170 K; $P4/nmm$ above 1170 K) [29].

Different phases of WO_3 differ by the extent to which the oxygen octahedra are distorted and the W atoms are off-center in the octahedra, as shown in the unit cells in Fig. 1.1. In the cubic phase, the W ions are centered in straight, upright octahedra of oxygens. In the tetragonal structure, the W ions are displaced in an alternating pattern along the [001] and [00$\bar{1}$] directions while the octahedra remain upright. In the orthorhombic phase, the tilting of the octahedra (i.e., ϕ_1 and ϕ_2) along $\hat{x}$ and $\hat{y}$ directions deviates from right angles and the W ions are offset from the center of the octahedra along non-Cartesian directions (e.g., [110]) in an alternating fashion. In the monoclinic phase, the W ions further displace along various directions and the octahedra are free to rotate, tilt, and distort along $\hat{x}$, $\hat{y}$, and $\hat{z}$ directions. The β angle, which is defined as the angle between the [100] and [001] lattice vectors, may take on values different from 90 degrees in the monoclinic phase. The rotations and tilts of octahedra corresponding to

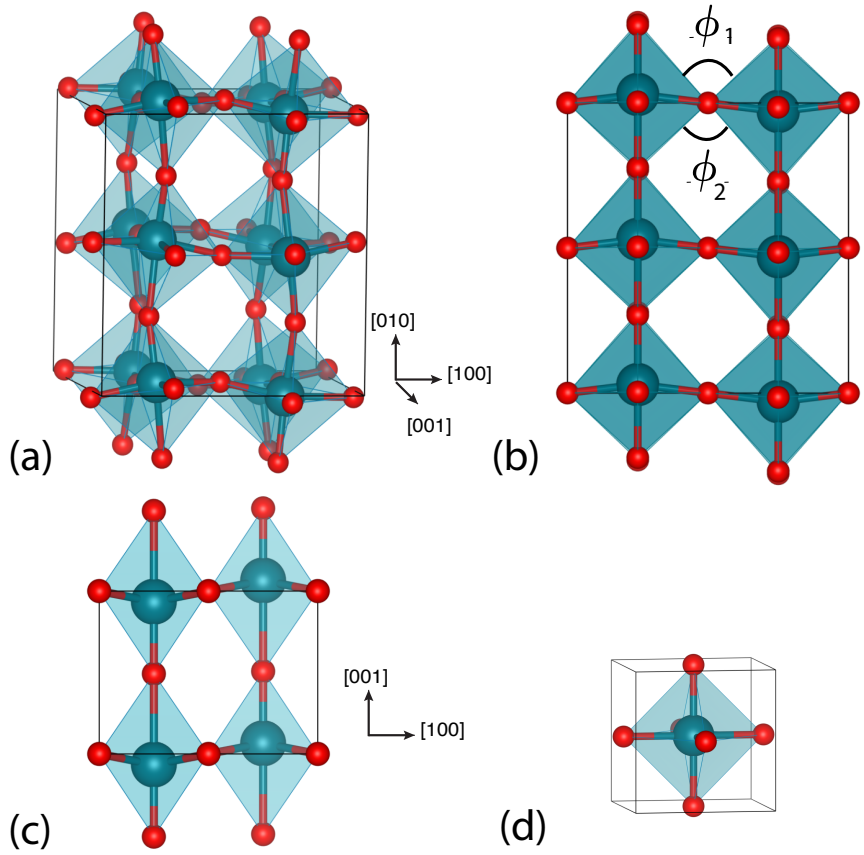

Figure 1.1: Unit cells of WO_3 in order of increasing symmetry: (a) room-temperature (RT) monoclinic (space group $P2_1/c$), (b) orthorhombic ($Pbcn$), (c) tetragonal ($P4/nmm$), and (d) cubic ($Pm\bar{3}m$). An example of the relative tilt angles ϕ_1 and ϕ_2 along $\hat{x}$ between octahedra is indicated; the tilt angles are similarly defined for $\hat{y}$ and $\hat{z}$.

the symmetry of the crystallographic space groups within Glazer notation [30] are well-documented for perovskites [31], including WO_3 [32]. The progression of these distortions as observed during the phase transformations is described in detail in Chapter 5. A thorough study of the various phonon modes that contribute to the structural distortions in WO_3 may be found in Ref. [33].

Our calculated lattice parameters and band gaps for the unit cells of different phases shown in Fig. 1.1 are listed in Table 1.2. The structural parameters as calculated compare well to experimental values. They also agree with previous calculations [34] to within

Table 1.1: Experimental and calculated lattice parameters and band gaps for WO_3; "ind" indicates indirect, "dir" direct band gaps. For calculated indirect gaps, the location of the valence-band maximum (VBM) and conduction-band minimum (CBM) in the Brillouin zone is indicated as (ind: VBM, CBM).

	a (Å)	b (Å)	c (Å)	β (°)	E_g (eV)
RT Monoclinic, $P2_1/c$					
Exp.[a]	7.31	7.54	7.69	90.90	2.6-2.8 (ind)
HSE	7.41	7.63	7.79	90.15	2.56 (dir: Γ)
Orthorhombic, $Pbcn$					
Exp.[b]	7.36	7.57	7.76	90.00	—
HSE	7.43	7.64	7.79	90.00	2.49
Tetragonal, $P4/nmm$					
Exp.[c]	5.25	5.25	3.91	90.00	—
HSE	5.29	5.29	3.96	90.00	1.53 (ind: Z, Γ)
Cubic, $Pm\bar{3}m$					
Exp.[d]	3.78	3.78	3.78	90.00	—
HSE	3.79	3.79	3.79	90.00	1.53 (ind: R, Γ)

[a] References [35, 36, 37, 38]. [b] Reference [39].
[c] Reference [40]. [d] References [15] and [41].

0.5%. Electronic band structures for the different phases are shown in Fig. 1.2.

In the electronic structure of WO_3, the conduction bands are composed primarily of $5d$ states (which is typical of many transition metal oxides), whereas the valence bands are primarily of O $2p$ character. A more general look into electronic structure of d-band perovskites is given in Ref. [9]. The octahedral environment of the W leads to crystal field splitting of the d-band states, which are degenerate in the isolated atom. In the cubic symmetry, which is free of internal structural distortions, this octahedral environment leads the d states to split into the lower-lying triply-degenerate t_{2g} states and higher-lying doubly-degenerate e_g states (at Γ). This crystal-field splitting is clearly seen in Fig. 1.2(d). Nevertheless, this splitting of the d-band states is more or less preserved in the t_{2g}-like and e_g-like bands, as seen in the clustering of bands in Fig. 1.2(a-c) for

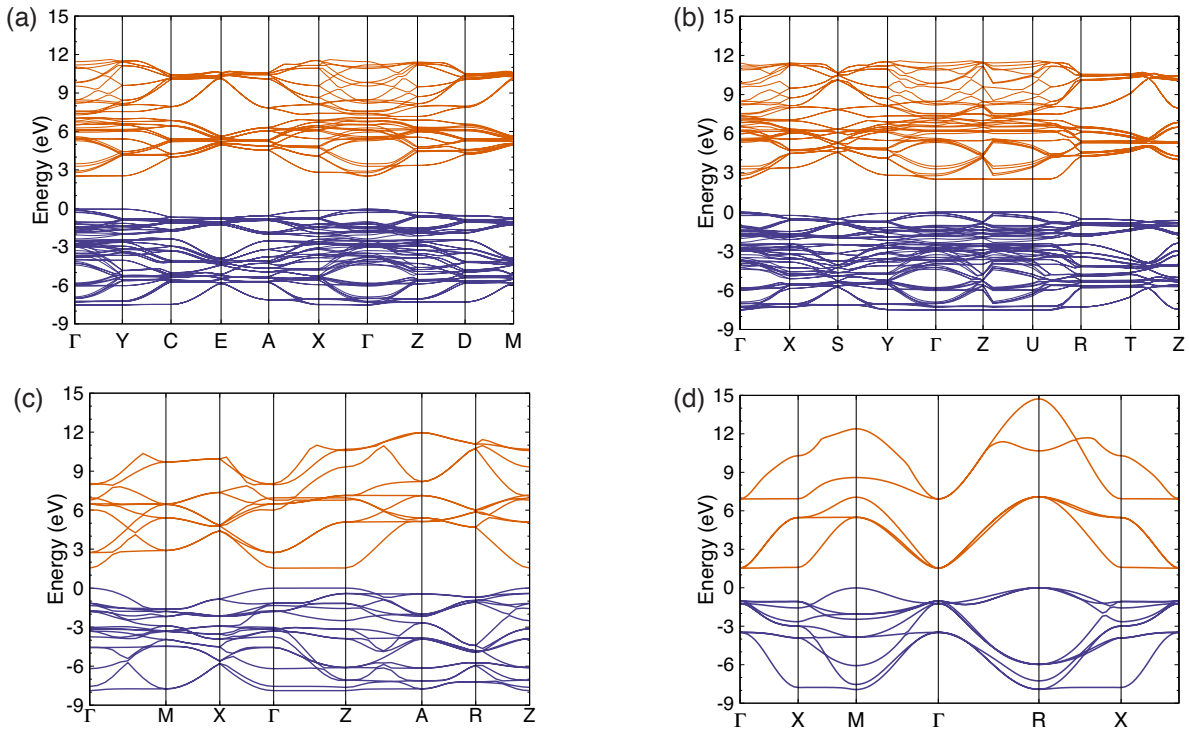

Figure 1.2: Calculated band structures for different phases of WO_3: (a) room-temperature (RT) monoclinic, (b) orthorhombic, (c) tetragonal, and (d) cubic.

lower symmetry phases. The shrinking band width of the conduction bands among the phases of WO_3 contributes to an increase in band gap as the symmetry is lowered. The cubic phase symmetry maximizes hybridizations and band dispersion, leading to the largest band width (13.2 eV) and smallest band gap (1.53 eV). As structural distortions are added, the band width of the t_{2g}-like and e_g-like bands shrinks to 11.47 eV for the tetragonal, 9.82 eV for tetragonal, and 8.96 eV for the monoclinic phase.

Throughout this dissertation, we shall compare and contrast the electronic and structural properties due to these structural distortions, particularly between the cubic and monoclinic phases. Chapter 5 explores the implications when these structural distortions are tuned incrementally between these two phases using electron doping. Chapters 4 and 7 describe how structural distortions of these polymorphs influence the behavior of defects and the optical properties, respectively.

Chapter 2

Foundations and Methods for Calculating Materials Properties

In this section, an overview of the theoretical methods used to quantum mechanically describe WO_3 is given. Our primary methodology is density functional theory (DFT), and a description of its theoretical basis and practical usage is given. For the purpose of this dissertation, a brief description of relevant concepts is presented. For further details on the theory and practical implementation, the reader is referred to Ref. [42].

2.1 The Many-Body Problem

At the heart of density functional theory is quantum mechanics. The time-independent Schrödinger equation,

$$\hat{\mathcal{H}}\Psi = E\Psi, \tag{2.1}$$

describes the state of the system as captured by the (full, many-body) wave function Ψ, and is the foundation upon which first-principles calculations are based.

In any introductory quantum mechanics class, one learns the derivation for the hy-

drogen atom, for which it is possible to find an exact analytical solution. The hydrogen atom consists of a single electron interacting with Coulombic potential of the nucleus. The Hamiltonian of the hydrogen atom is thus the sum of the kinetic and potential energy of this electron. Extending to solids, which contain many atoms and electrons, a rigorous way to set up the many-body interacting Hamiltonian would be to track the Coulombic interaction between every electron and nucleus, i.e.,

$$\hat{\mathcal{H}} = -\frac{\hbar^2}{2m}\sum_i \nabla_i^2 - \sum_{i,I}\frac{Z_I e^2}{|\mathbf{r}_i^2 - \mathbf{R}_I^2|} + \frac{1}{2}\sum_{i\neq j}\frac{e^2}{|\mathbf{r}_i^2 - \mathbf{r}_j^2|} - \sum_I \frac{\hbar^2}{2M_I}\nabla_I^2 - \sum_{I\neq J}\frac{Z_I Z_J e^2}{|\mathbf{R}_I^2 - \mathbf{R}_J^2|}, \quad (2.2)$$

in which we have taken the convention for lower-case variables to correspond to the electrons and upper-case variables to the nuclei. The first and fourth terms of Eq. 2.2 describe the kinetic energy of the electron i and nucleus I with atomic number Z_I and mass M_I. The second term is the Coulomb interaction between the nuclei and electrons, while the third term captures pair-wise Coulomb interactions between electrons at positional coordinates $\mathbf{r}$, and the final term the interaction between nuclei at positional coordinates $\mathbf{R}$.

However, solving Eq. 2.2 is generally mathematically intractable and computationally impractical for systems with more than two electrons, save for a few exceptions like simple molecules. In fact, even if known solutions did exist for Eq. 2.2, the memory required to store the information needed to describe the wave function would be astronomical [43]. For example, let us estimate the amount of memory it would take to store the wave function of an oxygen atom. Consider sampling the system of N electrons with P grid points. The many-body wave function requires about P^{3N} numbers to store, where the factor of three is for the three positional coordinates. An oxygen

atom has eight electrons, so one would need to store $10^{3\times8}$ numbers for a reasonably sized grid of 10 points. Assuming memory takes 1 byte/number, the memory needed is on the order of a trillion terabytes for a single oxygen atom! Systems of single atoms, of course, are nowhere near describing an actual solid. It is partially for these reasons that DFT proved to be a groundbreaking framework for calculating phenomena related to condensed matter and laid the foundation for modern-day computational materials science. In the following sections, the basic concepts of DFT relevant to this dissertation are presented.

2.2 Fundamentals of Density Functional Theory

2.2.1 Hohenberg, Kohn, and Sham

Two concepts serve as the foundation for DFT. They are the Hohenberg-Kohn theorem and the Kohn-Shan ansatz. The Hohenberg-Kohn (HK) theorem establishes DFT as a exact many-body theory that in principle requires only knowledge of the electron density [44]. The HK theorem can be elegantly proven using the variational principle in a few short lines for non-degenerate systems via proof by contradiction, and readily extended to degenerate systems [42]. Two key ideas emerge from the HK theorem: 1) the external potential is uniquely determined by the ground-state electron density; and 2) there exists a universal functional for the total energy, and the ground-state electron density that minimizes this energy is the exact ground state. As such, DFT is predominantly a ground-state theory. Recasting the central variable to be the electron density instead of the coordinates of individual electrons is computationally attractive, of which there are far fewer parameters to keep track. However, the HK theorem only states that such a universal energy functional exists, and provides no inkling of how to calculate it.

Thus comes the Kohn-Sham (KS) ansatz [45]. In the KS framework, the many-body fully-interacting system of electrons is replaced with an auxiliary system of noninteracting particles in an effective potential chosen in such a way as to reproduce the fully interacting system. We explore the Hamiltonian of this auxiliary system in the following section.

2.2.2 Highlights of the Hamiltonian in DFT

While in principle exact, DFT in practice involves several assumptions. The first is the Born-Oppenheimer approximation, which is not unique to DFT but is nevertheless the first step taken. The Born-Oppenheimer approximation is an adiabatic approximation. In this approximation, it is assumed the electrons stay in the adiabatic ground state at any point in time as the nuclei move, i.e., the electrons move rapidly compared to the motion of the nuclei. As such, the kinetic energy of the nuclei is treated as a perturbation upon the Hamiltonian. What is gained in the Born-Oppenheimer approximation is the decoupling of the nuclei and electrons. That is, the electronic $\mathbf{r}$ and nuclear $\mathbf{R}$ degrees of freedom in the many-body wave function Ψ are assumed to be separable as

$$\Psi(\{\mathbf{r}\},\{\mathbf{R}\}) = \psi(\{\mathbf{r}\}:\{\mathbf{R}\},t)\phi(\{\mathbf{R}\},t), \tag{2.3}$$

where the set of electron coordinates $\{\mathbf{r}\}$ depends on the nuclear positions $\{\mathbf{R}\}$. In principle the lattice is able to vibrate and couple with the electrons. This coupling may be treated perturbatively to linear order. A description of how phonons and electron-phonon coupling are calculated may be found in Section 3.2. The implications of such coupling are explored in the transport properties of WO_3.

Here, we focus on the electrons and their interactions in an extended solid. We recast

the Hamiltonian defined in Eq. 2.2 as

$$\mathcal{H} = T + V_{\text{ext}} + V_{\text{ee}} + E_{II}, \tag{2.4}$$

where T is the kinetic energy of the electrons (the kinetic energy of the nuclei is neglected in the Born-Oppenheimer approximation); V_{ext} is the interaction between the electrons and nuclei; V_{ee} is the interaction between electrons; and E_{II} is the classical interaction between nuclei, and is simply a constant in the DFT framework. As covered in Section 2.2.1, the charge density serves as the central quantity and is given by

$$n(\mathbf{r}) = \langle \Psi(\{\mathbf{r_i}\}) | \sum_{i=1}^{N} \delta(\mathbf{r} - \mathbf{r}_i) \, | \Psi(\{\mathbf{r_i}\}) \rangle \, , \tag{2.5}$$

where N is the number of electrons in the system. The total energy of the system is defined as the expectation value of Hamiltonian in Eq. 2.4; noting that the total energy has become a functional of the density, the total energy is given by

$$E[n(\mathbf{r})] = \frac{\langle \psi | \, \hat{\mathcal{H}} \, | \psi \rangle}{\langle \psi | \psi \rangle} = \left\langle \hat{T}[n] \right\rangle + \left\langle \hat{V}_{\text{ee}}[n] \right\rangle + \int d\mathbf{r} n(\mathbf{r}) \hat{V}_{\text{ext}}[n] + E_{II}. \tag{2.6}$$

The KS ansatz provides a practical way of calculating the ground-state density of a system. We follow the derivation in Ref. [42]. In the KS ansatz, it is assumed that the energy functional of density $E[n(\mathbf{r})]$ may be written in terms of single-particle wave functions $\psi(\mathbf{r})$ of the non-interacting auxiliary Hamiltonian. From this assumption, the charge density easily follows as

$$n(\mathbf{r}) = \sum_{i=1}^{N} |\psi_i(\mathbf{r})|^2. \tag{2.7}$$

The ground state energy using the KS ansatz is

$$E_{KS} = T[n] + \int d\mathbf{r} V_{\text{ext}}(\mathbf{r}) n(\mathbf{r}) + E_{\text{Hartree}}[n] + E_{\text{XC}}[n], \tag{2.8}$$

where we have the kinetic energy of the electrons $T[n]$ and potential between nuclei and electrons $V_{\text{ext}}(\mathbf{r})$ as before in Eq. 2.2. Two new terms have appeared, which collectively describe the electron-electron interactions. E_{Hartree} represents the classical Coulomb interaction of the electron density, named after D.R. Hartree who first included it:

$$E_{\text{Hartree}} = \frac{1}{2} \int d\mathbf{r} d\mathbf{r}' \frac{n(\mathbf{r}) n(\mathbf{r}')}{|\mathbf{r} - \mathbf{r}'|}, \tag{2.9}$$

where the factor of $\frac{1}{2}$ accounts for double-counted interactions. The quantum mechanical component, i.e., many-body term, of the electron-electron interaction is encapsulated in E_{XC}, known as the exchange-correlation energy. E_{XC} is composed of the exchange E_{X} and correlation E_{C} energies. The exchange component arises from the Pauli exclusion principle. The correlation energy is defined as the difference between the exact energy and the energy of an uncorrelated system. Together the exchange and correlation encapsulate all many-body phenomena of the true interacting system not captured by the fictitious non-interacting system. In dealing with an auxiliary system, the KS framework allows us to deal with independent particles but an interacting density.

If a universal $E_{\text{XC}}[n]$ were known, the exact ground state and density of the many-body problem could be determined. However, of the terms in Eq. 2.8, $E_{\text{XC}}[n]$ remains unknown and must be approximated. The crux of DFT is then to find functionals for $E_{\text{XC}}[n]$, as described in the next section.

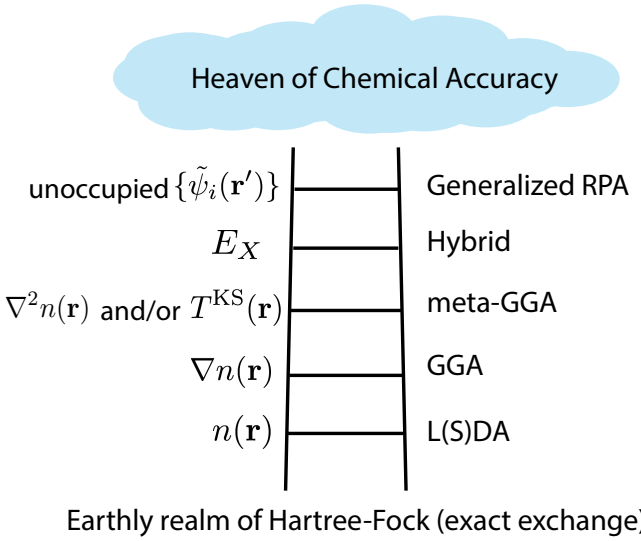

Figure 2.1: Hierarchy of accuracy in approximations to the exchange-correlation functional as shown on a Jacob's ladder. On the right side are the ingredients that go into the calculation of the exchange-correlation energy. At each higher rung of the ladder, the ingredients from lower rungs are also included. L(S)DA = local (spin) density approximation, GGA = generalized gradient approximation, RPA = random phase approximation. Higher accuracy requires more computational resources. Adapted from Ref. [46].

2.3 Historical Overview of Functionals

Many descriptions of the exchange-correlation have been developed over the past few decades since the formulation of DFT. With brevity, we describe a few early attempts up until the development of hybrid functionals. Other more advanced methods for describing many-body interactions exist, such as many-body perturbation theory in the *GW* approach for describing excitations, but these lie outside the scope of this dissertation.

The development of accuracy in functionals is aptly described with a version of Jacob's ladder, which describes the main ingredients used and historical development of the various formulations on the exchange-correlation energy, as shown in Fig. 2.1. The reader is encouraged to peruse Refs. [46, 47] for further information.

At the lowest level is Hartree-Fock, in which only exchange interactions are considered. Exchange-correlation in the DFT framework begins at the local (spin) density approximation, or L(S)DA in which the exchange-correlation is taken to be that of a uniform electron gas, which is known exactly from Monte Carlo and other many-body methods. At the next level is the generalized gradient approximation (GGA), which includes dependence on the gradient of the local electron density. A further variant is meta-GGA, in which the second spatial derivative and the kinetic energy of the KS orbitals are included. However, these methods are known to severely underestimate the band gap due to poor handling of the self-interaction error [48, 49, 47]. Hybrid functionals address this by including some part of the exact exchange E_{X}, which is known from Hartree-Fock (HF) theory, and given by

$$E_{\mathrm{X}}^{\mathrm{HF}} = -\frac{1}{2}\sum_{i,j}\int d\mathbf{r}d\mathbf{r}'\tilde{\psi}_i^*(\mathbf{r})\tilde{\psi}_j^*(\mathbf{r}')\frac{1}{|\mathbf{r}-\mathbf{r}'|}\tilde{\psi}_j(\mathbf{r})\tilde{\psi}_i(\mathbf{r}'). \tag{2.10}$$

One can go further still in incorporating non-local ingredients, such as unoccupied KS orbitals, as is the case in the generalized random phase approximation (RPA). Further discussion of the accuracy of various functionals may be found in Refs. [50, 51].

In this dissertation, we primarily use hybrid functionals. For all such hybrid functionals, the XC energy takes the form

$$E_{\mathrm{XC}}[n] = \alpha E_{\mathrm{X}}^{\mathrm{HF}}[n] + (1-\alpha)E_{\mathrm{X}}^{\mathrm{DFT}}[n] + E_{\mathrm{C}}^{\mathrm{DFT}}[n] \tag{2.11}$$

where α is an adjustable "mixing" parameter of how much exact exchange to include. While adjustable, a typical value is 25%. Specifically, we use the functional from Heyd, Scuseria, and Ernzerhof (HSE) [52, 53], which mixes the short-range exchange with screened Hartree-Fock exchange. That is, the Coulomb interaction is divided into a

short- (SR) and long-range (LR) component; a screened Coulomb potential is applied only to the exchange interaction, which screens the long-range part of the Hartree-Fock exchange. This may be represented as

$$E_{\mathrm{XC}}^{\mathrm{HSE}}[n] = \alpha E_{\mathrm{X}}^{\mathrm{HF,SR}} + (1-\alpha)E_{\mathrm{X}}^{\mathrm{PBE,SR}} + E_{\mathrm{X}}^{\mathrm{PBE,LR}} + E_{\mathrm{C}}^{\mathrm{PBE}}, \tag{2.12}$$

where PBE is the GGA functional developed by Perdew, Burke, and Ernzerhof [54].

2.4 DFT in Practice

2.4.1 The Choice of Basis

The basis set is often chosen out of convenience, either in the mathematics or in the implementation. As we work with extended systems, plane waves are the natural choice of basis set to represent the KS orbitals. Other basis sets are possible, and many variations are known in quantum chemistry, where the focus is on molecules and where basis sets of more localized character are a natural choice.

For extended systems, the Bloch theorem states that each eigenfunction of the Schrödinger equation can be expressed as the product of a plane wave and a function $u_{n\mathbf{k}}$ with the periodicity of the crystal,

$$\psi_{n\mathbf{k}}(\mathbf{r}) = e^{i\mathbf{k}\cdot\mathbf{r}} u_{n\mathbf{k}}, \tag{2.13}$$

where the periodic part is expanded in reciprocal lattice vectors $\mathbf{G}_l$

$$u_{n\mathbf{k}}(\mathbf{r}) = \frac{1}{\sqrt{V_{\mathrm{cell}}}} \sum_l c_{n,l}(\mathbf{k}) e^{i\mathbf{G_l}\cdot\mathbf{r}}. \tag{2.14}$$

In order to solve for the wave function, a scheme to represent the potential due to the nuclei plus the core electrons is needed. For that, we turn to pseudopotentials. The central idea of pseudopotentials is to "smooth out" the rapid oscillations of the core electron wave functions with an effective ionic potential that acts on the valence electrons, as these rapid oscillations are computationally expensive to represent. Fortuitously, in most solids and molecules, bonding is mainly determined by the interaction of valence electrons.

Many modern electronic structure codes use the projector-augmented wave method (PAW) [55, 49] to generate pseudopotentials. PAW builds upon older pseudopotential techniques based on projectors and auxiliary functions. The basic idea is to map the true wave functions onto auxiliary wave functions via some linear transformation. This transformation is defined with some set of projection operators that contain the full all-electron wave function. Thus, the full all-electron wave function is recoverable via a linear transformation. In this dissertation, all of our calculations are based on PAW pseudopotentials, unless otherwise noted. The reader is referred to Refs. [55, 42, 56] for further details and references.

2.4.2 Numerical Considerations

In order to make sure our calculations output reasonable results, any calculation must be tested for numerical convergence. We cover the convergence criteria that are immediately relevant to this dissertation: namely basis set, energy cutoff, sampling of the Brillouin zone, periodic boundary conditions, supercells, and charge neutrality.

With the choice of a plane-wave basis, one must choose when to truncate the series. Each plane wave is indexed by a wavevector $\mathbf{k}$, which is related to the crystal momentum and this is related to the energy cutoff, which scales as $|\mathbf{k}|^2$. The energy cutoff is element

and pseudopotential specific. Like anything in computation, one must balance accuracy with computational efficiency. The reader is referred to Ref. [42] or any user guide for released DFT codes for additional details.

For extended systems, we use periodic boundary conditions. While a natural choice for calculating bulk properties, this requires careful consideration for (charged) defects (see Chapter 4) or charged cells (see Chapter 5). First is the choice of supercell size. In our studies of various point defects, we aim to extract the dilute limit. Current state-of-the-art DFT calculations can reasonably handle around a few hundred to a few thousand atoms for advanced functionals like hybrid functionals. Thus, while we aim to have as large a supercell as possible, we are limited by what is computationally practical and feasible. Nevertheless, it is important to choose a sufficiently large supercell, or at least understand the limitations of insufficiently large supercells. A short illustrative study is documented for oxygen vacancies in Chapter 4.

Secondly and relatedly, imposing periodic boundary conditions will lead to spurious interactions between periodic images of charged defects, which is particularly problematic given the long-range nature of Coulomb interactions. As such, the energy of the system will diverge. In the case of charged defects, we use a correction scheme from Freysoldt and collaborators [57, 58]. For the case of charged cells, a background jellium is added. This jellium is uniformly applied to the cell and provides the compensating charge needed to achieve a charge neutral system (see p. 502 in Ref. [42]).

Finally, we comment briefly on Brillouin zone sampling (including both **k**-point sampling for electrons and **q**-point sampling for phonons). The discrete sampling of the Brillouin zone requires a sufficient number of **k**-points in order to converge forces and energies. Calculating materials properties involves evaluating integrals over the Brillouin zone that often require much more dense sampling compared to self-consistent calculations (see calculation of electrical conductivity in Chapter 6 and optical absorption in

Chapter 7). Conventional methods are prohibitively expensive for well-converged results. Thus we turn to alternate but advanced interpolation schemes, i.e., Wannier interpolation. The methodology we use is based on Wannier functions, which are described in the following section.

2.4.3 The Wannier Basis

Standard DFT codes choose plane-waves as the basis set to expand and represent the wave functions. This choice is natural, both physically and computationally. The translational symmetry of the crystal naturally lends itself to plane-waves in the Bloch representation of the wave function (Eq. 2.13).

Wannier functions were originally proposed by Gregory Wannier [59] in the late 1930s as another basis set for e.g., tight-binding calculations, but only recently gained traction as a useful tool in computational condensed matter physics. Wannier functions are essentially the Fourier transform of the Bloch representation

$$w_{n\mathbf{R}}(\mathbf{r}) = \frac{V}{(2\pi)^3} \int_{BZ} \Big[\sum_m U_{mn}^{(\mathbf{k})} \psi_{m\mathbf{k}} \Big] e^{-i\mathbf{k}\cdot\mathbf{r}} d\mathbf{k}, \tag{2.15}$$

where $w_{n\mathbf{R}}(\mathbf{r})$ is a Wannier function centered on lattice site $\mathbf{R}$ indexed by band n. $U_{mn}^{(\mathbf{k})}$ is a unitary matrix that transforms a manifold of Bloch states to Wannier states. This unitary transformation preserves orthonormality of the Bloch states.

The reason why we turn to Wannier functions essentially boils down to 1) the ability to achieve linear scaling for calculating ground-state properties requiring dense meshes and 2) the greater physical intuition gained on chemical bonding. Thus, Wannier functions are a useful tool for calculating materials properties efficiently, particularly on dense grids as we shall see in Chapters 6 and 7. The application of the Wannier basis set is discussed in further detail in Sections 3.5 and 3.2.2.

In principle, there is no unique way of choosing Wannier functions due to the indeterminacy of gauge in Bloch functions. For example, a Bloch wave function $\psi_{n,\mathbf{k}}$ can be transformed into

$$\left|\bar{\psi}_{n,\mathbf{k}}\right\rangle = e^{i\phi_n(\mathbf{k})}\left|\psi_{n,\mathbf{k}}\right\rangle \tag{2.16}$$

for any real function $\phi_n(\mathbf{k})$ that is periodic in reciprocal space. Such a transformation does not change the physical description but a different choice of $\phi_n(\mathbf{k})$ leads to a different set of Wannier functions. A reasonable solution then is to use maximally localized Wannier functions (MLWF). Significant effort has been put into developing and implementing the methods for the transformation of Bloch wave functions to MLWFs [60, 61]. This has culminated in the open-source software package `Wannier90` [62, 63].

We outline the methodology for finding MLWFs here. Two components are needed to construct the Wannier functions: 1) the projection of Bloch states onto an initial set of trial functions used to find the set of smoother Bloch orbitals and 2) the overlaps between the periodic part of the Bloch states. The key to achieving MLWFs is ensuring that the Bloch orbitals are first "smooth," i.e., the derivative with respective to $\mathbf{k}$ is regular, $\nabla_{\mathbf{k}}\left|\bar{\psi}_{n,\mathbf{k}}\right\rangle$. This is not guaranteed with Bloch functions as defined in Eq. 2.13 due to e.g., electronic degeneracies in the Brillouin zone [63]. Smoothness of the Bloch functions is needed in order to be able to apply optimization methods for finding the maximially localized set of orbitals in real space. The set of smooth Bloch orbitals is achieved via the projection of Bloch states onto a set of trial functions. Further details are given in Refs. [60, 63, 61]. In order to find MLWFs, the spatial localization of the Wannier wave functions

$$\Omega = \sum_n \left[\left\langle w_{n\mathbf{0}}(\mathbf{r})\right| r^2 \left|w_{n\mathbf{0}}(\mathbf{r})\right\rangle - \left\langle w_{n\mathbf{0}}(\mathbf{r})\right| r \left|w_{n\mathbf{0}}(\mathbf{r})\right\rangle^2 \right], \tag{2.17}$$

is minimized via steepest descent, The terms in Eq. 2.17 may be rewritten in terms of the overlaps between the periodic part of the Bloch states [63]. Details and derivation of what this entails may be found in the `Wannier90` user guide, including usage with standard DFT codes. In this dissertation, we use the Wannier basis in order to calculate electron-phonon (see Section 3.4) and optical (see Section 3.5) matrix elements on dense meshes that would otherwise be computationally prohibitive to calculate.

2.5 Molecular Dynamics

DFT alone is well-suited for calculating static structures at 0 K. However, many phenomena of interest occur at finite temperatures. One method of investigating structure and dynamics at finite temperatures is molecular dynamics. The methodology described here applies equally to classical or quantum mechanical systems. When forces and energies are derived from DFT, this methodology is known as quantum or *ab initio* molecular dynamics.

Within the context of this thesis, we use molecular dynamics to generate disordered structures at elevated temperatures, as described in Chapter 7. The reader is referred to Refs. [64, 65] for further discussion of molecular dynamics. Here, we provide a brief overview of key concepts.

2.5.1 Theoretical Overview

A key property we assume in our calculations is ergodicity. Ergodicity is the idea that an ensemble average of several configurations is equivalent to a time average over the phase space. The phase space collectively consists of the position and momenta of the particles in the system. In the context of generating amorphous structures, this means for sufficiently long simulation times, we adequately sample the ensemble of atomic

configurations possible in a disordered solid.

At its core, molecular dynamics involves solving Newton's equations of motion $\mathbf{F}_I = m_I \mathbf{a}_I$ for each particle I in the system. For large-scale systems, this consists of $3N$ coupled differential equations of the form

$$\frac{d\mathbf{p}_I}{dt} = -\frac{dU(\mathbf{R}^N)}{d\mathbf{R}_I} \tag{2.18}$$

for some momentum $\mathbf{p}_I$ and potential U with N particles each with coordinates $\mathbf{R}_I$ in the system. The set of equations defining the motion of the nuclei satisfies conservation of total energy, i.e.,

$$\frac{dH}{dt} = \Big[\sum \frac{dU}{d\mathbf{R}_I}\frac{d\mathbf{R}_I}{dt} + \sum \frac{d}{dt}\big(\frac{\mathbf{p}_I^2}{2m_I}\big)\Big] = 0; \tag{2.19}$$

conservation of net linear and net angular momentum; and time-reversal symmetry.

In a solid, we are primarily concerned with forces and velocities of the nuclei. Forces may be obtained in quantum molecular dynamics using the Hellmann-Feynman theorem, which directly connects forces on nuclei to the charge density. The force on nuclei can always be written as

$$\mathbf{F}_I = -\frac{\partial E}{\partial \mathbf{R}_I}. \tag{2.20}$$

The Hellmann-Feynman theorem states

$$\mathbf{F}_I = -\frac{\partial E}{\partial \mathbf{R}_I} = -\left\langle \Psi \left| \frac{\partial \hat{H}}{\partial \mathbf{R}_I} \right| \Psi \right\rangle - \frac{\partial E_{II}}{\partial \mathbf{R}_I}. \tag{2.21}$$

Amazingly, knowing the forces requires only terms with explicit dependence on only nuclear positions. We may see why this is case using Eq. 2.6 for the expression of energy

and assuming properly normalized wave functions. Expanding Eq. 2.6, we get

$$-\frac{\partial E}{\partial \mathbf{R}_I} = -\left\langle \Psi \left| \frac{\partial \hat{H}}{\partial \mathbf{R}_I} \right| \Psi \right\rangle - \left\langle \frac{\partial \Psi}{\partial \mathbf{R}_I} \left| \hat{H} \right| \Psi \right\rangle - \left\langle \Psi \left| \hat{H} \right| \frac{\partial \Psi}{\partial \mathbf{R}_I} \right\rangle - \frac{\partial E_{II}}{\partial \mathbf{R}_I}. \tag{2.22}$$

For the exact solution to the ground state, the second and third terms vanish by the variational theorem. This expression holds for local and non-local potentials, e.g., pseudopotentials used in the practical implementation of DFT.

Different possible configurations are sampled via propagating the equations of motion with respect to time. Numerically integrating the coupled equations of motion described by Eq. 2.18 involves discretizing time. A simple and robust way of incrementing the positions and momenta is known as the velocity Verlet algorithm [66].

$$\mathbf{R}_I(t+\delta t) = \mathbf{R}_I(t) + \mathbf{v}_I(t)\delta t + \frac{1}{2m_I}\mathbf{F}_I(t)\delta t^2 \tag{2.23}$$

$$\mathbf{v}_I(t+\delta t) = \mathbf{v}_I(t) + \frac{1}{2m_I}(\mathbf{F}_I(t) + \mathbf{F}_I(t+\delta t))\delta t. \tag{2.24}$$

The Verlet algorithm is based on a Taylor expansion of the updated position $\mathbf{R}_I(t+\delta t)$ around small time increments δt. From there, an expression for the updated velocity $\mathbf{v}_I(t+\delta t)$ may be written down. As the updated positions $\mathbf{R}_I(t+\delta t)$ depend only on quantities at time t, the updated forces and velocities may be calculated at time step t. Despite its simplicity, the velocity Verlet algorithm is quite robust, with errors in positions and velocities on the order of δt^4.

Standard molecular dynamics simulations use the microcanonical ensemble (NVE), which consist of a fixed number of particles N, volume V, and energy E. At equilibrium, the kinetic and potential energies will fluctuate around their average values, but still conserve the total energy. The microcanonical ensemble has a direct connection to measureable thermodynamic values, such as temperature. However, actual experimental

conditions typically do not involve fixed volume or energy. Rather their respective conjugate variables, pressure and temperature, are the fixed conditions. Thus, it is useful to go beyond the microcanonical ensemble. Here, we will primarily discuss the canonical ensemble (NVT), which has fixed volume and temperature. In this dissertation, the canonical ensemble is used as a means for simulating melting and quenching conditions to achieve disordered structures.

2.5.2 Choosing a Thermostat

The choice of the canonical ensemble (NVT) necessitates a choice of the thermostat, or mechanism for ensuring some setpoint for the average temperature of the system. There are several choices to the thermostat, each with a different strategy for achieving a fixed temperature. We discuss three: the Berendsen thermostat [67], Andersen thermostat [68], and Nosé-Hoover thermostat [69, 70].

The Berendsen thermostat utilizes velocity rescaling to achieve a fixed temperature. In this methodology, the velocities are scaled by some constant $\lambda = \sqrt{1 + \frac{\Delta t}{\tau_T}(\frac{T}{T_0} - 1)}$ for some integration time step Δt and setpoint temperature T_0. The strength of coupling between the system and a fictitious heat bath is described with τ_T, which serves as a measure for how long it takes the system to equilibrilate to T_0. In general velocity rescaling techniques, like the Berendsen thermostat, do not strictly follow the canonical ensemble, and are therefore not recommended.

The Andersen thermostat involves stochastic coupling. That is, some subset of the particles in system are stochastically chosen to collide with the heat bath. These selected particles have their momenta reassigned to a value drawn from a Maxwell-Boltzmann distribution at the setpoint temperature. While this satisfies the canonical distribution, it can disrupt correlations between particle velocities, which renders extracting dynamic

properties diffcult, if not erroneous.

The thermostat of choice in most modern simulations is the Nosé-Hoover thermostat, which uses an extended Hamiltonian to couple to a heat bath. The Nosé method introduces an extra degree of freedom for the heat bath so that energy can flow in and out of the reservoir as needed. Hoover further simplified the equations of motions in the thermostat proposed by Nosé in terms of parameters relating to the fictitious heat bath. The Nosé-Hoover thermostat is a popular choice for reasons that the canonical ensemble can be recovered, it is deterministic, and it preserves time-reversal symmetry [71]. If the reader is interested, further information and relevant equations may be found in Refs. [72, 73].

The theory and methods described are the foundation in the methodology described in Chapter 7 for generating disordered structures.

2.5.3 Molecular Dynamics Using *Ab initio* Codes

Molecular dynamics simulations in *ab initio* codes come in two main flavors. One flavor is the use of the Born-Oppenheimer approximation as described in Section 2.2. In this framework, the forces on the nuclei are calculated at each iteration with the time-independent Schrödinger equation. An alternative flavor is the Car-Parrinello method [74] that introduces the electronic degrees of freedom as a fictitious variable in an extended Hamiltonian, and effectively leads to a coupled system of nuclei and electrons. In the calculations described in Chapter 7, the Born-Oppenheimer molecular dynamics method is utilized.

2.6 Calculation Methodology

The primary packages used in our studies are the Vienna *Ab initio* Simulation Package (VASP)[75, 49] and Quantum Espresso [76]. We additionally use the `Wannier90` [62, 63] code for post-processing and calculation of transport and optical properties.

Our calculations are based on (generalized) Kohn-Sham theory [45] using projector-augmented wave pseudopotentials [55], as implemented in the Vienna *Ab initio* Simulation Package (VASP). For W, the $5d$ and $6s$ states are treated as valence states; for O, the valence states are the $2s$ and $2p$ states. We use the hybrid functional of Heyd, Scuseria, and Ernzerhof (HSE) [52, 53]. In HSE, the amount of mixing between the non-local Hartree-Fock exchange with short-range exchange of PBE is chosen to be the standard 25%. A plane-wave cutoff of 500 eV is used. For equilibrium crystalline structures, a **k**-point mesh of $6 \times 6 \times 6$ for the 4-atom cubic phase and $4 \times 4 \times 4$ for the 32-atom monoclinic phase are used. Further computational details are found in the respective Chapters. All calculations, unless otherwise stated, are based on the HSE functional with the aforementioned calculation parameters.

Chapter 3

Theoretical Overview of Electronic Behavior in Materials

We examine both transport and optical properties associated with WO_3 to understand the influence of high doping levels. This section provides an overview of the various materials phenomena investigated. Chapter 4 studies the (de)localization of electrons associated with charged defects; Chapter 5 explores how electron doping drives phase transformations; Chapter 6 looks explicitly at electron-phonon coupling on carrier transport; and Chapter 7 studies the influence of electron doping on optical absorption.

We group the fundamental concepts of the following Chapters based on the following topics. We begin with the Drude model, a phenomenological model that we draw upon to contrast with our first-principles calculations. Second, going from free to localized carriers, a brief overview of polarons is presented, followed by electron-phonon interactions. A short description of spin-orbit coupling is also presented, as it is large for W. We additionally provide the methodology and theory for computing the mobility and optical spectra of a material. While these methods are applied to WO_3, many of the principles described here apply to other materials systems.

3.1 To Localize or Delocalize Electrons

The interaction of electrons with the crystal lattice can manifest in several ways. Electrons can be (spatially) delocalized or localized, and the extent to which localization occurs has a significant impact on the electronic and optical properties. Here, we provide a brief overview of several important models for understanding free carriers and polarons. Many of the basic concepts here will be useful in Chapters 4 and 7.

3.1.1 The Drude Model: A Classical Look at Free Carriers

It turns out that electronic transport and optical properties are closely related, both being mediated by electrons. The quantum mechanical treatment of electrical conductivity and optical absorption may both be cast in terms of an expression for conductivity based on Fermi's Golden Rule [77, 78]. We describe the quantum mechanical treatment of transport in Section 3.4.2 and that of optical properties in Section 3.5.

The earliest attempts at understanding electrical and optical conductivity were phenomenological. One such well-known model is the Drude model, which was originally created to describe transport properties in simple metals. While the original derivation was intended to describe transport with scattering events, many concepts from the Drude model cross-apply to optical properties.

We begin with a simple derivation of the Drude model as it relates to electrical conductivity. In this model, the electrons are treated classically as particles that bounce off heavier, relatively immobile ions, as shown in Fig. 3.1. The equations that describe the drift velocity $\mathbf{v}$ of electrons of mass m in an electric field is simply a damped version of Newton's equations of motion

$$m\frac{d\mathbf{v}}{dt} + \frac{m\mathbf{v}}{\tau} = e\mathbf{E}_0 e^{-i\omega t} \tag{3.1}$$

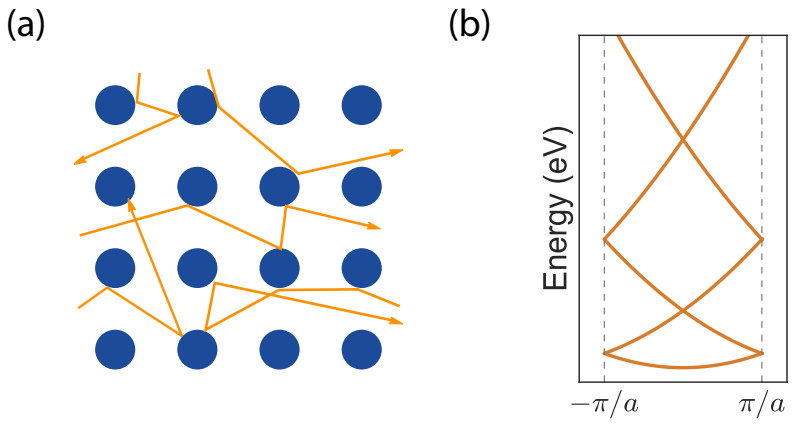

Figure 3.1: Schematic representation of the assumptions in the free-electron gas model. In addition to the Pauli exclusion principle enforced by Fermi-Dirac statistics, the free-electron gas model also assumes (a) a sea of pinball-like electron particles (orange paths) scattering off immobile ions (blue circles), characterized by relaxation time τ between scattering events; (b) the dispersion of the free-electron approximation, where interactions between the electrons and nuclei are neglected. Additionally, electron-electron interactions are neglected.

where a relaxation time τ, or $\gamma = 1/\tau$ the scattering rate, has been introduced as a damping term. τ is related to the average path distance an electron travels before encountering the next scattering center. Solutions for the velocity $\mathbf{v}$ to this differential equation also have a sinusoidal form

$$\mathbf{v} = \mathbf{v}_0 \, e^{-i\omega t}. \tag{3.2}$$

Inserting Eq. 3.3 into Eq. 3.1 gives you

$$(-mi\omega + m/\tau)\mathbf{v}_0 = e\mathbf{E}_0 \rightarrow \mathbf{v}_0 = \frac{e\mathbf{E}_0}{(-mi\omega + m/\tau)} \tag{3.3}$$

Using the definition of the carrier density $j = ne\mathbf{v}_0 = \sigma\mathbf{E}_0$, we find the complex conductivity to be

$$\sigma^{\text{Drude}}(\omega) = \frac{ne^2\tau}{m(1 - i\omega\tau)} \tag{3.4}$$

for some carrier concentration n. When $\omega = 0$, one recovers the well-known DC electric conductivity $\sigma^{\text{Drude}} = ne^2\tau/m$.

Sommerfeld added quantum mechanical Fermi-Dirac statistics to the classical Drude model, which made possible the derivation of simple and relatively successful models for describing electrical and thermal conductivities, density of states, and heat capacity in materials (see Ref. [26] for more information). This is known as the free-electron gas model. The assumptions of the free-electron gas model are shown schematically in Fig. 3.1. Thus, the Drude(-Sommerfeld) model has continued to be a useful tool for gaining intuition in complex materials systems. For an electron in a material, the free-electron mass m is replaced with the effective mass m^* (assumed to be isotropic). We shall see in Section 3.4.2 that the Drude model can be recovered in the Boltzmann transport formalism under the assumptions of the free-electron gas model.

We now turn to how the Drude model relates to optical properties. The imaginary part of the complex conductivity determines the dissipative part of the response function as captured by the complex dielectric function $\varepsilon = \varepsilon_1 + i\varepsilon_2$ with

$$\varepsilon_2^{\text{Drude}}(\omega) = \frac{4\pi\sigma}{\omega} = \frac{4\pi}{\omega}\frac{ne^2\tau}{m(1+\omega^2\tau^2)}. \tag{3.5}$$

With the dielectric function in hand, it is possible to find an expression for the absorption and reflectance. The absorption and reflectance in the Drude model is shown schematically for various τ in Fig. 3.2. An important parameter that emerges from this derivation is the plasma frequency, which is defined as

$$\omega_p^2 = \frac{4\pi ne^2}{m\varepsilon^\infty}\ (\text{CGS}) = \frac{ne^2}{m\varepsilon^0\varepsilon^\infty}\ (\text{SI}), \tag{3.6}$$

where the mass m is typically taken to be the effective mass of the electron. The plasma

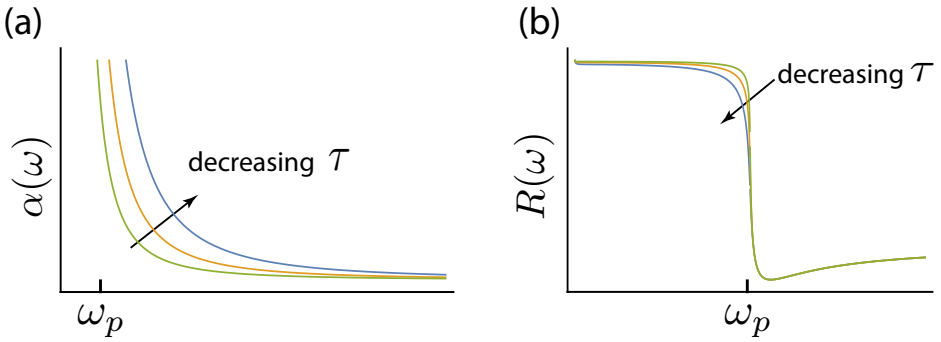

Figure 3.2: (a) absorption coefficient $\alpha(\omega)$ and (b) reflectivity spectra $R(\omega)$ in the free-electron gas model for various values of the scattering rate ($\gamma_p = 1/\tau = \omega_p/200, \omega_p/100, \omega_p/50$). Arrows indicate the trend in absorption coefficient α and reflectivity R for decreasing relaxation time τ; the plasma frequency ω_p is shown for $\gamma_p = \omega_p/200$.

frequency delineates at what point along the electromagnetic spectrum the reflectance drops substantially and the material becomes transparent to higher incident energies. We refer the reader to Section 3.5.2 for details on the relations between the dielectric constant and measured optical spectra.

The absorption for free carriers is

$$\alpha^{\text{Drude}}(\omega) = \frac{n}{c}\frac{\omega_p^2\gamma}{\omega^2}, \tag{3.7}$$

where we define $\gamma = 1/\tau$ as the dampening constant and take this damping constant to be small relative to the plasma frequency. Like with Boltmann transport theory, the quantum mechanical treatment of the optical conductivity as derived by Kubo and Green can be reduced to the form of the Drude model in Eq. 3.4, assuming a single parabolic band [78].

For d-band perovskites such as WO_3 that have complicated features in the band structure, the Drude model is insufficient, and we must turn to quantum mechanical descriptions. The shortcomings of the Drude model are further discussed in Section 3.4

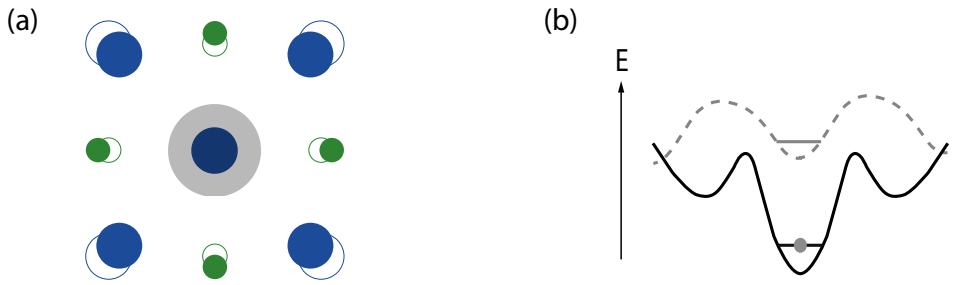

Figure 3.3: (a) Schematic of a self-trapped polaron: the cations (large blue circles) and anions (small green circles) shift from their equilibrium positions (open circles) in the presence of excess charge (grey shaded region). (b) Schematic of the energy landscape of a self-trapped polaron: displaced ions result in a potential well (solid curve) that lowers the energy of the carrier compared to that of the unperturbed potential (dotted curve). Adapted from Ref. [80].

for transport and Chapter 7 for optical properties.

3.1.2 Polarons: the Localization of Electrons

A polaron is a quasiparticle consisting of a self-trapped carrier and the associated displacements of atoms from their equilibrium positions, as shown in Fig. 3.3. If coupling between the electrons and lattice is strong, the formation of polarons becomes favorable. We follow the description of polarons from David Emin, which provides a useful overview of polaron formation and related transport phenomena [79].

A polaron is formed if the change in ionic positions leads to a potential well that self-traps the carrier. The carrier is assumed to be moving slowly enough so as to induce shifts in the ionic positions.

Polarons are categorized into two main categories for polarons (i.e., when electron-phonon interactions play a sizeable role): large and small polarons. As the name suggests, a large polaron is a quasiparticle whose spatial extent spans several unit cells. Large polarons are massive quasiparticles that have been found to scatter coherently, i.e., with occasional scattering events with mobilities typically $> 1\,\mathrm{cm}^2/\mathrm{V}\cdot\mathrm{s}$ that fall

with temperature. In contrast, small polarons are confined to a single unit cell and scatter incoherently, i.e., via hopping with mobilities typically $\ll 1\,\mathrm{cm}^2/\mathrm{V}\cdot\mathrm{s}$ that typically rise with temperature, reflecting some activation energy. Thus, whether small or large polarons form in the material has profound implications for the optical and electronic response of a material.

It is possible for large and small polarons to coexist. This has been found to be the case based on explicit first-principles calculations for oxides such as TiO_2 [81]. Thus, the formation of smaller versus large polarons requires a case-by-case study. We discuss the formation and existence of polarons in Chapter 4, particularly in the context of oxygen vacancies in WO_3 compared to other oxides. We shall see that while small polarons have been invoked to explain electrical conductivity and optical behavior, they are unstable in crystalline WO_3. Instead, our calculations show that large polarons can form.

Thus far, we have only provided descriptions of the general categories of polaron formation. Polaron formation is related to the more general phenomena of electron-phonon interactions. The extent to which polaron formation is favored is determined by the strength of electron coupling to the lattice. The following sections describe the quantum mechanical treatment of electron-phonon interactions in materials and how they relate to transport properties.

3.2 Electron-Phonon Interactions in Polar Materials

Electron-phonon interactions can have a profound impact on the nature of the electronic, transport, and optical properties of materials. In the scope of this dissertation, we study their contribution to transport, as discussed in Section 3.4.2. Here, we present the formulation for understanding electron interactions with the lattice explicitly using linear order perturbation theory, focusing on electron-phonon coupling to polar optical

phonon modes.

3.2.1 Calculation of Vibrational Properties

To start, we describe the methodology used to calculate vibrational properties in a material. At finite temperatures, the collective motion of atoms as phonons plays an important role. It is possible to decompose this vibration into phonon or vibrational modes by essentially solving a set of coupled differential equations as an eigenvalue problem. At the foundation of calculating a material's vibrational spectrum is the Born-Oppenheimer approximation, as described in Section 2.2.2, which allows us to treat separately the electronic and ionic degrees of freedom. One method for calculating the phonon modes in a system is density functional perturbation theory (DFPT). The derivation and relevant equations in DFPT may be found in Ref. [82].

The linear response of the electron density is used to calculate the vibrational spectra of a material. It is based on the assumption that, like in DFT, the system obeys the Kohn-Sham equations and the vibrations in the crystal can be treated perturbatively. In the harmonic approximation, the phonon modes are extracted from the determinant of the interatomic force constants (IFCs), which is a Hessian of the Born-Oppenheimer energy surface scaled by atomic masses

$$\det\left|\frac{1}{\sqrt{M_I M_J}}\frac{\partial^2 E(\mathbf{R})}{\partial \mathbf{R}_I \partial \mathbf{R}_J} - \omega^2\right| = 0, \tag{3.8}$$

where ω are the phonon frequencies, and $\mathbf{R}_I$ is the position coordinate of atom I with mass M_I. The Hellmann-Feynman theorem defined in Eq. 2.21 is used to find the interatomic force constants. The linear-order response of the wave function and potential, which are needed in the calculation of the interatomic force constants, are obtained from first-order perturbation theory.

One expects $3N$ phonon modes, where N is the number of atoms in the simulation cell. For any material with at least two distinct atomic sites, two kinds of modes appear—acoustic and optical. The derivation of a simple 2-atom-site system that demonstrates this can be found in many standard solid-state textbooks [25, 26, 27]. Of these modes, three are acoustic modes in which the motion of the atoms is in-phase with each other; the remaining are optical modes in which the atoms move out of phase with each other. Phonons can be grouped into collections of modes corresponding to transverse and longitudinal motions, which describe along which axes these vibrational modes exist based on group theory and symmetry. While the discussion of group theory and symmetry of phonons is outside the scope of this dissertation, further information may be found in Ref. [83].

Finally, we make note of some practical considerations when calculating phonons. Sum rules impose physical constraints. For phonons, this is known as the acoustic sum rule (ASR), which emerges from the translational invariance and charge neutrality of the system. This is because at Γ, the acoustic modes are simply a rigid shift of the cell. In practice, our calculations break translational symmetry, owing to a variety of reasons, including the discreteness of the grid for finite Fourier transforms, an under-converged geometry, or finite cell effects. There are several schemes for imposing the ASR [84]. We use the 'crystal' scheme as described in Ref. [85].

3.2.2 Models for Electron-Phonon Interactions in Polar Materials

The interaction between electrons and phonons plays an important role in electrical conductivity, superconductivity, and optical properties of materials. We shall see how it plays a role in mobility in the following section. In Dirac notation, one way to calculate

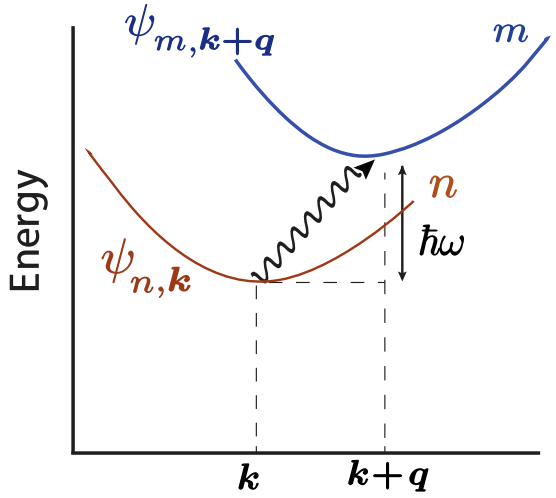

Figure 3.4: Schematic illustrating $g_{\boldsymbol{q},\nu}$ as described in Eq. 3.9. The electron-phonon interaction causes an electron to scatter between electron states separated by q in reciprocal space and $\hbar\omega$ in energy.

the electron-phonon interaction, or matrix element is

$$g_{\boldsymbol{q},\nu} = \left(\frac{\hbar}{2M\omega_{\boldsymbol{q},\nu}}\right)^{\frac{1}{2}} \left\langle \psi_{n,\,\boldsymbol{k}} \left| \frac{\delta V_{SCF}}{\delta \boldsymbol{u}_{\boldsymbol{q},\nu}} \right| \psi_{m,\,\boldsymbol{k}+\boldsymbol{q}} \right\rangle, \tag{3.9}$$

where the electron-phonon matrix element $g_{\boldsymbol{q},\nu}$ is calculated from the overlap between two electronic states, as schematically depicted in Fig. 6.2. The deformation potential $\delta V_{SCF}/\delta \boldsymbol{u}_{\boldsymbol{q},\nu}$ measures how much the self-consistent potential changes with respect to some pattern of atomic displacement $u_{\mathbf{q},\nu}$ for phonon wavevector $\mathbf{q}$ with phonon mode index ν.

Electrons scattering off the polar longitudinal optical (LO) phonons requires special treatment due to the long-range nature. This long-range nature physically arises from the long-range macroscopic electric fields that arise from the out-of-phase motion of the atoms. A useful analogy is given in Ref. [25], where planes of atoms in a polar material are treated like a classical capacitor. Between these planes, a dipole moment

exists. The longitudinal motion parallel to the direction of the dipole dramatically changes the energy stored in the capacitor compared to the transverse motion. Several analytical forms have been developed to describe this long-range interaction; the original description being the Fröhlich model [86]

$$g_{\mathbf{q}\nu}^{\text{Fröhlich}} = \frac{i}{|\mathbf{q}|}\sqrt{\frac{e^2\,\hbar\omega_{\text{LO}}}{2\epsilon_0\,V_{\text{cell}}}}\sqrt{\frac{1}{\varepsilon^{\infty}}-\frac{1}{\varepsilon^{0}}}, \tag{3.10}$$

where ω_{LO} corresponds to the frequency of the longitudinal optical mode, ε^0 is the static dielectric constant, and ε^∞ is the high-frequency dielectric constant. In the Fröhlich model, it is assumed that the material is isotropic and has only one LO mode. Generalizations to isotropic materials with more than one LO mode have been well-documented, and a useful summary may be found in Ref. [87]. One common feature in all of these models is the $1/q$ behavior of $g_{\mathbf{q}\nu}$.

The form of the Fröhlich model can be generalized to account for more complex electronic and atomic structures. We present here the generalized form of the Fröhlich model in the context of current computational techniques. State-of-the-art methods for calculating electron-phonon matrix elements on dense grids use Wannier interpolation (see Section 2.4.3) based on a DFPT calculation with a coarse grid. This is significantly more computationally efficient compared to performing DFPT explicitly on a dense grid. This Wannier interpolation scheme is implemented in the EPW program [88]. Due to the slow decay of $1/q$ behavior, the scattering off of LO polar modes is not localized and thus poorly described with Wannier functions. Thus, scattering off LO polar modes is treated separately from contributions of other phonon modes as a long-range contribution [88]. The total electron-phonon matrix elements $g_{mn,\nu}(\mathbf{k},\mathbf{q})$ are calculated using [88]

$$g_{mn,\nu}(\mathbf{k},\mathbf{q}) = g^{S}_{mn,\nu}(\mathbf{k},\mathbf{q}) + g^{L}_{mn,\nu}(\mathbf{k},\mathbf{q}), \tag{3.11}$$

where $g^S_{mn,\nu}$ is the short-range contribution. The long-range contribution, $g^L_{mn,\nu}$ is computed with [89, 90, 91]

$$g^L_{mn,\nu}(\mathbf{k},\mathbf{q}) = i\frac{e^2}{V_{cell}\varepsilon^0}\sum_\kappa \sqrt{\frac{\hbar}{2M_\kappa\omega_{\mathbf{q},\nu}}} \times \sum_{\mathbf{G}\neq\mathbf{q}} \frac{(\mathbf{q}+\mathbf{G})\cdot\mathbf{Z}^*_\kappa\cdot\mathbf{e}_{\kappa,\nu}(\mathbf{q})}{(\mathbf{q}+\mathbf{G})\cdot\boldsymbol{\varepsilon}^\infty\cdot(\mathbf{q}+\mathbf{G})}\langle\psi_{m,\mathbf{k}+\mathbf{q}}\left|e^{i(\mathbf{q}+\mathbf{G})\cdot\mathbf{r}}\right|\psi_{n,\mathbf{k}}\rangle, \quad (3.12)$$

where $\mathbf{G}$ is a reciprocal lattice vector, $\mathbf{Z}^*_\kappa$ is the Born effective charge tensor, $\mathbf{e}_{\kappa,\nu}(\boldsymbol{q})$ is the polarization vector associated with phonon wavevector $\mathbf{q}$ of mode ν for atom κ, and ε^∞ is now a tensor. For the cubic phase, there is only one unique element. The sum over $\mathbf{G}$ reciprocal lattice vectors is to account for the periodicity of the lattice [90]. The electron-phonon matrix elements are also weighted by the overlap between initial and final electronic states, $\langle\psi_{m,\mathbf{k}+\mathbf{q}}\left|e^{i(\mathbf{q}+\mathbf{G})\cdot\mathbf{r}}\right|\psi_{n,\mathbf{k}}\rangle$. This form of the long-range component of the matrix elements is analogous in form to the Fröhlich model. Unlike the Fröhlich model however, it holds for materials of any arbitrary symmetry or number of LO modes, making it applicable for understanding the electron-phonon interaction in chemically complex, low-symmetry structures. Previous calculations on GaAs [90], SnO_2 [92], GaN [93], and various oxides [94, 95, 96, 97] have shown such analytic models, including those proposed by Fröhlich [86] and Vogl [89], can successfully describe $g^L_{mn,\nu}$ for polar materials.

The basic idea for interpolation of the electron-phonon matrix elements is to first substract out the long-range contribution using Eq. 3.12 from the full matrix elements calculated from DFPT, then perform interpolation via Wannier functions on the short-range component, and finally add back the long-range contribution on the dense grid. The long-range component accounts for the contributions leading to the long-wavelength divergence, and leaving the remaining parts in the short-range contribution. A more

in-depth description of the history and methodology for describing electron-phonon interactions with Wannier functions is given in Ref. [98]. We note that in our calculations, all the phonon modes are included in the electron-phonon matrix elements.

3.3 Fermi's Golden Rule

Many properties of interest involve integrals over the Brillouin zone. To describe the transitions between electronic states, e.g., through scattering or excitations, a common approximation is Fermi's Golden rule. Such electronic transitions or scattering events between states are treated using first-order perturbation theory.

$$\Gamma_{i\to f} = \frac{2\pi}{\hbar} |\langle \psi_m | \mathcal{H}' | \psi_n \rangle|^2 D. \tag{3.13}$$

This equation represents a transition rate from state ψ_n of band n to ψ_m of band m by perturbation $\mathcal{H}'$, where D is the density of states. A key assumption in Fermi's Golden rule is the expectation that the probability amplitude of the initial state falls off exponentially with time (see Ref. [99] for a derivation). Fermi's Golden Rule also assumes that all secondary transitions within the continuum of states are neglected. The quantum mechanical descriptions of transport and optical properties presented in this thesis are both based on Fermi's Golden rule. That is, many calculations for materials properties that describe electronic transitions involve integrating over some matrix element like $\mathcal{H}'$ denoting some interaction between the particles of interest, multiplied by the occupation factors for the particles of interest and a term that imposes energy and/or momentum conservation.

We shall see in Sections 3.4 and 3.5 that the calculation of mobility and optical absorption stems from Fermi's Golden Rule.

3.4 Mobility with the Boltzmann Transport Equation

In this section, a basic outline of the Boltzmann transport equation is presented. The calculation of mobilities in WO_3 is presented in Chapter 6.

3.4.1 Boltzmann Transport Theory

Boltzmann Transport theory describes the thermodynamic statistical distribution of carriers of various momenta under non-equilibrium conditions. The Boltzmann Transport equation (BTE) is a statement of the conservation of particles in time and space in an incompressible phase space, and solutions to this differential equation describe the dynamic behavior of some particle of interest—electrons in this case. The reader is referred to Refs. [26, 77, 100] for additional details on derivations and background. The BTE is expressed as

$$\frac{\partial f}{\partial t} + \dot{\mathbf{r}} \cdot \frac{\partial f}{\partial \mathbf{r}} + \dot{\mathbf{k}} \cdot \frac{\partial f}{\partial \mathbf{k}} = \left(\frac{\partial f}{\partial t}\right)_{\text{coll}} \equiv \mathcal{I}_{\mathbf{k}}, \tag{3.14}$$

where the spatial and time variation of the distribution of electrons is described through the collision integral $\mathcal{I}_{\mathbf{k}}$, which is dependent on $\mathbf{r}$, $\mathbf{k}$, and t; $f = f(\mathbf{r}, \mathbf{k}, t)$ is the distribution of electrons.

A common model for $\mathcal{I}_{\mathbf{k}}$ is known as the relaxation time approximation,

$$\mathcal{I}_{\mathbf{k}}\{f\} = -\frac{f(\mathbf{r}, \mathbf{k}, t) - f^0(\mathbf{r}, \mathbf{k})}{\tau(\epsilon(\mathbf{k}))}, \tag{3.15}$$

which describes how small deviations in the local equilibrium particle distribution relax to the equilibrium distribution in some characteristic time τ that is allowed to have some

energy dependence. The local equilibrium distribution is described by the Fermi-Dirac distribution

$$f^0(\mathbf{r},\mathbf{k},\mathbf{t}) = \Big\{\exp\Big(\frac{\epsilon(\mathbf{k})-\mu(\mathbf{r},t)}{k_bT(\mathbf{r},t)}\Big)+1\Big\}^{-1}. \tag{3.16}$$

To obtain solutions to BTE, we write the actual distribution f as

$$f(\mathbf{r},\mathbf{k},t) = f^0(\mathbf{r},\mathbf{k},t) + \delta f(\mathbf{r},\mathbf{k},t), \tag{3.17}$$

and solve for the deviations away from the local equilibrium distribution δf. To make the problem mathematically tractable, we use a linearized version of the BTE that assumes the system is always close to equilibrium, which is

$$\frac{\partial \delta f}{\partial t} - \frac{e}{\hbar c}\mathbf{v}\times\mathbf{B}\cdot\frac{\partial \delta f}{\partial \mathbf{k}} + \mathbf{v}\cdot\left[e\cdot\mathbf{E} + \frac{\epsilon-\mu}{T}\nabla T\right]\Big(-\frac{\partial f^0}{\partial \epsilon}\Big) = \mathcal{I}_{\mathbf{k}}, \tag{3.18}$$

where $\mathbf{B}$ is the magnetic field and $\mathbf{E}$ is the electric field. The velocity $\mathbf{v}$ of these electrons may be calculated with $\mathbf{v} = 1/\hbar\vec{\nabla}_k\epsilon_k$. We consider the case of a spatially uniform but temporally fluctuating electric field $\mathbf{E} = \mathbf{E}_0 e^{-i\omega t}$, and assume $\mathbf{B} = 0, \nabla T = 0$. That is,

$$\frac{\partial \delta f}{\partial t} + e\mathbf{v}\cdot\mathbf{E}\Big(-\frac{\partial f^0}{\partial \epsilon}\Big) = \mathcal{I}_{\mathbf{k}} = -\frac{\delta f}{\tau(\epsilon(\mathbf{k}))}, \tag{3.19}$$

where we have rewritten Eq. 3.15 in terms of δf using Eq. 3.17. The solution to this differential equation is

$$\delta f(\mathbf{k}) = \frac{e\mathbf{E}_0\cdot\mathbf{v}\cdot\tau(\mathbf{k})}{1-i\omega\tau(\mathbf{k})}\Big(-\frac{\partial f^0}{\partial \epsilon}\Big)e^{i\omega t}. \tag{3.20}$$

At DC conditions ($\omega = 0$), assuming that the system is initially in equilibrium (i.e.,

$t = -\infty, \delta f = 0$), the solution to the BTE is then

$$\delta f(\mathbf{k}) = e\mathbf{E}_0 \cdot \mathbf{v}\Big(-\frac{\partial f^0}{\partial \epsilon}\Big)\tau(\mathbf{k}). \tag{3.21}$$

With knowledge of δf, we are able to relate deviations from the equilibrium distribution to the current density as

$$j^\alpha(\mathbf{r}, t) = -2e \int_{BZ} \frac{d\mathbf{k}}{(2\pi)^3} \delta f \cdot v^\alpha \tag{3.22}$$

$$= 2e^2 E_0^\beta \int \frac{d\mathbf{k}}{(2\pi)^3} \tau(\mathbf{k}) v^\alpha(\mathbf{k}) v^\beta(\mathbf{k}) \Big(-\frac{\partial f^0}{\partial \epsilon}\Big), \tag{3.23}$$

where α and β are Cartesian coordinate components and the factor of two accounts for spin. This current density can be related to the electrical conductivity via $j^\alpha = \sigma_{\alpha\beta} E_\beta$. From here, we can directly extract the electrical conductivity to be

$$\sigma_{\alpha\,\beta} = 2e^2 \int \frac{d\mathbf{k}}{(2\pi)^3} \tau(\mathbf{k}) v^\alpha(\mathbf{k}) v^\beta(\mathbf{k}) \Big(-\frac{\partial f^0}{\partial \epsilon}\Big). \tag{3.24}$$

Of note is that the conductivity is a property of the Fermi surface, as determined by $\Big(-\partial f^0/\partial \epsilon\Big)$.

It is possible to evaluate the conductivity explicitly for the free-electron gas and recover the Drude model discussed in Section 3.1.1. Using the Drude model readily allows us to write $\epsilon(\mathbf{k}) = \hbar^2\mathbf{k}^2/2m^*$, which thus makes $v^\alpha = 1/\hbar \nabla_\alpha \epsilon(\mathbf{k}) = \hbar k^\alpha / m^*$. Assuming $\tau(\mathbf{k})$ is constant, we can write the conductivity as [28]

$$\sigma_{\alpha\,\beta} = -2e^2 \frac{1}{\hbar} \tau \int \frac{d\mathbf{k}}{(2\pi)^3} v^\alpha(\mathbf{k}) \Big(\frac{\partial f^0}{\partial k^\beta}\Big), \tag{3.25}$$

where we have made the use of

$$\mathbf{v}(\mathbf{k})\Big(-\frac{\partial f^0}{\partial \epsilon(\mathbf{k})}\Big) = -\frac{1}{\hbar}\Big(\frac{\partial f^0}{\partial \mathbf{k}}\Big). \tag{3.26}$$

Next substituting the expression for $\mathbf{v}$, applying integration by parts, and assuming the effective mass is a scalar, the conductivity becomes

$$\sigma_{\alpha\beta} = 2e^2\frac{1}{\hbar}\tau\int\frac{d\mathbf{k}}{(2\pi)^3}\Big(\frac{\partial \mathbf{v}}{\partial \mathbf{k}}\Big)f^0 \tag{3.27}$$

$$= 2e^2\tau\int\frac{d\mathbf{k}}{(2\pi)^3}\frac{1}{m^*}f^0 \tag{3.28}$$

$$= \frac{ne^2\tau}{m^*}. \tag{3.29}$$

From Eq. 3.27, we have recovered the phenomenological Drude model. However, as discussed in Section 3.4.2, assuming a constant relaxation time τ and single parabolic band is inaccurate in more complex materials such as d-band perovskites. Not only are the bands in d-band perovskites not parabolic, first-principles calculations show the scattering rate is far from constant.

Section 3.4.2 continues the discussion of the specific form of the conductivity and scattering rate used in this dissertation. Many forms exist for the choice of the relaxation time τ, depending on the approximations made and what kind of scattering phenomena are being described (e.g., electron-electron scattering). In this dissertation, we focus on scattering as mediated by the electron-phonon interaction.

3.4.2 Mobilities from First Principles

Mobilities are derived from the electronic conductivity, $\mu = \sigma/ne$. For the purpose of studying transport properties we focus on the cubic phase of WO_3. We will specifically

be interested in the influence of spin-orbit coupling (SOC) (described in Section 3.6). The reason for focusing on the cubic phase is motivated in Chapter 6; here, we present the methodology.

In a cubic crystal the mobility is isotropic. We compute the conductivity tensor based on the Boltzmann transport theory, given as

$$\sigma_{\alpha\,\beta} = \frac{e^2}{V_{\text{cell}}} \sum_{n,\mathbf{k}} w_{\mathbf{k}} \tau_{n\mathbf{k}} \left(-\frac{\partial f_{n\mathbf{k}}}{\partial \epsilon_{n\mathbf{k}}} \right) v_{n\mathbf{k},\alpha}\, v_{n\mathbf{k},\beta} \tag{3.30}$$

where $w_{\mathbf{k}}$ is the $\mathbf{k}$-point weight, V_{cell} is the cell volume, $f_{n\mathbf{k}}$ is the Fermi-Dirac distribution function, and $v_{n\mathbf{k}} \equiv 1/\hbar \times \partial \epsilon_{n\mathbf{k}}/\partial \mathbf{k}$ are band velocities. The integral form in Eq. 3.24 has been transformed into a sum over discrete points in the Brillouin Zone. When spin-orbit coupling is included, the sum over bands n implicitly includes a sum over total angular momentum $j = l \pm 1/2$ states [101].

When calculating electronic conductivity, it is common to assume a constant scattering rate τ^{-1} [102]. First-principles approaches in which the energy and $\mathbf{k}$ dependence of the scattering rate are fully taken into account have only recently emerged [94, 95, 103, 104, 105, 96, 97]. These studies have shown that the scattering rate has a strong dependence on band and $\mathbf{k}$ vector that must be taken into account. In our calculations, the band- and $\mathbf{k}$-dependent scattering rate $\tau^{-1}_{n,\mathbf{k}}$ is calculated using [94]

$$\tau^{-1}_{n\mathbf{k}} = \frac{2\pi}{\hbar} \sum_{\mathbf{q}\nu,m} |g_{mn,\nu}(\mathbf{k},\mathbf{q})|^{\mathbf{2}} \cdot \Big\{ \left(\mathbf{n}_{\mathbf{q}\nu} + \mathbf{f}_{\mathbf{k+q},\mathbf{m}}\right) \delta\left(\epsilon_{\mathbf{k+q},\mathbf{m}} - \epsilon_{\mathbf{k},\mathbf{n}} - \hbar\omega_{\mathbf{q}\nu}\right) + \left(1 + n_{\mathbf{q}\nu} - f_{\mathbf{k+q},m}\right) \delta\left(\epsilon_{\mathbf{k+q},m} - \epsilon_{\mathbf{k},n} + \hbar\omega_{\mathbf{q}\nu}\right) \Big\}, \tag{3.31}$$

where $g_{mn,\nu}(\mathbf{k},\mathbf{q})$ are electron-phonon coupling matrix elements, and $n_{\mathbf{q}\nu}$ and $f_{m,\mathbf{k+q}}$ are phonon and electron occupation factors described by Bose-Einstein and Fermi-Dirac distributions. Bands are indexed by m and n, while phonons are indexed by wavevector

$\mathbf{q}$ and frequency ν. In Eq. 3.31, we see the form of Fermi's Golden rule. The electron-phonon matrix elements describe the interaction of electrons with the vibrating lattice. The δ functions ensure energy conservation in the electron-phonon scattering processes.

3.5 Optical Spectra Using First-Principles Calculations

The interaction of light with condensed matter plays a large role in optoelectronic devices. Within the context of this dissertation, we are interested in understanding the role of exccess carriers in optical absorption. Calculations that describe the influence of sturctural distortions on the absorption spectra are described in Chapter 7.

The basis of understanding the optical response of a material also rests on Fermi's Golden Rule. Here, the perturbing potential is taken from the electronic dipole approximation. The dipole approximation assumes that the wavelength of the incident light that leads to transitions between bound states is much larger than the length scale of the atom. Thus, incident radiation of the form $\exp(i\mathbf{k}\cdot\mathbf{r}) \approx 1+i\mathbf{k}\cdot\mathbf{r}+...$ can be approximated as unity, allowing us to neglect position dependence of the electric field. Perturbation by electromagnetic radiation entails a Hamiltonian with a modified momentum that includes a vector potential $\mathbf{A}$ for an object of mass m_0 and charge e,

$$\mathcal{H} = \frac{1}{2m_0}\left[\mathbf{p} - \frac{e}{c}\mathbf{A}\right]^2 + U, \tag{3.32}$$

where the electric field $\mathbf{E}(\mathbf{r},t) = -\frac{\partial}{\partial t}\mathbf{A}(\mathbf{r},t)$ may be easily obtained. Expanding the squared term in Eq. 3.32 and neglecting the $\mathbf{A}^2$ term, we recover the unperturbed Hamiltonian and now have a perturbative term containing terms of the form $\mathbf{A}\cdot\mathbf{p}$ from which the optical matrix elements are derived. Each of the optical matrix elements

are calculated assuming linearly polarized, monochromatic light.

3.5.1 The Complex Dielectric Function

The central quantity in calculating the optical spectra is the complex dielectric function, which is a measure of how a material responds to external electric fields. In the context of this thesis, we are interested in the absorption spectra due to excess carriers making interband transitions in which the crystal momentum is conserved. The macroscopic method for calculating the dielectric function (see Refs. [28, 106]) is obtained using Maxwell's equations that relate the response function in a medium to electric and magnetic fields. Here, we present a microscopic microscopic framework for calculating the dielectric function.

The absorption coefficient as a function of photon frequency ω can be expressed as

$$\alpha(\omega) = \frac{\omega}{n_r c}\varepsilon_2\,, \tag{3.33}$$

where $n_r(\omega)$ is the index of refraction, c the speed of light, and ε_2 the imaginary part of the dielectric function. The latter is given by (in atomic units) [107, 108, 109]

$$\varepsilon_2(\omega) = 2\frac{4\pi^2 e^2}{\omega^2}\frac{1}{V_{cell}}\frac{1}{N_{\mathbf{k}}}\sum_{ij\mathbf{k}}|\hat{\mathbf{e}}\cdot\mathbf{p}_{ij}(\mathbf{k})|^2\times\Delta f\delta(\epsilon_{j,\mathbf{k}}-\epsilon_{i,\mathbf{k}}-\hbar\omega), \tag{3.34}$$

where $\hbar\omega$ and $\hat{\mathbf{e}}$ are the photon energy and polarization, $\mathbf{p}_{ij}(\mathbf{k})$ is the dipole transition matrix element between bands i and j, $\Delta f = (f_{i,\mathbf{k}} - f_{j,\mathbf{k}})$ contains occupation statistics for electrons, and $\epsilon_{i,\mathbf{k}}$ is the electron energy of band i at state $\mathbf{k}$. The δ function ensures energy conservation for the pair of electronic states separated by the photon energy $\hbar\omega$. The factor of two accounts for the spin degeneracy. Conversion to SI units involves a multiplicative prefactor of $1/4\pi\varepsilon_0$ where ε_0 is the vacuum permittivity. In general, ε_2 is

a tensor. In the cubic and disordered phases considered in Chapter 7, the response is isotropic.

The absorption coefficient (units 1/cm) for interband transitions based on the random phase approximation therefore is given as [93, 107, 110]

$$\alpha(\omega) = 2\frac{4\pi^2 e^2}{\omega c n(\omega)} \frac{1}{V_{cell}} \frac{1}{N_{\mathbf{k}}} \sum_{ij\mathbf{k}} |\hat{\mathbf{e}} \cdot \mathbf{p}_{ij}(\mathbf{k})|^2 \times \Delta f \delta(\epsilon_{j,\mathbf{k}} - \epsilon_{i,\mathbf{k}} - \hbar\omega). \tag{3.35}$$

It is possible to relate the imaginary part of the dielectric function to the real part using the Kramers-Kronig relations:

$$\varepsilon_1(\omega) = 1 + \frac{2}{\pi}\mathcal{P}\int_0^\infty d\omega' \frac{\omega' \varepsilon_2(\omega)}{\omega'^2 - \omega^2 + i\eta} \tag{3.36}$$

where $\mathcal{P}$ is known as the Cauchy principal value and η is a complex shift of the poles done for numerical purposes that effectively results in a Lorentzian smearing of the spectra. There is a factor of 2 to account for the fact that $\varepsilon_2(\omega > 0)$ is symmetric with $\varepsilon_2(\omega < 0)$. The Kramers-Kronig relations are used for complex functions that are analytical in the upper half of the complex plane. A necessary condition for a function to be analytical is causality. In basic terms, causality is the condition that there must be some external perturbation to cause a response of the system. Causality implies analyticity. Based on analyticity, it is possible to relate the real and imaginary parts of a complex function. The reader is referred to Refs. [107, 108, 111] for mathematical details.

Using the real and imaginary parts of the dielectric function, we can recast Eq. 3.35 in terms of ε_1 and ε_2. We present such equations in the following section.

3.5.2 Relation to Absorption and Reflectance Spectra

In many applications of interest, the transmittance, absorbance, and reflectance are desired. Here, we present the various ways to represent such quantities used in the context of this thesis. For a more complete catalogue of equations for calculating optical spectra, we refer the reader to Ref. [106].

We may define the complex refractive index $\tilde{n} = n_r + i\kappa$, where n is the index of refraction, which contains information on the phase velocity of the propagating wave in the medium, and κ is the extinction coefficient. The complex dielectric function is related to the complex refractive index via $\varepsilon(\omega) = \varepsilon_1(\omega) + i\varepsilon_2(\omega) = \tilde{n}^2$. This allows for the absorption coefficient α to be recast as

$$\alpha(\omega) = \frac{4\pi}{\lambda}\kappa = \frac{2\omega}{c}\mathrm{Im}(\sqrt{\varepsilon_1 + i\varepsilon_2}). \tag{3.37}$$

This is equivalent to

$$\alpha(\omega) = \sqrt{2}\frac{\omega}{c}\left[\sqrt{\varepsilon_1(\omega)^2 + \varepsilon_2(\omega)^2} - \varepsilon_1(\omega)\right]^{1/2}, \tag{3.38}$$

using the fact that the index of refraction may also be written as

$$n_r(\omega) = \left[\sqrt{\varepsilon_1(\omega)^2 + \varepsilon_2(\omega)^2} + \varepsilon_1(\omega)\right]^{1/2}/\sqrt{2}. \tag{3.39}$$

Based on the computed dielectric function, we can calculate optical spectra. In a medium with no reflection, the transmittance can be written as

$$T = \exp(-\alpha \cdot d), \tag{3.40}$$

where d is the sample thickness. For completeness, the reflectivity (unitless) is

$$R(\omega) = \left| \frac{\tilde{n}(\omega) - 1}{\tilde{n}(\omega) + 1} \right|^2 = \left| \frac{\sqrt{\varepsilon_1(\omega) + i\varepsilon_2(\omega)} - 1}{\sqrt{\varepsilon_1(\omega) + i\varepsilon_2(\omega)} + 1} \right|^2 . \tag{3.41}$$

Thus, knowledge of either the real or imaginary part of the dielectric function in combination with the Kramers-Kronig relations is sufficient to obtain other relevant optical spectra. We make use of these equations and discuss the absorption spectra for WO_3 as a function of structural distortions in Chapter 7.

3.5.3 Practical Calculation of the Optical Matrix Elements

Just as with transport properties, the calculation of the absorption requires a dense sampling of the Brillouin zone. Bloch wave functions calculated on the coarse grid are transformed into the maximally-localized Wannier basis [63]. In order to achieve dense meshes, we use Wannier interpolation, as described in Section 2.4.3.

In order to calculate Eq. 3.35, an accurate description of the band structure and eigenenergies is needed in addition to the calculation of the optical matrix elements. The calculation of the optical transition matrix elements requires calculating the dipole matrix elements. We calculate the dipole matrix elements via the matrix elements of the velocity operator, which are the generalized optical matrix elements. The matrix elements of the velocity operator are given by [107, 112, 113]

$$v_{nm,\alpha}(\mathbf{k}) = \langle \psi_{m\mathbf{k}} \,|\, \hat{v}_\alpha \,|\, \psi_{n\mathbf{k}} \rangle = \frac{1}{\hbar} \left\langle u_{m\mathbf{k}} \left| \frac{\partial \hat{H}(\mathbf{k})}{\partial k_\alpha} \right| u_{n\mathbf{k}} \right\rangle , \tag{3.42}$$

where α indicates a Cartesian direction. The matrix elements are calculated using first-order perturbation theory. A more convenient expression to calculate the velocity matrix

elements is [112]

$$v_{nm,\alpha}(\mathbf{k}) = \frac{1}{\hbar}\left[\frac{\partial \epsilon_{n\mathbf{k}}}{\partial k_\alpha}\delta_{nm} + (\epsilon_{m\mathbf{k}} - \epsilon_{n\mathbf{k}})\left\langle u_{n\mathbf{k}} \middle| \frac{\partial}{\partial_\alpha} \middle| u_{m\mathbf{k}} \right\rangle\right]. \tag{3.43}$$

Further details are given in Refs. [92] and [112].

3.6 Spin-orbit Coupling

Spin is a purely quantum mechanical property for particles such as electrons and describes the intrinsic angular momentum of such particles. An important phenomenon that arises from the electron spin is the interaction of this spin with the orbital motion of the electron itself, known as spin-orbit coupling (SOC). SOC can have profound impact on the electronic and vibrational structure of a material. This is explored in Chapter 6 on transport properties. Here, we present a semiclassical picture to provide intuition on the origins of SOC and then a brief overview of its quantum mechanical treatment.

3.6.1 A Semiclassical Picture

It is possible to understand the physical origins of SOC using a semiclassical model [114]. In this model, we consider the electron to have an orbit around the nucleus in much the same way planets orbit the sun. This model will immediately show why SOC is significant in compounds containing heavier elements.

The electron has a spin s and orbital angular momentum l, each with its own magnetic moment μ_s and μ_l. Associated with the orbit of the electron is a current I. This orbit sweeps out an area A that leads to a magnetic moment $|\mu| = |\mathbf{I}| \cdot A$ in a time period

$T = 2\pi/\omega$. Assuming a circular orbit, the magnetic moment is

$$|\mu| = |\mathbf{I}| \cdot A = \frac{-e}{T}\pi r^2 = \frac{-e\omega}{2\pi} \cdot \pi r^2 = -\frac{1}{2}e\omega r^2. \tag{3.44}$$

Using the definition of orbital angular momentum $|\mathbf{l}| = |\mathbf{r} \times \mathbf{p}| = m\omega r^2$, the magnetic moment for the orbital angular momentum is $\mu_l = \frac{-e}{2m}\mathbf{l}$; similarly for the magnetic moment of spin, $\mu_s = \frac{-g_s e}{2m}\mathbf{l}$, where g_s is a relativistic correction (around 2).

In the reference frame of the orbiting electron, the electron experiences a magnetic field due to the protons in the nucleus due to the apparent motion of the nucleus relative to the electron. This interaction is effectively a perturbation to the potential seen by the electron due to this apparent magnetic field.

The perturbing potential describing the SOC interaction is

$$V = -\mu_s \cdot \mathbf{B}_l = \frac{Ze^2\mu_0}{8\pi m^2 r^3}(\mathbf{s} \cdot \mathbf{l}). \tag{3.45}$$

where $\mathbf{B}_l$ is the apparent magnetic field seen by the electron and μ_0 is the magnetic permeability. While this treatment of SOC is semiclassical, we have arrived at the main components that describe SOC: namely 1) $(\mathbf{s}\cdot\mathbf{l})$, the interaction between spin and orbital angular momentum and 2) and the dependence on atomic number Z. As SOC is much weaker than the Coulomb interaction, it is treated perturbatively. An important effect of SOC is lifting degeneracies in the electronic structure, as we shall see in Chapter 6.

Since W is a heavy atom, we expect SOC to play an important role in WO_3. In Chapter 6 we will explore how SOC affects transport properties.

3.6.2 From the Schrödinger to the Dirac Equation

The Dirac equation contains relativistic corrections to the Schrödinger equation that can describe SOC. Following Refs. [108, 115], we provide a brief introduction to the Dirac equation. Including relativistic effects requires reformulating the kinetic energy as $T^2 = c^2\mathbf{p}^2 + m^2c^4$.

In the relativistic framework proposed by Dirac, the wave function is a 4-component spinor. The Dirac equation in the absence of external fields can be written as

$$\left[\frac{\mathbf{p}^2}{2m} + V(\mathbf{r}) - \frac{\mathbf{p}^4}{8m^3c^2} - \frac{\hbar^2}{4m^2c^2}\nabla V \cdot \nabla + \frac{\hbar}{4m^2c^2}\sigma \cdot (\nabla V \times \mathbf{p})\right]\psi = E\psi \tag{3.46}$$

The first two terms are the non-relativistic Hamiltonian found in the Schrödinger equation. The third term $\mathcal{H}_v = -\mathbf{p}^4/8m^3c^2$ is a relativistic correction to the kinetic energy. The fourth term $\mathcal{H}_d = -\hbar^2/4m^2c^2\,\nabla V \cdot \nabla$ is a relativistic correction to the potential, also known as the Darwin correction. The final term $\mathcal{H}_{so} = \hbar/4m^2c^2\,\sigma \cdot (\nabla V \times \mathbf{p})$ describes the perturbation due to spin-orbit coupling. In the centrosymmetric potential of an atom, the potential may be written as $\nabla V = (\mathbf{r}/r)(dV/dr)$, which gives the following form of the SOC perturbation

$$\mathcal{H}_{so} = \frac{\hbar}{4m^2c^2}\frac{1}{r}\frac{dV}{dr}\sigma \cdot \mathbf{l}, \tag{3.47}$$

where we have again used the definition of orbital angular momentum $\mathbf{l} = \mathbf{r} \times \mathbf{p}$. σ represents the Pauli spin matrices. In practice, it is possible to treat SOC perturbatively or fully by solving the Dirac equations self-consistently; existing DFT codes take various approaches. For example, VASP treats SOC perturbatively whereas Quantum Espresso can be used to solve the Dirac equations to generate fully relativistic pseudopotentials and include SOC self-consistently in calculations. We have found in our

calculations for WO_3 both approaches (and codes) to yield similar electronic structure. This is discussed in further detail in Chapter 6.

Chapter 4

Extrinsic and Intrinsic Defects in WO_3

Our investigation of high levels of doping in WO_3 begins with a study of defects and dopants. Defects and dopants can be intentionally or unintentionally incorporated, and significantly impact the electronic and optical properties of materials. Thus, it is important to thoroughly characterize the common defects and dopants that occur in WO_3.

First, we study doping with the alkali metals, as these are the typical dopants in devices with WO_3. Then, we look at oxygen vacancies, a defect that is frequently invoked to explain observed experimental phenomena in complex oxides. We shall see that both oxygen vacancies and alkali metal dopants are shallow donors. This result will serve as the foundation for the remaining chapters on mobility and optical absorption.

The results presented here are adapted from Ref. [116], with portions adapted from Ref. [117].

4.1 Calculation Methodology

In order to understand the thermodynamic and electronic behavior of alkali metal dopants and oxygen vacancies, we calculate the formation energy. The formation energy encapsulates the likelihood of a particular defect being incorporated in a system [58]. We first consider interstitial Li on the empty A site. The formation energy is defined as

$$E^f[\mathrm{Li}_i] = E_{\mathrm{tot}}[\mathrm{Li}_i] - E_{\mathrm{tot}}[\mathrm{WO_3}] + \mu_{\mathrm{Li}} + qE_F + \Delta^q, \tag{4.1}$$

where $E_{\mathrm{tot}}[\mathrm{Li}_i]$ is the total energy of a supercell containing one Li interstitial, $E_{\mathrm{tot}}[\mathrm{WO_3}]$ is the total energy of the same supercell of the pristine bulk structure; and μ_{Li} is the chemical potential of Li, i.e., the energy of the reservoir of atoms with which Li is exchanged. We choose the chemical potential of Li to reflect equilibrium with lithium oxide [118].

For the oxygen vacancy, the formation energy is similarly defined as

$$E^f[V_{\mathrm{O}}] = E_{\mathrm{tot}}[V_{\mathrm{O}}^q] - E_{\mathrm{tot}}[\mathrm{WO_3}] - \mu_{\mathrm{O}} + qE_F + \Delta^q, \tag{4.2}$$

where $E_{\mathrm{tot}}[V_{\mathrm{O}}]$ is the total energy of a supercell containing an oxygen vacancy, and μ_{O} is the chemical potential of oxygen. For a defect with charge q, electrons are exchanged with E_F, the Fermi level, as referenced to the valence-band maximum (VBM) of the bulk material. The final term, Δ^q, is a charge-state dependent correction due to the finite size of the supercell [57, 119], which allows the defect behavior to be extracted in the dilute limit.

Although the value of the chemical potential μ_{O} varies depending on the growth

conditions, limits on μ_O may be determined based on the stability of WO_3:

$$\Delta H^f(WO_3) = \mu_W + 3\mu_O \ , \tag{4.3}$$

where $\Delta H^f(WO_3)$ is the enthalpy of formation, μ_W is the chemical potential of the W referenced to the energy of metallic W, and μ_O is the chemical potential of the O referenced to the energy of an O_2 molecule.

Using HSE, we find for the monoclinic phase $\Delta H^f_{HSE}(WO_3)$ = –8.32 eV, which compares well with experiment [$\Delta H^f_{exp}(WO_3)$ = –8.73 eV [120]]; for the cubic phase, $\Delta H^f_{HSE}(WO_3)$ = –8.03 eV. The O-rich limit is given by μ_O = 0; the O-poor (i.e., W-rich) limit is given by $\mu_W = 0$.

4.2 Doping with Alkali Metals

We begin our analysis with alkali metal doping, and later compare with the case of oxygen vacancies. Monovalent species, such as H, Li, and Na, are commonly used as dopants, with Li being the most common due to its fast diffusivity.

Monovalent dopants are shallow donors. We are able to see this in the formation energy plot for the Li interstitial in Fig. 4.1. Figure 4.1 shows that only the +1 charge state is stable for all Fermi levels in the band gap. This means that when Li is inserted into the system, it donates its valence electron to the host system.

The physical origin for this shallow-donor behavior is related to the fact that the valence electronic states of alkali metals lie above the conduction-band edge of WO_3. This is evident when considering the density of states plots for the various dopants. We use the monoclinic phase as an example, but the same observations hold for other phases. Figure 4.2 compares the density of states of WO_3 doped with free carriers and with alkali

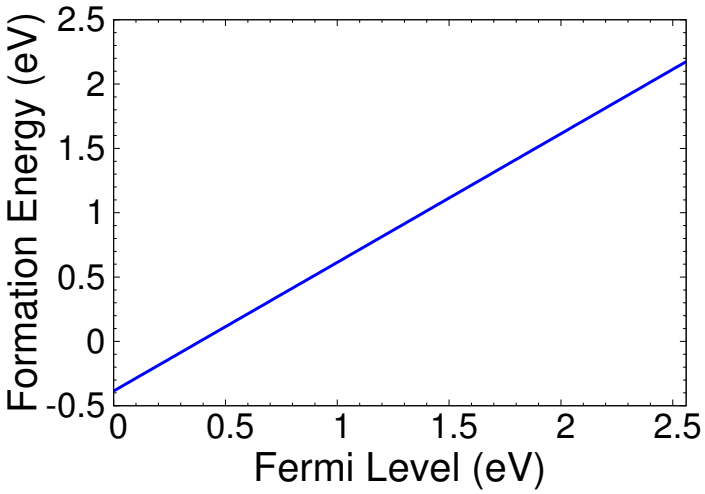

Figure 4.1: Formation energy of a Li atom intercalated in the monoclinic phase of WO_3 under oxygen-rich conditions; the zero of Fermi level is set to the valence-band maximum. The +1 charge state is the only stable charge state.

dopants. As seen in this comparison of density of states, doping with alkali metals is nearly identical to doping with only excess electrons. Little to no atomic contributions from the alkali dopant appears in the electronic density of states in the vicinity of the Fermi level. Both result in the Fermi level being shifted into the conduction band with only small differences in the final electronic structure.

We explore the influence of these excess carriers in the remaining chapters. Chapter 5 explores the interplay between the change in atomic and electronic structure at high carrier concentrations. Chapter 6 investigates the mobility and scattering of these carriers, and Chapter 7 looks into their optical response. Next, we calculate the formation energies and elucidate the electronic behavior for oxygen vacancies.

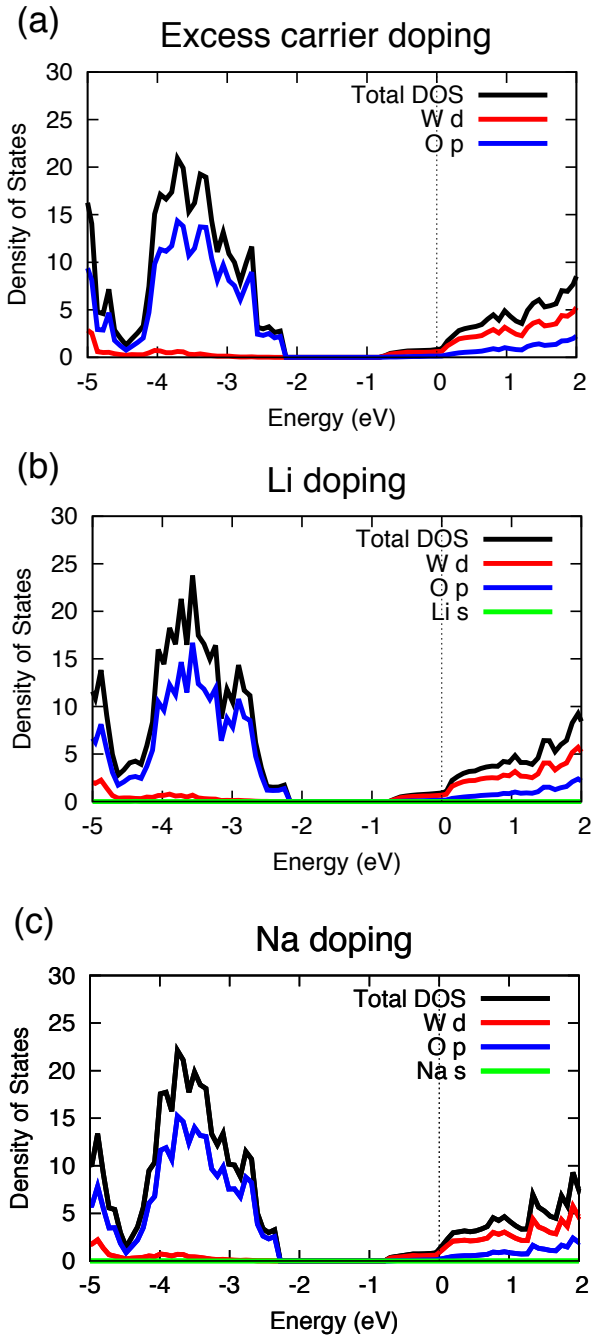

Figure 4.2: Comparison of density of states for the room-temperature monoclinic phase with (a) excess carrier doping, (b) Li doping, and (c) Na doping. The zero of energy is taken to be the Fermi level (dotted line)

4.3 Electronic Properties of Oxygen Vacancies

4.3.1 Motivation and Methodology

WO_3 is easily reduced and thus commonly found in substoichiometric compositions WO_{3-x} [121, 122]. It is thus important to understand how oxygen deficiencies influence the electronic and optical behavior of WO_3. Transport studies of single-crystalline monoclinic WO_3 have reported an increase in conductivity and electron carrier concentrations with increased oxygen deficiency [122], similar to the increase in conductivity that is observed in intercalated WO_3 [123, 17]. For electrochromic applications, monovalent elements such as Li or Na are typically intercalated, which causes a drop in optical transmittance at IR and visible wavelengths, and leads to coloration. However, the relationship between oxygen vacancies and electrochromism is far from understood. Some studies report higher optical density and higher coloration efficiency with higher levels of deficiency [122, 124].

The actual mechanism of how oxygen vacancies affect the electronic and optical behavior of WO_3 is still not well established. Some studies claim that polarons form for the neutral charge state V_O^0 and for V_O^+ [125, 126, 127, 128, 129], or that defect levels appear deep in the gap [130]. Others propose that oxygen vacancies lead to shallow levels near or resonant with the conduction band [131]. Thus, whether excess electrons from oxygen vacancies are localized or act like free carriers is unclear.

First-principles calculations using density functional theory (DFT) have already been used to study oxygen vacancies in WO_3, but many of these studies use the local density approximation (LDA) or generalized gradient approximation (GGA) for the exchange-correlation functional [132, 131, 126, 133]. Because LDA and GGA calculations severely underestimate band gaps, the results for the reported position of the oxygen vacancy levels in the gap carry large uncertainties. One study used the B3LYP hybrid functional,

which provides a better description of electronic structure, and found that oxygen vacancies induce levels in the gap, approximated from single-particle eigenvalues using Janak's theorem [130]. However, in order to accurately assess the stability of various charge states and draw conclusions about deep or shallow states, formation energies for different charge states need to be explicitly calculated. A discussion of the previous computational studies is included in Section 4.3.3.

Our goal is to understand the impact of oxygen vacancies on the electrical and optical properties of WO_3. We note that our results are for oxygen vacancies in the dilute limit in crystalline WO_3. We do not include crystallographic shear planes [121], in which the corner-sharing octahedra become edge-sharing and closer W-W distances occur, possibly leading to other phenomena. We consider various possible configurations of the oxygen vacancy for room-temperature (RT) monoclinic WO_3 (see Fig. 4.3), which is stable from room temperature to 600 K [29]. To provide further insight and allow comparisons with previous literature, we also performed calculations for the cubic phase. Since oxides such as WO_3 may display a tendency towards polaron formation [81], we also investigate self-trapping of electrons, both in bulk and in the vicinity of the vacancy. Our results show that the oxygen vacancy is a shallow donor that can cause n-type conductivity. We suggest that the excess electrons from oxygen vacancy donors provide a source for electrochromic behavior.

We use the HSE functional and the calculation parameters described in Section 2.6. To simulate an oxygen vacancy, an oxygen atom is removed from the supercell, and all the atomic coordinates are allowed to relax (until forces are below 0.05 eV/Å) while keeping lattice parameters fixed. The vacancy calculations use a 256-atom supercell for the monoclinic phase and a 108-atom supercell for the cubic phase, with a 400 eV energy cutoff. Convergence up to a 500 eV plane-wave energy cutoff was tested; lattice parameters changed by less than 0.25%. Integrations over the Brillouin zone

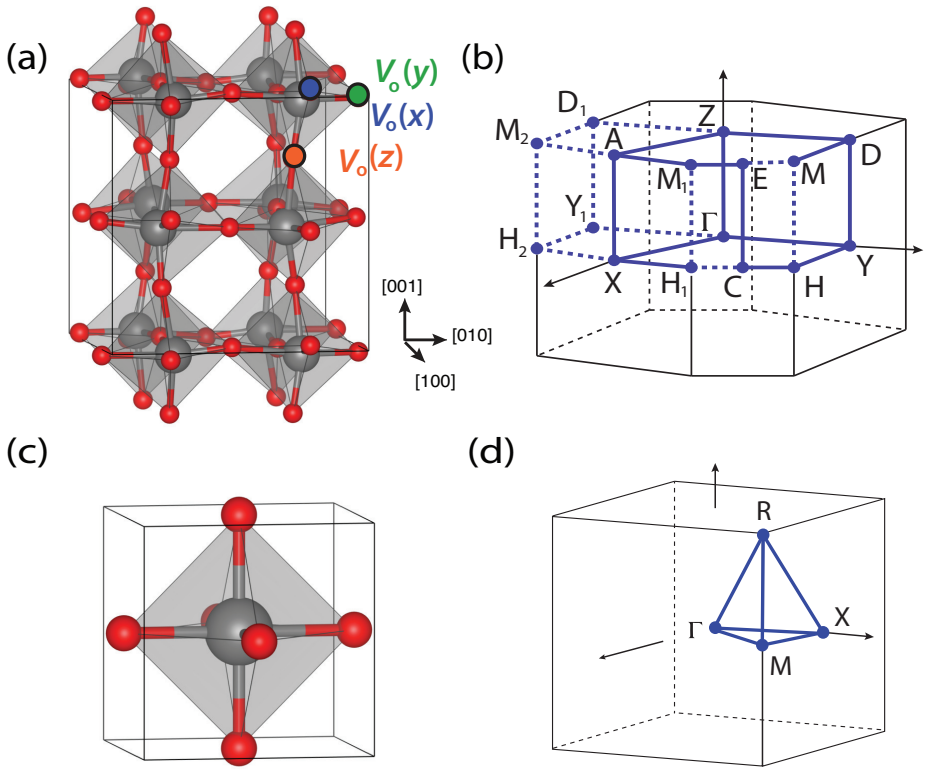

Figure 4.3: The two phases considered here are the monoclinic and cubic phases. (a) Unit cell of the room-temperature (RT) monoclinic phase of WO_3, indicating the distinct oxygen vacancy sites. (b) Corresponding Brillouin zone (determined using Ref. [134]). (c) Unit cell of cubic phase. (d) Corresponding Brillouin zone. For corresponding band structures, see Fig. 1.2.

were performed by using the special k-point $(\frac{1}{4}, \frac{1}{4}, \frac{1}{4})$; convergence up to $2 \times 2 \times 2$ **k**-point meshes was tested, resulting in formation energies changing by less than 0.1 eV. In the monoclinic phase, tilted and rotated octahedra and off-centered W atoms occur, resulting in three unique oxygen sites, as labeled in Fig. 4.3. The naming convention for differentiating between the oxygen vacancy sites is taken to be $V_{\mathrm{O}}^{q}(c)$, where q is the charge state and c is the cartesian direction along which the vacancy lies (referenced to neighboring W atoms). In the high-symmetry cubic phase, only one site for the oxygen vacancy needs to be considered. Spin polarization was included in all calculations involving unpaired electrons.

4.3.2 Results

Formation energies and charge-state transition levels

Formation energies for oxygen vacancies as a function of Fermi level E_F are shown in Fig. 4.4. The slope of each curve corresponds to the charge state of the defect. The formation energies are very similar in the monoclinic and cubic phases. For the monoclinic phase, the three possible oxygen sites were explored, resulting in similar properties for the vacancies. In both the monoclinic and cubic phases, we find no thermodynamic charge-state transition levels over the range of Fermi levels corresponding to the band gap.

Our results indicate that the oxygen vacancy acts as a shallow donor, stable only in the V_{O}^{2+} charge state; other charge states are not stable for Fermi levels within the band gap, at least with respect to excess carriers in the conduction band. However, in oxides such as WO_3, carriers may display a tendency towards polaron formation, i.e., self-trapping of electrons accompanied by a lattice deformation [81]. We therefore also investigated the possibility of polaron formation, first in the bulk. We added an extra

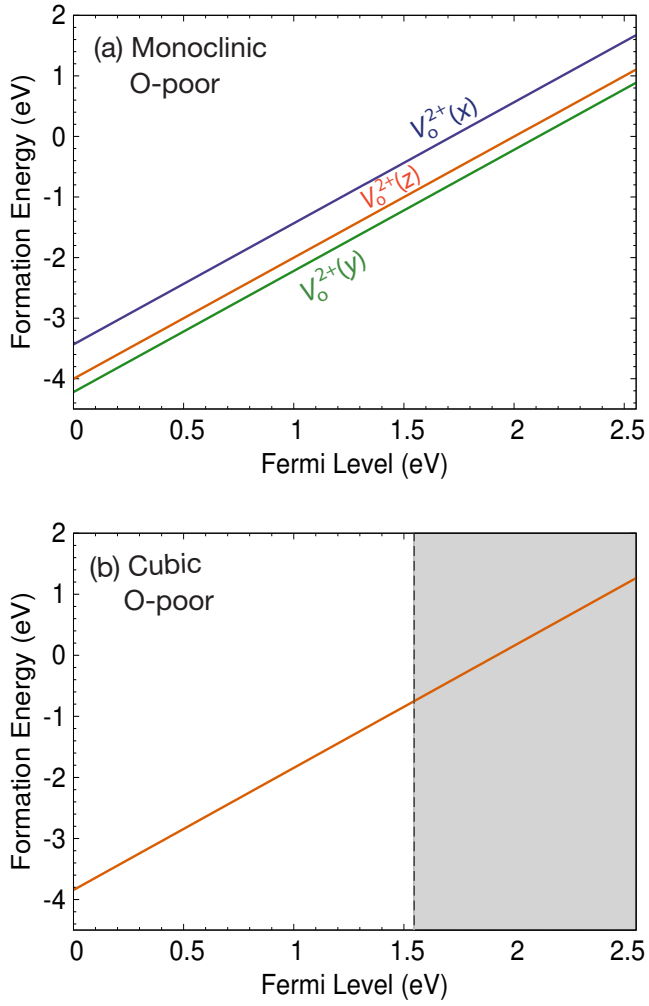

Figure 4.4: Formation energies of oxygen vacancies in oxygen-poor conditions for (a) monoclinic and (b) cubic phases of WO_3. In oxygen-rich conditions, formation energies are higher by an amount equal to $|\Delta H^f_{\mathrm{HSE}}(WO_3)|/3$. Fermi levels referenced to the VBM are shown for values in the band gap. For monoclinic, results for the three possible oxygen sites are included. For cubic, the vertical dotted line indicates the band gap; energies above the CBM are indicated in gray.

electron to the supercell and initialized the calculation by placing a magnetic moment on a chosen W atom and locally distorting the neighboring oxygen atoms to accommodate the formation of a polaron. We found that stabilizing a small polaron in the bulk was not possible; any attempt at charge localization accompanied by deformations was unstable, and the system returned to the bulk structure with a delocalized charge distribution. Using the same methodology as for the bulk polaron, we also explored the formation of a small polaron next to the vacancy in the form of W^{5+}, i.e., an excess electron localized on a W atom next to the V_O^{2+} (see also Section 4.3.3). However, we were similarly unable to stabilize either the V_O^{+} or V_O^{0} configuration, and thus we report no thermodynamic transition levels corresponding to these states.

The shallow behavior of oxygen vacancies explains the observed decrease in resistivity with increasing oxygen deficiency in monoclinic single crystals [122]. This increase in conductivity that occurs with higher oxygen deficiencies coincides with a greater degree of coloration [122]. This shallow-donor behavior of oxygen vacancies is therefore similar to what is observed with monovalent dopants like Na and Li. In alkali-doped WO_3, the atoms occupy the A site and contribute excess electrons to the conduction band as shallow donors (see Section 4.2 and Refs. [123, 17]), leading to increased electric conductivity [135]; simultaneously, electrochromic behavior is observed. We therefore postulate that the mechanism by which oxygen vacancies contribute to electrochromic behavior is also related to excess electrons, as it is for intercalated WO_3.

We note that $V_O(y)$ has the lowest formation energy among the three possible sites [Fig. 4.4] in the monoclinic phase. The difference in formation energy among the different oxygen vacancy sites correlates with the initial bond distance before the vacancy is introduced. $V_O(y)$ has the largest initial (as well as final) distance between W atoms adjacent to the vacancy; this will cause the bonding state to be the most energetically shallow. Relaxations and their correlation with electronic structure are discussed in

more detail in the next section.

Atomic Relaxations and Electronic Structure

Here we describe the atomic relaxations around the oxygen vacancy in the cubic phase. The relaxations for all atoms in the two octahedra nearest to the vacancy are shown for the V_O^{2+} charge state in Fig. 4.5. The W atoms next to the vacancy move outward, increasing their separation by around 6% (approximately 0.25 Å) with respect to the distance in the pristine bulk. Concomitantly, the W-O bonds along the direction defined by the W atoms and the vacancy are shortened by around 8% (approximately 0.15 Å). Four additional oxygen neighbors of the W atom lie in a plane perpendicular to the W-V_O-W direction; these O atoms move inwards, with the W-O bonds becoming 1% shorter compared to bulk.

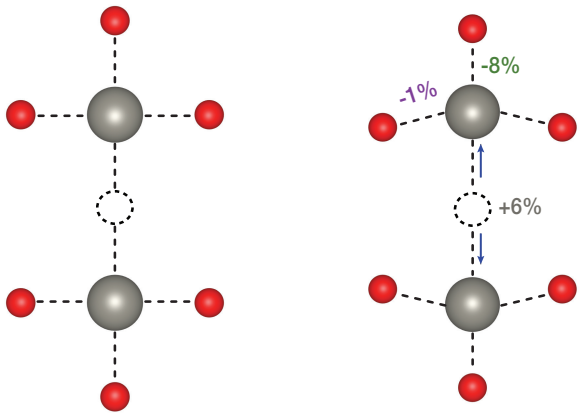

Figure 4.5: Structure of the unrelaxed (left) and relaxed (right) oxygen vacancy in the 2+ charge state in cubic WO_3. Large grey spheres represent W and small red spheres represent O. Relaxations are shown for octahedra nearest to the vacancy. Changes in bond lengths and distances are expressed as fractions of the corresponding quantities in the bulk crystal.

The monoclinic phase exhibits a similar pattern of atom relaxations around the oxygen vacancy, but with some differences among the $V_O(x)$, $V_O(y)$, and $V_O(z)$ sites

due to the anisotropy of the monoclinic phase. Relaxations for select neighbors of the vacancy are shown for the 2+ charge state in Fig. 4.6. The W neighbors of the vacancy move outward by 9% (approximately 0.35 Å) for $V_O(x)$ and 12% for $V_O(z)$, expressed as a percentage of the respective bulk equilibrium distances. The largest displacement of W atoms occurs for $V_O(y)$, with the W-W distance increasing by 15% (approximately 0.50 Å). The outward motion of the W causes their bonds with the next-nearest-neighbor O atoms along the W-V_O-W direction to be compressed, in some cases by up to 20%. Other W-O bonds may elongate or shorten depending on the specific relaxations of the W atoms.

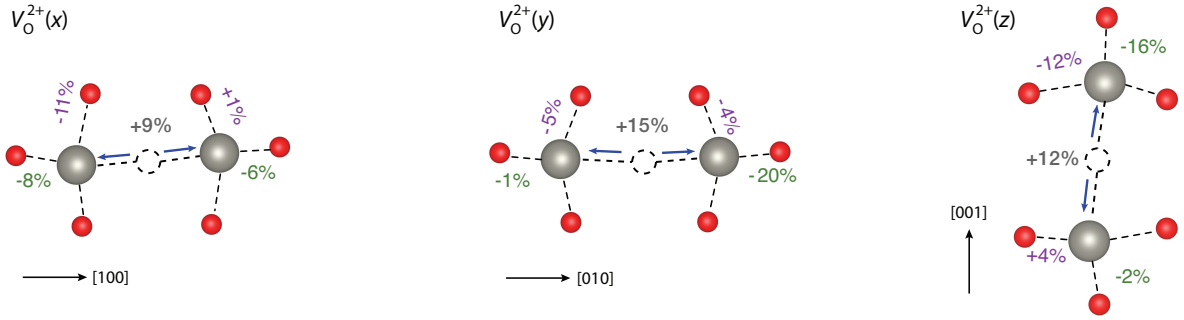

Figure 4.6: Structure of relaxed $V_O^{2+}(x)$ (left), $V_O^{2+}(y)$ (middle), and $V_O^{2+}(z)$ vacancies in the 2+ charge state in monoclinic WO_3. Large grey spheres represent W and small red spheres represent O. Relaxations are shown for select neighbors of the vacancy. Changes in bond lengths and distances are expressed as fractions of the corresponding quantities in the bulk RT monoclinic phase.

We now discuss the effect of these relaxations on the electronic structure. In principle, oxygen vacancies in WO_3 could be stable in three possible charge states: V_O^0, V_O^+, or V_O^{2+}. Removing an oxygen atom leaves two W dangling bonds with one electron each, which form a doubly occupied bonding state and an empty antibonding state in the case of a neutral vacancy (V_O^0). For the *unrelaxed* vacancy in monoclinic WO_3, the bonding state (Kohn-Sham state in the band structure) is at 0.50 eV below the CBM for $V_O(x)$, at 0.19 eV for $V_O(y)$, and at 0.06 eV for $V_O(z)$. The position of the bonding state depends strongly on the W-W distance, which is related to the overlap of the two W dangling

bonds.

The forces on the W atoms are outward, i.e., away from the vacant site. Upon relaxation of internal coordinates, the doubly occupied bonding state moves up in energy and becomes resonant with the conduction band as the W atoms relax away from the vacancy. The two electrons then occupy extended conduction-band states perturbed by the presence of the vacancy. This result should be interpreted as a doubly ionized vacancy (V_O^{2+}) with two electrons in the conduction band. Figure 4.7 shows charge density plots and the corresponding band structures, illustrating the transition from a localized state around the vacancy to a delocalized state upon relaxation, and the defect state becoming resonant with the conduction band.

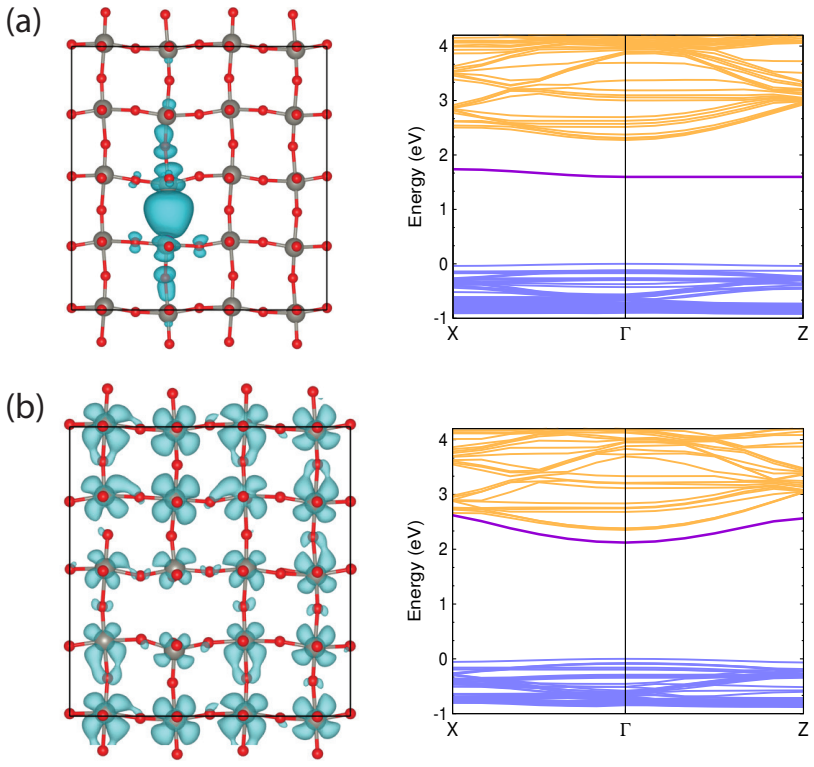

Figure 4.7: Charge density of the vacancy-induced state and band structure for $V_O^0(y)$, (a) before and (b) after atomic relaxation. Isosurfaces are shown at 10% of the maximum density and in the plane containing the vacancy. Large grey spheres represent W and small red spheres represent O. CBs are shown in orange, VBs in blue, and the band in purple corresponds to the charge density plots shown on the left.

Similarly, in the +1 charge state of the *unrelaxed* vacancy (V_O^+), a singly occupied spin-up state occurs in the band gap at 1.68 eV below the CBM for $V_O(x)$, 1.41 eV for $V_O(y)$, and 0.50 eV for $V_O(z)$, with a corresponding spin-down state resonant in the conduction band. Again, upon relaxation this occupied state moves above the CBM, leaving the band gap free of states and indicating that V_O^{2+} is the only stable charge state for the vacancy.

Observations on the Charge Density Distribution

A representative charge density plot is shown in Fig. 4.8. As expected for a shallow donor, an additional electron added to a supercell containing a V_O^{2+} occupies an extended conduction-band state perturbed by the presence of the vacancy. Intriguingly, in the case of $V_O(x)$ and $V_O(y)$ this state is not distributed over the entire supercell but is predominantly located on a specific plane of atoms. This type of charge distribution is consistent with the formation of a large polaron that is delocalized in two dimensions. This is observed for both the cubic and monoclinic structures. In order to make sure that this feature is not an artifact of our calculations, we perform two tests: 1) for the cubic phase, using a supercell oriented along different directions, effectively changing the boundary conditions to ensure interactions between supercells do not lead to artifacts; and 2) for the monoclinic phase, using a larger supercell.

In the first test, we start from the 108-atom cubic supercell, which is a 3×3×3 multiple of the 4-atom primitive cell. We rotate the lattice vectors by 45° about the z axis and create a new $2\sqrt{2} \times 2\sqrt{2} \times 3$ supercell with 96 atoms. We then introduce an oxygen vacancy, and allow the cell to relax in order to test for any artifacts happening at the cell boundary. As seen in Fig. 4.8(b), the planar distribution of charge density is still observed. In the second test, Fig. 4.8(c) shows that with a 384-atom supercell ($3 \times 3 \times 2$ supercell of the monoclinic unit cell), the planar distribution still extends to

the edges of the simulation cell, again suggesting this is not an artifact of our calculation parameters.

The atomic character of this charge density is predominantly derived from d_{xy} orbitals. Our calculations and tests demonstrate that the formation of a small polaron is not favorable, but formation of large polarons is quite likely in a material such as WO_3. Experiments have suggested a large-polaron radius of 8.5 Å [122]. We note that, in the absence of any localization, hydrogenic effective mass theory suggests a hydrogenic state with a radius of approximately 25 Å, using the lower limit of measured $\varepsilon = 12.1$ [136] and representative effective mass $m^* = 0.25m_0$ (calculated from our HSE band structure). The supercells used in our study are not large enough to capture the full extent of the observed charge densities, but they allow us to set a lower limit on the size of the large polaron [i.e., 22 Å in diameter as seen from Fig. 4.8(c)]. In order to rigorously investigate this planar feature, larger supercells are needed.

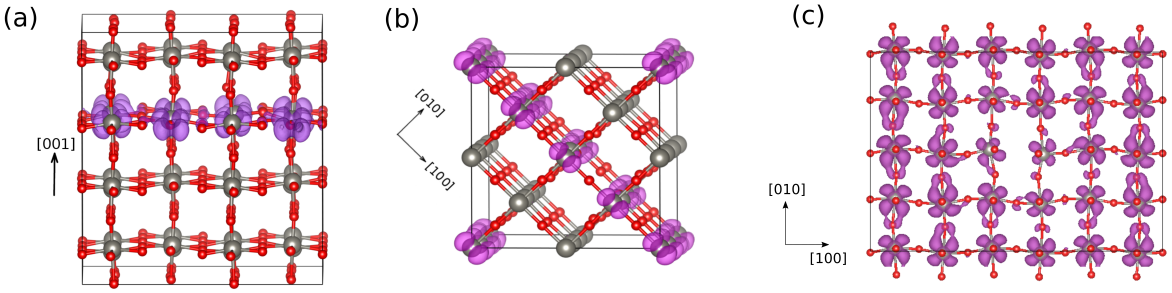

Figure 4.8: Charge densities illustrating in-plane localization in the same plane as the oxygen vacancy for (a) the $V_O^0(y)$ defect in monoclinic phase; similar planar localization is found for the $V_O^0(x)$, $V_O^{+1}(x)$, and $V_O^{+1}(y)$ charge states; (b) the oxygen vacancy in a cubic supercell with lattice vectors rotated by 45° about the z axis; (c) the 384-atom supercell with $V_O^0(x)$, shown in-plane of the oxygen vacancy for clarity.

Caution should thus be exercised in interpreting such phenomena. However, such a planar distribution of electrons has been observed in electron spin resonance (ESR) measurements of monoclinic WO_3 [137]. These ESR measurements described an unpaired electron with a two-dimensional spread of the wave function, exhibiting d_{xy} symme-

try similar to the W $5d$ conduction-band states. The observed planar distribution of electrons bound to V_O^{2+} therefore appears to be an actual feature of WO_3.

4.3.3 Discussion

Comparison with Previous Calculations

Absorption by deep defect levels has been proposed as a mechanism for electrochromism. Our results for oxygen vacancies do not support such a mechanism based on absorption. Our present results differ from those reported in a previous hybrid functional study for monoclinic WO_3, which found that the oxygen vacancy introduced deep levels in the gap [130]. The band gap in the B3LYP calculations of Ref. [130] (3.10 eV for the monoclinic phase) was significantly larger than our HSE value, as well as larger than experimentally measured gaps (see Table 1.2). We therefore investigated the possibility that a larger band gap might result in localization of oxygen vacancy states and lead to deep levels in the gap.

We performed two types of tests. First, we increased the mixing parameter up to as large as 50%. Up to 35% mixing (corresponding to a band gap of 3.05 eV), the charge density corresponding to the highest occupied state for V_O^0 remains delocalized, i.e., our conclusion about V_O being a shallow donor holds. This is illustrated in Fig. 4.9. With the standard mixing parameter of $\alpha = 0.25$, the band gap of the monoclinic structure is 2.56 eV, slightly underestimating the experimental band gap, which is reported to be $E_g = 2.80$ eV [138, 139, 140]. Increasing the mixing parameter to $\alpha = 0.30$ reproduces the experimental gap. As a variation to this test, we investigated structures obtained with a significantly higher (but unphysical) mixing parameter ($\alpha = 0.50$), for which strong charge localization occurs, and gradually reducing the mixing parameter in steps of 0.05 down to $\alpha = 0.25$. The band structures and charge density distribution for the

relaxed structures are shown for three mixing levels in Fig. 4.9; the band gap is 3.05 eV at $\alpha = 0.35$ and 3.93 eV at $\alpha = 0.50$. Figure 4.9 shows that even at mixing levels that result in band gaps on par with amorphous configurations [141, 38, 142] the charge density is delocalized across multiple atomic sites.

Second, we looked into different possible structures of the monoclinic phase, since we observed that several metastable configurations are possible and that the band gap is quite sensitive to the details of the structure. Indeed, the low symmetry of the monoclinic phase allows for a range of octahedral tilts and distortions and off-center positions of the W ions, and these structural parameters directly affect the band width of the *d*-derived conduction band and hence the band gap. The cubic phase, which has perfect octahedra, has the largest band width and hence the smallest band gap. Our results reported above are for the lowest-energy configuration of the monoclinic phase, obtained by consistently optimizing the lattice parameters and atomic positions, starting from different initial configurations. We can also obtain various metastable structures, and we investigated the oxygen vacancy defect in one of these structures that has a band gap of 3.00 eV, following the same methodology as above. The final conclusion is the same; namely, that the oxygen vacancy is a shallow donor, stable only in the 2+ charge state, in spite of the larger band gap of this structure.

The discrepancy between our results and those of Wang *et al.* [130] may be due to the difference in functionals, resulting in a significantly larger band gap in B3LYP than in HSE. Wang *et al.* [130] also reported that they still found localization of vacancy states (i.e., V_O^+, V_O^0) even when using an HF15LYP functional, which produces a gap of 2.72 eV. The HSE hybrid functional [52] has been verified to provide a reliable description of the electronic structure of a wide range of materials, while B3LYP (and HF15LYP) may overestimate the degree of localization [143, 48]. Indeed, the B3LYP functional was found to have difficulty describing the transition from localized to delocalized electrons.

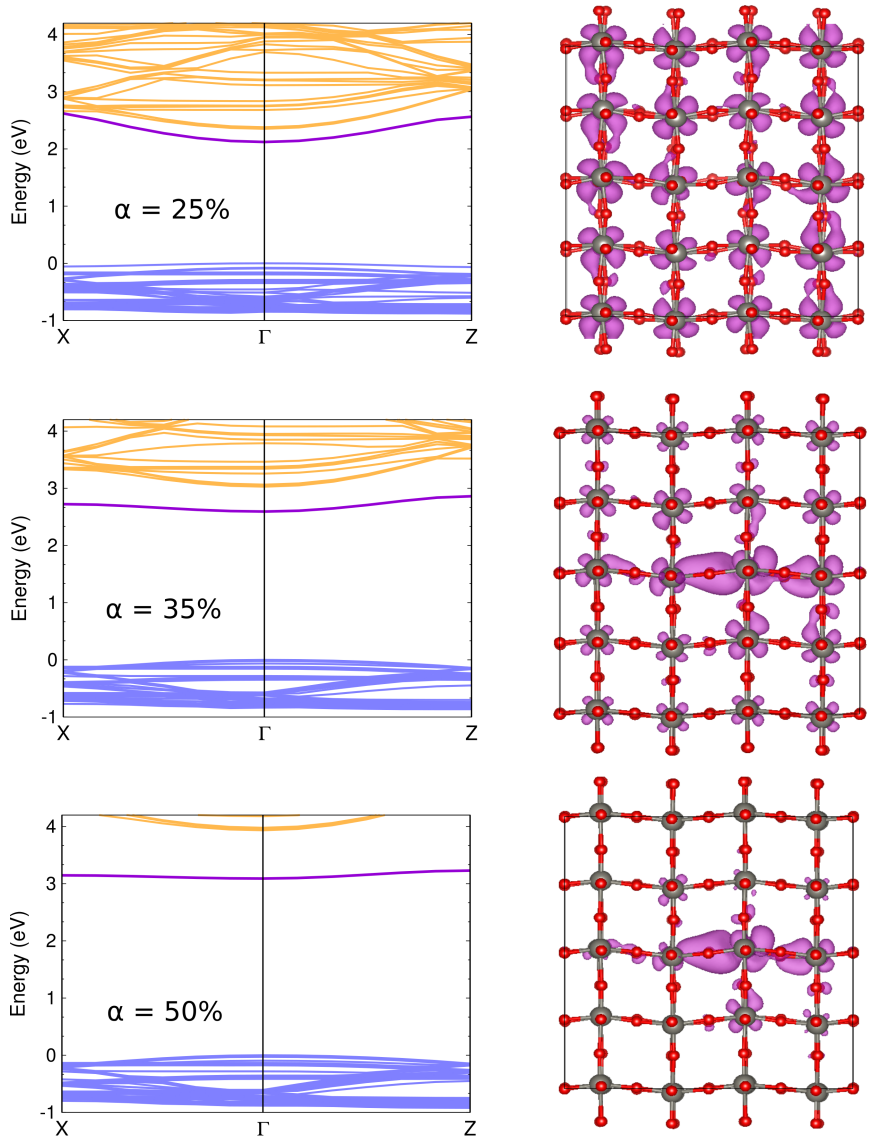

Figure 4.9: Band structure and charge density isosurfaces for the electrons bound to a neutral oxygen vacancy $V_O^0(y)$ in monoclinic WO_3, relaxed at various mixing parameters in HSE. The state associated with the defect level is shown in purple. Isosurfaces are shown at 10% of their maximum value.

Paier *et al.* [143] attributed most of the error to the LYP correlation energy, which cannot reproduce the homogeneous electron gas limit in periodic systems; the remaining error stems from the Becke exchange and choice of parameters used in the functional. The B3LYP functional thus artificially favors localization, an effect we have observed in our own comparisons of HSE and B3LYP calculations for oxygen vacancies in identical structures with all other input parameters kept the same.

We note that our choice of 25% mixing in the HSE functional is justified. The band gap in our calculations is in good agreement with experiment (see Table 1.2). In addition, a study on a very similar oxide, namely MoO_3, reported a band gap obtained with 25% mixing in HSE in excellent agreement with experiment [144]. We note that small polarons were actually found to be stable in MoO_3 using the same HSE functional and mixing parameter [145]. We attribute the greater tendency for localization in MoO_3 to the more localized character of the CB states, which are made up of $4d$ orbitals, as opposed to the $5d$ orbitals in WO_3.

Of equal importance, the 64-atom and 32-atom supercells used by Wang *et al.* [130] are too small to accurately describe the oxygen vacancy in the dilute limit. Removing one oxygen vacancy from a 256-atom supercell corresponds to a 0.5% concentration of oxygen vacancies. In 64- and 32-atom supercells, the corresponding concentrations are much higher: 2.1% and 4.2%. Creating an oxygen vacancy in these small supercells results in every other oxygen atom being removed along at least one direction, leading to strong spurious interactions between defects. These artifacts are particularly evident when one tries to perform supercell-size corrections and finds that the methodology of Ref. [57] cannot even be applied to these small cells. The unphysically high formation energy for the neutral oxygen vacancy reported in Ref. [130] (around 5.3 eV; 1.7 eV higher than our calculations in oxygen-rich conditions) can also be attributed to the small supercell size (as verified in our own calculations for small supercells). The spurious

interactions between defects in these small cells also inhibit the full relaxation of the W atoms surrounding the vacancy. As an example, for $V_O^0(x)$, the relaxed W-W distance in the 64-atom supercell is elongated by 2.6% of the bulk bond length, compared to 6.3% in the 256-atom supercell. This results in a more localized charge distribution around the oxygen vacancy.

Finally, we note that the use of the CRYSTAL09 code in the study of Wang *et al.* [130] forces them to *approximate* optical transitions using Kohn-Sham eigenvalues based on Janak's theorem, and make further approximations to obtain thermodynamic charge-state transition levels. They do not directly calculate formation energies of charged states, as we do in this work, which is required for a rigorous assessment of the stability of the charge states [58].

Implications for Optical and Electronic Properties of WO_3

Our results have several implications for electronic and optical properties of WO_3. The shallow-donor nature of the oxygen vacancy is consistent with the increase in conductivity with oxygen deficiency found in experiment, as discussed in Section 4.3.2. It is also in agreement with a study using Raman spectroscopy in which additional peaks assigned to the presence of W^{5+} emerged upon coloration in *amorphous* samples, but not in crystalline samples [146].

A number of mechanisms for electrochromism in WO_3 have been proposed; some are based on absorption by deep defect levels [130, 142, 11], some on polarons [147, 128, 127, 126, 129], and others on transitions of electrons in the conduction band from occupied to unoccupied levels [148, 149, 150, 151, 152]. Our results for oxygen vacancies do not support a mechanism based on absorption by deep levels. Our results also contrast with a proposed mechanism for the coloration of WO_3 based on transitions involving small polarons (e.g., W^{5+} centers). Our calculations show that in *crystalline* WO_3, no

localization of charge occurs, either in the bulk or in the vicinity of the oxygen vacancy, in agreement with ESR measurements [137].

It should be noted that amorphous WO_3 may behave differently from the crystalline material we focus on in the present study. Amorphous WO_3 has structural disorder that may promote charge localization around the vacancy [146, 153]. Furthermore, amorphous WO_3 has a significantly larger band gap than crystalline WO_3 [154, 155, 140], which leads to the formation of in-gap states, consistent with our findings when varying the mixing parameter (Sec. 4.3.3). Unlike previous studies [130] that make comparisons with results for amorphous structures, we have restricted our comparisons with reports on crystalline WO_3. Our conclusion that the oxygen vacancy is a shallow donor supports the proposed mechanism that electrochromism is mediated by excess carriers that make transitions to empty states, and explains why electrochromism is observed in crystalline WO_3 with oxygen deficiencies, similar to what is observed in intercalated WO_3.

4.3.4 Conclusions

In conclusion, we have demonstrated that the oxygen vacancy and alkali dopants in monoclinic and cubic WO_3 act as shallow donors. The only stable charge state for alkali dopants is +1. The oxygen vacancy is stable exclusively in the V_O^{2+} charge state; the V_O^{+} and V_O^{0} states are unstable. We explore how the electronic structure of alkali interstitials leads to shallow-donor behavior; and how the electronic structure of the oxygen vacancy is tightly coupled to the atomic relaxation of W atoms surrounding the vacancy: outward motion of W atoms moves the vacancy-induced states into the conduction band. The shallow-donor nature of the vacancy and alkali dopants is consistent with the observed trends in electrical conductivity and coloration in experiment. The lack of deep levels associated with V_O indicates that electrochromism cannot be explained in terms of ab-

sorption due to such levels. Neither is electrochromism associated with small polarons, which we also find be unstable in crystalline WO_3. Our results suggest that excess carriers are most likely responsible for the electrochromic properties of WO_3. We test this hypothesis in Chapter 7.

Chapter 5

Phase Transformations upon Doping in WO_3

We next study the effects of electron doping in the system and explore the physics behind the interplay between atomic and electronic structure in the structural phase transformations observed. The results presented here are adapted from Ref. [156].

5.1 Motivation and Methodology

The vacant A site in WO_3 enables high levels of doping up to stoichiometric compositions [157]. WO_3 has been observed to undergo structural changes to higher symmetry phases as a function of doping [158, 146, 15, 16, 157]. The ability to dope with a variety of foreign species makes the structure and electronic properties of WO_3 highly tunable.

At room temperature, WO_3 is monoclinic, with off-centered W ions surrounded by oxygens in distorted octahedra. As a function of doping, the highly distorted monoclinic phase transforms to a tetragonal, and ultimately to a cubic structure [146]. These transformations have been experimentally observed upon doping with Na [15, 157] and Li

[16]. A study from Wang *et al.* used *in situ* transmission electron microscopy to investigate the kinetics of dopant intercalation and structural transformation in Li-intercalated WO_3 [159]. Several computational studies have also investigated the influence of doping in WO_3. One such study compared and contrasted the electronic structure and bonding environment of ReO_3 with $NaWO_3$, which are isoelectronic [160]. Another study showed that the relaxed volume increases and the band gap decreases with the size of the dopant at low doping concentrations (∼4%) [161]. Walkingshaw *et al.* demonstrated, using density functional theory in the local density approximation (LDA), that the structural transformations could be decomposed into certain modes of distortion (e.g., changes of bond length in the xy-plane) [162]. However, the physical mechanisms of this structural transformation have not yet been fully explained.

In the present work, we distill the observed structural transformations to adding excess electrons to the system and elucidate the mechanisms of the structural phase transformations using density functional theory with a hybrid functional. We perform a detailed analysis of charge doping up to stoichiometric concentrations to understand the driving force for the structural transformation. We quantify the energetics of the transformation, and demonstrate that the lowering of the conduction bands between the monoclinic and higher symmetry phases is the energetic driving force.

Experimentally, the addition of electrons is achieved by doping with alkali atoms [15, 157, 16]; it could also be associated with the presence of oxygen vacancies [116]. Explicit inclusion of dopants or point defects in our calculations could affect the quantitative results and shift the computationally determined phase boundaries. Consideration of dopant-specific effects is beyond the scope of the present work; the complexity of that problem is illustrated by the differences observed between experimental results that nominally use the same dopant (e.g., Na, in Refs. [15] and [163]). Our goal in the present work is to show that essential physics is captured by focusing on the addition of

excess electrons.

The majority of our calculations are performed for pure charge doping; i.e., no dopant atoms are included, only electrons are added to the system. At least one point is calculated for every increment of $x = 0.0625$ electrons per formula unit up until $x = 0.75$, beyond which no further phase changes occur. A homogeneous compensating background provides charge neutrality, as is standard practice in first-principles calculations for charged systems [58]. In the real system, the electrons would be supplied by dopant atoms that become ionized, and these positive ions provide the compensating charge. Each calculation is initiated with the 32-atom RT monoclinic phase of WO_3 with a given amount of electron charge added. All calculations are converged until the residual forces are below 0.05 eV/Å, at which point the symmetry of the final structure is determined.

We use the calculation parameters outlined in Section 2.6. We tested **k**-point meshes up to $8 \times 8 \times 8$, and found that lattice parameters changed by less than 0.25%, volumes by less than 0.5%, and relevant energy differences by less than 15 meV per formula unit.

5.2 Results

A comparison of the structural motifs of the various polymorphs of WO_3 is presented in Section 6.3.1. Our calculated lattice parameters and band gaps for the unit cells of different phases shown in Fig. 1.1 are listed in Table 1.2 in Chapter 1. In the following section, we quantify the structural changes that occur with electron doping.

5.2.1 Phase Diagram with Electron Doping

We perform calculations at discrete values of electron concentrations, and report the phase observed for the lowest-energy structure at each concentration. We begin with the monoclinic structure at low electron concentrations. Due to this discrete sampling,

the electron concentrations at which phase boundaries occur are approximate. As these structural transformations are gradual, the marked phase boundaries represent not a sudden change in structure, but a rough delineation between two observed phases. We note that similar issues arise in an experimental determination of phase boundaries. In our computational approach, we base the phase boundaries on a collective examination of the structural parameters (lattice parameters and internal distortion of atomic coordinates) described below. Phase boundaries are indicated as solid vertical lines in Figs. 5.1 and 5.2.

Figure 5.1 illustrates the evolution of the lattice parameters, β angle, and volume as a function of electron concentration. The figure tracks the progression from the low-symmetry monoclinic phase where $a \neq b \neq c$ and $\beta > 90^o$ to the high-symmetry cubic phase where lattice parameters become equivalent and β approaches 90^o. The volume expansion shown in Fig. 5.1(c) is largely determined by the degree of tilting of the octahedra. A significant volume expansion occurs within the monoclinic phase upon addition of electrons, due to the decrease in the amount of tilting. Only a small amount of additional expansion occurs within the orthorhombic ($Pbcn$) and tetragonal ($P4/nmm$) phases.

The distortions of the internal coordinates are shown in Fig. 5.2. A useful metric for the overall distortion of the octahedra is the mean of the quadratic elongation parameter [164]

$$\langle \lambda_{oct} \rangle = \sum_{i=1}^{6} \frac{1}{6} \left(\frac{l_i}{l_0} \right)^2, \tag{5.1}$$

where l_0 is the bond length of the pseudocubic structure with the volume of the distorted perovskite and l_i is an actual bond length of the distorted perovskite; λ_{oct} is a measure of the distortedness of a perovskite from a cubic symmetry and is thus unity for the cubic phase. As shown in Fig. 5.2(a), the quadratic elongation parameter approaches unity as

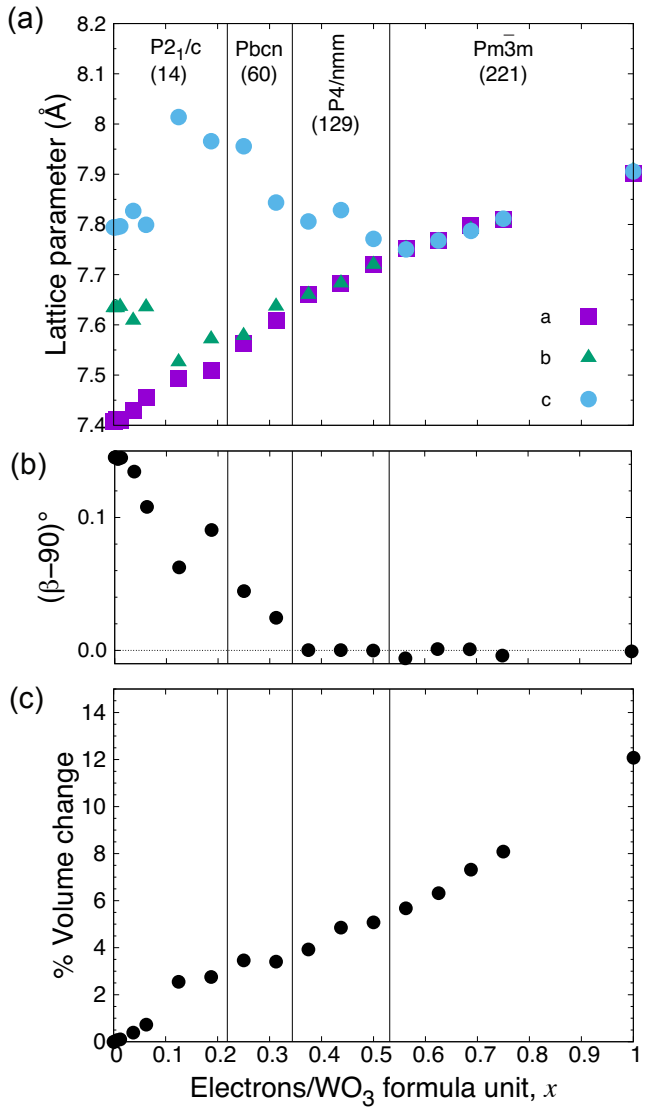

Figure 5.1: Evolution of (a) lattice parameters, (b) β angle, and (c) volume as a function of electron doping in HSE. Space groups and space-group numbers for the various phases are indicated.

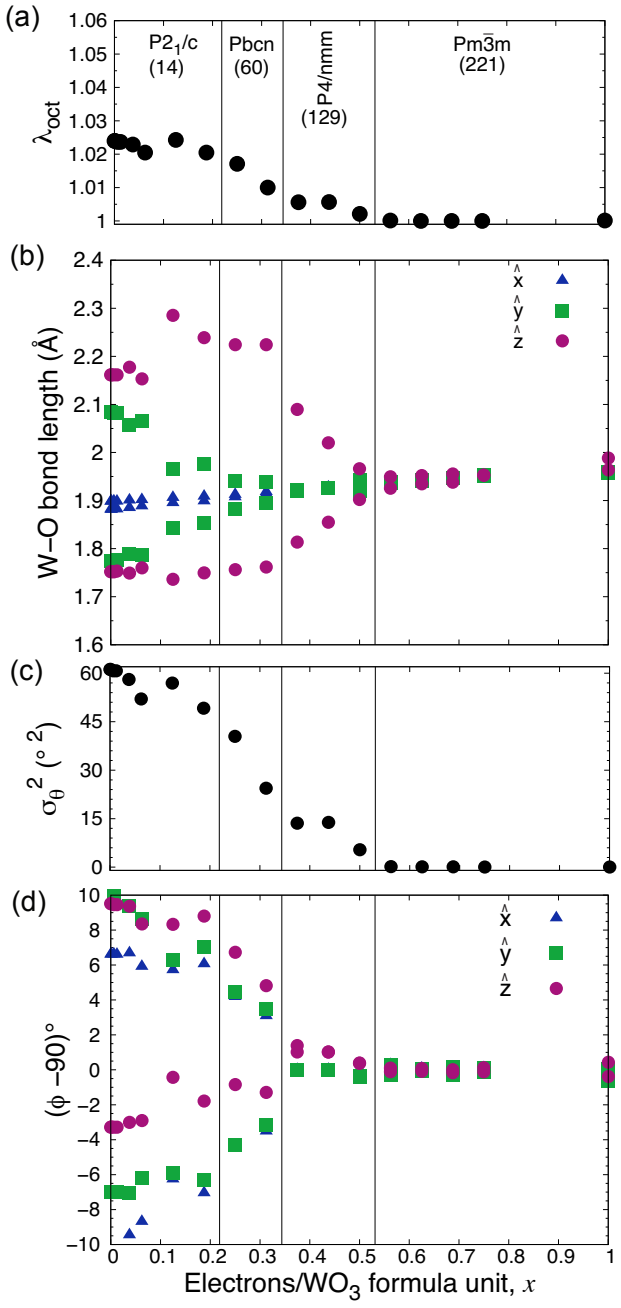

Figure 5.2: Evolution of (a) the quadratic elongation λ_{oct}, (b) variation of W-O bond lengths, (c) bond angle variance σ_θ^2, and (d) tilt angles of octahedra ϕ_1 and ϕ_2 (defined in Fig. 1.1) for each of the crystal directions as a function of electron doping with boundaries between symmetry phases (solid lines), as defined in the text. Space groups and space-group numbers for the various phases are indicated.

a function of doping when no distortions in bond lengths are present. The corresponding evolution of bond lengths illustrating the internal distortion of the octahedra along each direction are shown in Fig. 5.2(b).

The bond angle variance σ_θ^2, shown in Fig. 5.2(c), provides complementary information about the distortion of bond angles in an octahedron, and is defined as the variance from a right angle of the 12 O-W-O angles θ between adjacent O atoms within an octahedron [164],

$$\sigma_\theta^2 = \sum_{i=1}^{12} \frac{1}{11}(\theta_i - 90^\circ)^2 \,. \tag{5.2}$$

Finally, the relative tilt angles ϕ_1 and ϕ_2 between octahedra are reported in Fig. 5.2(d) along the $\hat{x}$, $\hat{y}$, and $\hat{z}$ directions.

The monoclinic structure of space group $P2_1/c$ symmetry persists up to around $x = 0.1875$, where x is defined as the number of electrons added per formula unit. Within this phase, the tilts of the octahedra decrease with increased doping, and the lattice parameters a and b converge [Fig. 5.1(a)]. Six distinct W-O bond lengths are present [Fig. 5.2(b)], due to the displacement of the W ion from the center of the octahedra. The smallest displacements occur along the $\hat{x}$ direction.

Between $x = 0.1875$ and $x = 0.25$ a transition to the orthorhombic $Pbcn$ phase occurs, in which a and b are equal and the angle β approaches a right angle with increased doping. In the orthorhombic symmetry, octahedral rotations (i.e., tilts measured by ϕ) are reduced around the $\hat{x}$, $\hat{y}$, $\hat{z}$ directions, with tilts in the $\hat{x}$ and $\hat{y}$ directions becoming equal. In terms of the W ions, the $\hat{y}$-direction displacements diminish, as evidenced in Fig. 5.2(b).

The $Pbcn$ orthorhombic phase is present up to around $x = 0.3125$; a transition to the tetragonal $P4/nmm$ phase takes place between $x = 0.3125$ and $x = 0.375$. In going from the orthorhombic to tetragonal phases, the relative tilting between octahedra

monotonically decreases [Fig. 5.2(d)]. With increased doping in the tetragonal phase, the lattice parameter c approaches a=b. The $\hat{x}$- and $\hat{y}$-displacements of the W ions also vanish, as shown in Fig. 5.2(b). This is also evident in the decrease of the bond angle variance, shown in Fig. 5.2(c). The remaining displacement of W ions along the $\hat{z}-$direction results in an antiferroelectric-like pattern, with alternating displacements in the $+\hat{z}$ and $-\hat{z}$ directions. With increasing doping, these bond lengths along the $\hat{z}$ direction become close to each other and to those in $\hat{x}\hat{y}$-plane.

The tetragonal $P4/nmm$ phase is stable up to around x= 0.5000; then a transition to the cubic phase ($Pm\bar{3}m$ symmetry) takes place between x= 0.5000 and x= 0.5625. This is evident in Fig. 5.1(a), in which $a = b = c$; and in Fig. 5.2, where the quadratic elongation converges to unity, all W-O bonds converge to a single value, and the bond angle variance vanish. Once the system is in the cubic phase, additional doping merely results in an expansion of the unit-cell volume [Fig. 5.1(a)].

5.2.2 Decomposition into Strain and Electronic Energies

In order to elucidate the mechanisms driving the structural phase transformations, we decompose the total energy change into its strain and electronic components. Our first-principles methodology allows us to add or remove excess fractional electrons, and to include or exclude relaxation of lattice vectors and atomic positions. We adopt the notation $E_y(x)$ to mean the total energy of a structure with an excess (fractional) concentration of electrons x in the conduction band, but with an atomic structure corresponding to a relaxation of the structure obtained with y electrons in the conduction band. That is, the relaxed structure obtained with x electrons in the conduction band has energy $E_x(x)$, and the relaxed ground-state monoclinic phase with no excess doping has energy $E_0(0)$.

First, we add excess electrons to the system to obtain $E_0(x)$, the total energy of the system with extra electrons added, but with the atomic structure kept fixed to that of the monoclinic (undoped) ground state. We can then relax the lattice vectors and atomic positions, leading to a relaxed structure with energy $E_x(x)$. At high enough doping, transformations to phases with higher symmetry will be observed, as discussed in Section 5.2.1. We define $E^{net}(x)$ as the energy difference between the relaxed system with x electrons and the unrelaxed system (i.e., fixed in the monoclinic structure) with x electrons:

$$E^{net}(x) = E_x(x) - E_0(x). \tag{5.3}$$

Our aim is to provide insight into the driving force for energy gain by decomposing this energy.

Once x electrons have been added and the structure is relaxed, we can consider this atomic structure, remove the excess electrons, and calculate the total energy of this structure, denoted $E_x(0)$. The difference between this energy and the energy of the undoped monoclinic structure provides a measure of the energy cost involved in deforming the structure; we will refer to this as a "strain energy," $E^{strain}(x)$:

$$E^{strain}(x) = E_x(0) - E_0(0). \tag{5.4}$$

The fact that transformations to other structures take place at higher doping levels indicates that placing the electrons in the conduction band leads to an energy gain, which we will refer to as $E^{elec}(x)$. We decompose the energy $E^{net}(x)$ as follows:

$$E^{net}(x) = E^{strain}(x) + E^{elec}(x) \tag{5.5}$$

Combining Equations 5.3, 5.4, and 5.5 leads to:

$$E^{elec}(x) = E^{net} - E^{strain} \tag{5.6a}$$

$$= [E_x(x) - E_0(x)] - [E_x(0) - E_0(0)]$$

$$= [E_x(x) - E_x(0)] - [E_0(x) - E_0(0)]\,. \tag{5.6b}$$

The rearrangement of the terms provides insight into the physical origin of this "electronic energy." The first term in square brackets in Equation (5.6b), $[E_x(x) - E_x(0)]$, is a measure of the change in energy associated with changes in the electronic structure upon adding x electrons (to a fixed atomic structure). However, to make this term meaningful we need to define a reference energy for those electrons; this is encapsulated in the second term, $[E_0(x) - E_0(0)]$, which is the energy of adding x electrons to the fixed monoclinic structure.

Figure 5.3 shows the decomposition of the net energy into its strain and electronic components. The strain cost to transform to a higher-symmetry phase is more than compensated by the electronic energy gain.

For the strain energy, further insight is provided by decomposing the strain energy into contributions related to volume expansion and to displacement of atomic positions. The volumetric component can be determined by considering the total energies associated with doping the cubic phase. An analogous strain energy E^{strain}_{volume} is thus calculated as in Eq. (5.7), but taking the undoped cubic phase as the reference state. The remainder in the strain energy, labeled $E^{strain}_{disp}(x)$, is then attributed to the energy associated with

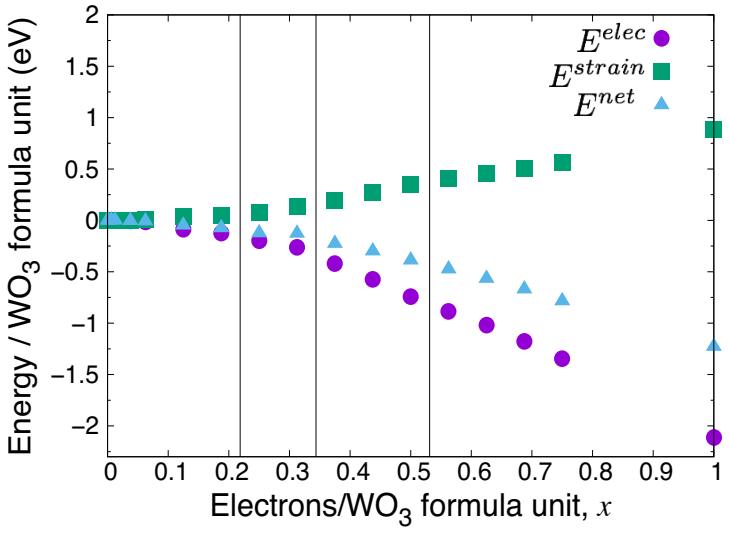

Figure 5.3: Decomposition of energy into strain and electronic components, as described in the text.

non-hydrostatic changes in lattice vectors and with displacement of atomic positions:

$$E^{strain}(x) = E_x(0) - E_0(0) \tag{5.7a}$$
$$= E^{strain}_{volume}(x) + E^{strain}_{disp}(x),$$
$$E^{strain}_{volume}(x) = [E^{cubic}_x(0) - E^{cubic}_0(0)] \tag{5.7b}$$
$$E^{strain}_{disp}(x) = E^{strain}(x) - E^{strain}_{volume}(x) \tag{5.7c}$$
$$= [E_x(0) - E_0(0)] - [E^{cubic}_x(0) - E^{cubic}_0(0)]$$

Figure 5.4 shows this decomposition of the strain energy. Below the concentration for the onset of the cubic phase, the terms due to volumetric expansion and due to distortions contribute roughly equally to the overall strain. Once the cubic phase is reached, strain energy associated with distortions becomes constant and any additional strain energy is strictly due to volume expansion with additional electron doping.

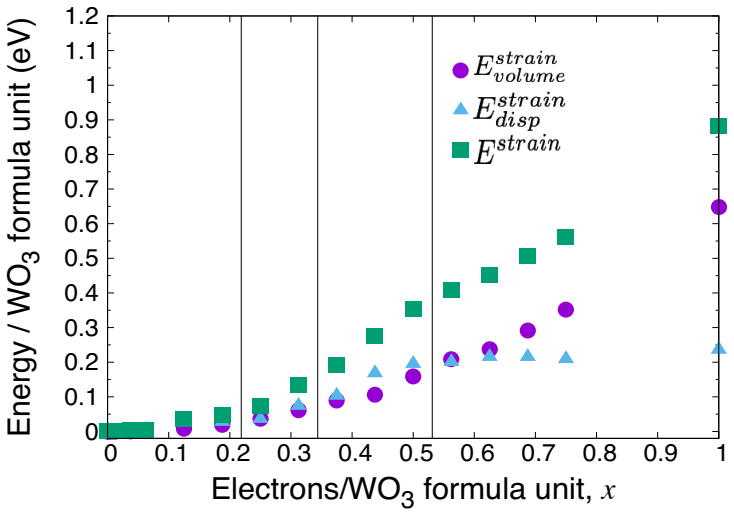

Figure 5.4: Decomposition of strain energy into volumetric and internal displacement components.

5.3 Discussion

5.3.1 Driving Force for Phase Transformation

As shown in previous sections, the transfer of the electron from the dopant to host lattice leads to the structural transformations earlier characterized. We now demonstrate that the gain in electronic energy, which drives the phase transformation (Fig. 5.3), is primarily due to a lowering of the conduction band on an absolute energy scale. Table 1.2 shows band gaps for the various phases of WO_3. The higher the symmetry of the phase, the smaller the band gap. This trend can be attributed to the correlation between the band width of the conduction band (composed primarily of W d states) and the degree of octahedral tilting and off-centering of W. Overlap between d orbitals is maximized in the highest-symmetry (cubic) structure. Strong overlap leads to large band width and hence small band gap. Lower-symmetry phases exhibit distortions of the octahedra that result in narrowed band widths and thus larger band gaps. We explicitly demonstrate and quantify how distortions play a role in the phase transformations for electronically

doped WO_3.

The overall change in the band gap as a function of doping, going from $x = 0$ to $x = 1$ is $\Delta E_g = -1.45$ eV. To demonstrate that this change in gap is driven primarily by the structural distortions and only partially by volume expansion, we calculate the change in gap due to the individual contributions (without electron doping). We use the band-gap change observed for the expanded cubic phase as an indicator of what fraction of the band-gap change can be attributed to volume expansion. For the volume change corresponding to $x = 1$ [Fig. 5.1(c)], this yields a change in the band gap of $\Delta E_g = -0.26$ eV. To determine how the band gap changes with internal structural distortions, we introduce either just the tilting of the octahedra, or only the offset of the W ions into the cubic structure at the (smaller) monoclinic volume. With only octahedral tilting, $\Delta E_g = -0.16$ eV; with only the offset of W ions, $\Delta E_g = -1.29$ eV; including both octahedral tilting and offset of W atoms of the monoclinic phase into the cubic structure, ΔE_g=−0.92 eV. We note that the band-gap changes due to octahedral tilting, W offset, and volume change are not simply additive, since the various types of distortions interact. Still, these results indicate that while volume expansion does lead to a reduction in the band gap, it is the structural distortions and in particular the offset of the W ions that are primarily responsible for the decrease in the band gap.

While the change in band gap is suggestive of why higher-symmetry phases are energetically favorable with doping, we still need to demonstrate that the conduction band itself is lowered in energy. For that purpose we calculate the alignment of band structures between the cubic and monoclinic phases. In principle this requires a calculation for an interface between the two phases [165, 4]. Such a calculation should be performed on a superlattice containing layers of each phase, which allows determining the alignment of the average electrostatic potentials within each phase. The position of the CBM with respect to the average electrostatic potential $\widetilde{V}$ is obtained from separate

calculations of the bulk phases. Combining the superlattice with the bulk results yields the conduction-band offset.

Unfortunately, constructing a pseudomorphic interface between the cubic and monoclinic structures is challenging. The distortions of the monoclinic phase lead to disparate bond lengths at the cubic-monoclinic interface that result in dipoles, which makes extracting a meaningful average electrostatic potential difficult. We therefore make the plausible assumption that the change in average electrostatic potential between monoclinic and cubic depends primarily on volume, and contributions related to additional distortions of the cell and to changes in internal coordinates can be neglected. Based on this assumption, the average electrostatic potentials $\widetilde{V}$ in the cubic phase is equal to the average electrostatic potential in the monoclinic phase if the cubic phase is strained (expanded) to be at the same volume as the monoclinic phase. To obtain the alignment between the strained and unstrained cubic phase, we perform a calculation for a superlattice in which one layer consists of cubic material at its equilibrium volume, and the other layer is strained to reflect the volume change between cubic and monoclinic phases. This calculation yields the result that the average electrostatic potential in cubic WO_3 at its equilibrium volume is 0.16 eV lower than in cubic WO_3 that is expanded to match the volume of the monoclinic structure.

Figure 5.5 shows the resulting alignment of the electrostatic potential, as well as the position of the CBM and the VBM referenced to the average electrostatic potential in the monoclinic and cubic phases. The resulting conduction-band offset between the cubic and monoclinic phases is 1.05 eV. The corresponding valence-band offset is much smaller, 0.02 eV. The insensitivity of the valence-band offset to the difference in structure between the cubic to monoclinic phases can be attributed to the fact that the O $2p$ states at the VBM are composed of non-bonding oxygen p-states [9], which are relatively unaffected by distortions.

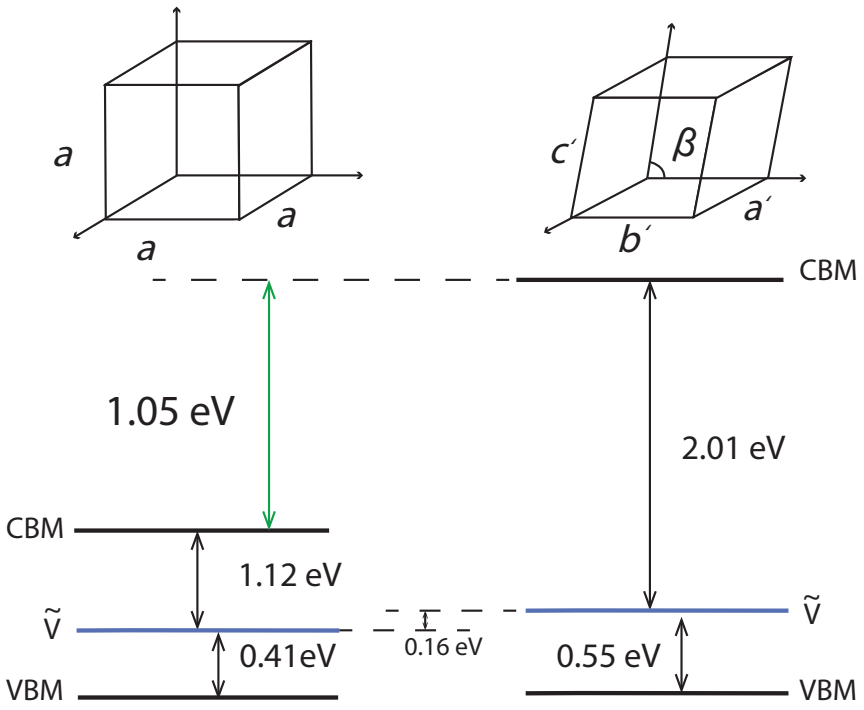

Figure 5.5: Band alignment between the cubic and monoclinic phases of WO_3. The positions of the VBM and CBM are shown with respect to the average electrostatic potential $\widetilde{V}$ in each phase.

We note that the band-gap difference between the monoclinic and cubic phases reported in Fig. 5.5 is different from the value $\Delta E_g = -1.45$ eV reported above for the difference between $x = 0$ to $x = 1$. The difference is due to the fact that the band gap for the cubic phase in Fig. 5.5 is for the undoped cubic phase at its equilibrium volume (as reported in Table 1.2), while the band-gap for $x = 1$ reflects the presence of a large concentration of electrons, leading to a volume expansion as well as additional conduction-band lowering due to band-gap renormalization. The purpose of Fig. 5.5 was to demonstrate that the CBM of the cubic phase is significantly lower than that of the monoclinic phase, providing a driving force for the phase transition to the higher-symmetry structure when electrons are placed in the conduction band.

5.3.2 Comparison with Previous Work and with Experiment

Walkingshaw *et al.* [162] also investigated how electronic doping of WO_3 leads to phase transformations. They focused on an examination of structural distortions rather than energetics. While the trends in modes of distortion upon electron doping are broadly similar to the ones found in our work, significant quantitative differences are evident for lattice parameters and atomic positions. The phase boundaries found by Walkingshaw *et al.* [162] also occur at much higher doping levels than in our study; for instance, the boundary between the tetragonal and cubic phase occurs at $x = 0.68$ in Ref. [162] while we find it at around $x = 0.53125$. We attribute these differences mainly to their use of the LDA. The electronic structure obtained with the HSE functional used in our work is known to be much more accurate than that obtained with LDA [166, 143]. Lattice parameters, and hence volume, are significantly underestimated in LDA. A smaller volume corresponds to greater octahedral tilting, and thus lower-symmetry phases will appear stable up to higher electron concentrations in LDA calculations.

Computations with electron doping were also performed by Wang *et al.* [159], who report phase boundaries at smaller electron concentrations. Again, the difference can be attributed to the use of a less accurate functional. Using GGA+U, Wang *et al.* [159] found lattice parameters for the monoclinic phase ($a = 7.68, b = 7.70, c = 7.76$ Å) that are significantly larger than those found experimentally or found with HSE (see Table 1.2). By similar logic as in the comparison with Walkingshaw *et al.* [162] a larger volume corresponds to smaller octahedral distortions, and this will tend to stabilize higher-symmetry phases at smaller electron concentrations. Given the importance of electronic effects in driving the phase transitions (see Sec. 5.3.1), our results can be considered more reliable.

We now turn to a comparison with experiment. Zhong *et al.* [16] investigated charging with Li, and reported that the phase boundaries observed in the case of charging differed significantly from those found in the case of discharging. Ranges of overlap were interpreted as regions of two-phase coexistence, but kinetic effects may also be playing a role. A comparison with our results, which are based purely on equilibrium energies, can therefore be only qualitative. The experimentally observed ranges of stability for different phases in the case of Li charging were $x \leq 0.015$ for monoclinic, $0.078 \leq x \leq 0.12$ for tetragonal, and $x \geq 0.21$ for cubic; in the case of discharging the ranges were $x \leq 0.01$ for monoclinic, $0.08 \leq x \leq 0.13$ for tetragonal, and $x \geq 0.36$ for cubic, with the measurements going up to x=0.50 [16]. Other experiments were performed with Na [15, 163]: Brown and Banks [15] observed the cubic phase for electron concentrations of $x \geq 0.26$, whereas Egdell and Hill [163] found that for $0.26 \leq x \leq 0.40$ other phases were present along with the cubic phase.

The difference between experimentally and computationally determined phase boundaries may be attributed to several factors. First, our calculations describe the behavior of bulk single crystalline material. This is not necessarily the case for experimental

samples, which may be polycrystalline, contain impurities other than the intercalated species, or be subject to stress due to thin-film preparation [16, 146, 163]. We note that even studies that use the same dopant species (e.g., the Na-doping experiments in Refs. [15] and [163]) report significant differences in the observed phase boundaries. Last but not least, our study was conducted for pure electron doping, and did not consider the influence of dopants explicitly.

5.4 Conclusions

We have performed a comprehensive first-principles treatment of the structural transformation of tungsten trioxide (WO_3) as a function of electron doping using hybrid functionals. A decomposition of energies into strain and electronic energies sheds light on the physical mechanisms underlying the transformations. We demonstrated that the structural transformation to higher-symmetry phases is driven predominantly by the lowering of the conduction band, which occurs as structural distortions become smaller.

Up to this point, we have established that both oxygen vacancies and alkali dopants behave as shallow donors. Furthermore, these shallow donors have profound impacts on the atomic and electronic structure. For the remainder of this dissertation, we explore the influence of these excess carriers on the transport (Chapter 6) and optical properties (Chapter 7) as a function of doping.

Chapter 6

First-principles Study of Transport in WO_3

From Chapters 4 and 5, we have established that shallow donors are the typical dopants in applications based on WO_3. For the remaining chapters, we explore how the excess carriers from these donors interact with the host lattice. In this chapter, we discuss transport properties with electron-phonon coupling. The contents of this chapter are in preparation for submission [W. Wang, Y. Kang, H. Peelaers, K. Krishnaswamy, C.G. Van de Walle. "First-principles study of transport in WO_3"].

6.1 Motivation

As mentioned in Chapter 1, WO_3 is utilized as an electrochromic material [10, 13, 167], as a functional material in gas sensing [19], photocatalysis [21, 22], an electrode in lithium-ion batteries [23], and as an electron transport layer in high-efficiency solar cells [24]. In all these applications, carrier transport plays a pivotal role, and a full understanding of transport mechanisms is a prerequisite for device performance. Few

studies have been devoted to understanding transport in WO_3; mainly these have been experimental reports of mobilities or electrical resistivities with fits to models. For instance, Berak *et al.*[122] reported mobilities in single crystalline monoclinic WO_3 on the order a tens of $cm^2/V{\cdot}s$ near room temperature, and Berggren studied the influence of temperature on resistivities of lithiated samples [123]. Here, we use a fully first-principles approach to shed light on the microscopic origins of mobility.

WO_3 has various polymorphs (see Fig. 1.1 and Table 1.2), which are distinguished by the degree of tilting, rotation, and distortion of WO_6 octahedra. In this work we focus on the cubic phase [Fig. 1.1(d)], which is free of structural distortions. We are motivated to study the cubic phase because of its potential use in complex oxide heterostructures in combination with other cubic perovskites; complex oxide interfaces can lead to large two-dimensional electron gas densities [4, 87]. Controlled growth along the [100] direction of cubic WO_3 on $SrTiO_3$ (STO) has been demonstrated using molecular beam epitaxy [168] and dc magnetron sputtering [169]. The cubic phase may also be stabilized through doping with donor species such as Li, Na or K [16, 157], a phenomenon that has been shown to be driven by the presence of excess electrons [162, 156]. Exploring transport in cubic WO_3 is therefore relevant for bulk as well as epitaxial films.

We use first-principles calculations based on DFT to obtain electronic and vibrational spectra, and calculate mobilities using Boltzmann transport theory within the relaxation time approximation [77]. We consider electron-phonon interactions as the dominant scattering mechanism at room temperature [77]. As WO_3 is a polar material, we discuss the role of LO-phonon scattering. Due to the heavy mass of the tungsten atom, spin-orbit coupling (SOC) is included in our calculations. Accurate sampling in $\mathbf{k}$ space is important, and for that purpose we use Wannier interpolation [170, 98] to account for the $\mathbf{k}$-dependent scattering rate [88, 91].

Our results show that the room-temperature mobility is much higher than in other

complex oxides: at 10^{20} cm^{-3} doping, and in the absence of free-carrier screening (which will make the mobility even higher), the mobility is as high as 238 cm^2/V·s, which is two orders of magnitude larger than in the prototype perovskite complex oxide, STO [171, 4, 94]. A detailed comparison of the various features in the electronic and vibronic structure will allow us to elucidate the factors that contribute to this difference in mobilities.

After a presentation of our methodology in Section 6.2, we first present our results on the bulk electronic and vibronic properties of cubic WO_3 in Sections 6.3.1 and 6.3.2. In Section 6.3.3 we present an in-depth investigation of scattering rates and (unscreened) mobilities as a function of doping. Finally, in Section 6.3.4 we address why the mobility in cubic WO_3 is significantly higher than in cubic STO at room temperature.

6.2 Methodology

Our calculations use the QUANTUM ESPRESSO code [76] with norm-conserving pseudopotentials [172] and the exchange-correlation functional of Perdew, Burke, and Ernzerhof (PBE) [54]. For W, the $5p6s5d$ states are treated as valence states, and for O, the $2s2p$ states. In our STO calculations, the $4s4p5s$ states are treated as valence states for Sr and $3s3p3d4s$ for Ti. In order to assess the accuracy of our band structures we also use the hybrid functional of Heyd, Scuseria, and Ernzerhof (HSE) [52, 53]. In order to include SOC, we perform self-consistent calculations based on a fully-relativistic pseudopotential. We use a plane-wave cutoff of 125 Ry and a $6 \times 6 \times 6$ **k**-point grid for integrations over the Brillouin zone.

The vibrational spectra are calculated using density functional perturbation theory (DFPT) [82]. Using a hybrid functional for all aspects of the calculations is currently not feasible, since DFPT calculations are not implemented with hybrid functionals; we therefore use the PBE functional. Based on the lattice dynamical properties we obtain

the electron-phonon matrix elements, which describe the strength of phonon-mediated transitions between different electronic states. These are calculated on a $6 \times 6 \times 6$ **k**- and **q**-point grid, and then Wannier-interpolated at denser **k**- and **q**-point grids using the EPW code [88]. To check the validity of using interpolation with Wannier functions [including using Eq. (3.12) for the long-range component], we compared the phonon spectra and electron-phonon matrix elements with explicit DFPT calculations along the high-symmetry paths of the Brillouin zone and found excellent agreement. For calculating the scattering rates and mobility we use $50 \times 50 \times 50$ **k**- and **q**-point grids.

The methodology for calculating the scattering rate and mobilities is described in Section 3.4.2. Scattering off polar longitudinal optical (LO) phonons tends to be the dominant scattering mechanism at room temperature in polar materials [94, 77, 97, 96], but we note that our calculated scattering rate [Eq. (3.31)] includes contributions from all phonons. Our methodology for treating electron-phonon matrix elements is described in Section 3.2.2.

6.3 Results

6.3.1 Bulk Electronic and Vibronic properties

In Chapter 1 we showed bulk electronic properties for calculations without SOC. Here, we present the bulk properties with SOC included. Note that the bulk properties reported are different from the values presented in Table 1.2 as we use a different functional. The calculated lattice parameter used in the calculations here is $a = 3.80$ Å for both with and without SOC, within 0.5% of reported experimental values ($a = 3.77$ Å [41] and $a = 3.78$ Å [15]). The calculated band structure for the conduction bands is shown in Fig. 6.1(a). The comparison with the band structure of STO [Fig. 6.1(b)] will

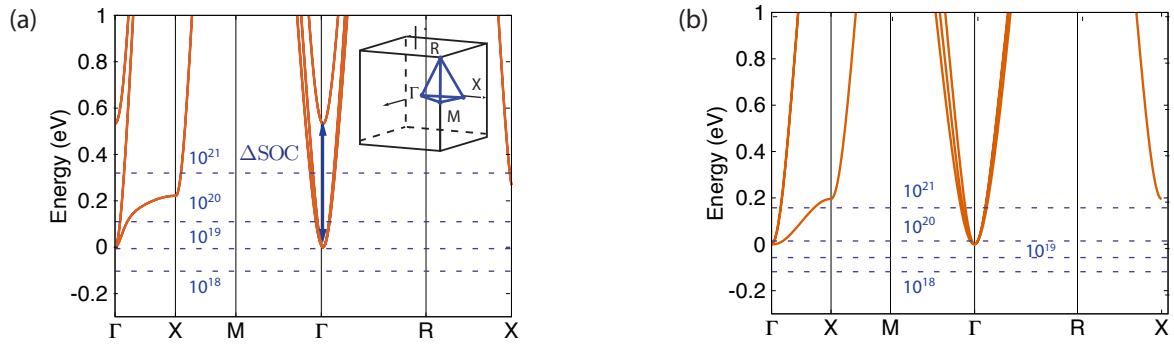

Figure 6.1: Electronic bandstructure of (a) cubic WO_3 and (b) cubic strontium titanate (STO). The Brillouin zone, identifying high-symmetry points, is depicted in the inset. Only the t_{2g} conduction-band states are shown. Dashed lines indicate the Fermi level for various electron concentrations (in cm^{-3}). The band splitting due to spin-orbit coupling in WO_3 is $\Delta SOC = 0.55$ eV.

be discussed in Sec. 6.3.4. As mentioned in Chapter 1, the conduction bands are composed predominantly of W $5d$ states. In cubic perovskites, the crystal field due to the octahedral oxygen cage encasing the transition-metal atom causes the d states to split into the lower-lying triply-degenerate t_{2g} and higher-lying doubly-degenerate e_g states. The inclusion of SOC splits the t_{2g} degeneracy and lifts one of the bands by 0.55 eV relative to the conduction-band minimum (CBM). The fundamental gap is $E_g = 0.70$ eV for non-relativistic calculations of WO_3 (consistent with previous PBE values [126]) and $E_g = 0.51$ eV with SOC included.

While PBE is known to underestimate the band gap, only the conduction-band structure near the Fermi level is relevant for determining transport properties of electrons. We do want to establish that the band dispersions obtained in PBE are reliable. For that purpose we compare with a band structure obtained with the HSE hybrid functional, which has been shown to provide a reliable description of the electronic structure of solids [166], and was previously used to obtain band structures for WO_3 (see Fig. 1.2 and Chapter 4). In Table 6.1, we compare effective masses calculated based on the PBE band structure with values obtained using HSE. Effective masses were calculated by

Table 6.1: Effective masses of the t_{2g} states for cubic WO_3 along high-symmetry directions, in units of the free electron mass m_0. Effective masses m_i^* are indexed by band i, starting from the lowest-lying band. Values calculated with PBE and HSE [116] functionals are shown.

	$\Gamma \to X$		$\Gamma \to M$		$\Gamma \to R$	
	PBE	HSE	PBE	HSE	PBE	HSE
m_1^*	0.17	0.17	0.24	0.22	0.21	0.18
m_2^*	0.15	0.18	0.15	0.17	0.15	0.14
m_3^*	0.21	0.20	0.25	0.26	0.20	0.17

fitting the band structure to a hyperbolic model as derived from $\mathbf{k} \cdot \mathbf{p}$ theory [173]:

$$\hbar^2 k^2 / 2m_\Gamma^* = \epsilon_\mathbf{k}(1 + \alpha \epsilon_\mathbf{k}), \tag{6.1}$$

where m_Γ^* is the electron effective mass at Γ, $\epsilon_\mathbf{k}$ is the band energy and momentum, and α is the non-parabolicity parameter. The comparison indicates that PBE provides a reliable band structure. The SOC-induced splitting results in the originally heavy band along $\Gamma \to X$ to have an effective mass comparable to the other t_{2g} bands.

The cubic phase contains four atoms in the unit cell, leading to 12 phonon modes, including two longitudinal optical (LO) phonons and four transverse optical (TO) phonon modes. Our calculated frequencies at Γ are shown in Table 6.2. The polar optical modes are associated with one LO and two degenerate TO modes. The imaginary TO mode indicates that the cubic structure is in fact dynamically unstable. Our calculated frequencies at Γ compare reasonably with previous calculations [33]. We note our calculations include the full $\mathbf{q}$ dependence of the phonon spectrum.

The calculated phonon frequencies at Γ for STO are also listed in Table 6.2. In contrast to WO_3, STO has 15 phonon modes, including three LO modes and six TO modes. Our calculated frequencies compare well with previous computational studies [94] and with experiment [174, 175], despite cubic STO also being dynamically unstable

Table 6.2: Calculated longitudinal (LO) and transverse (TO) phonon frequencies in cm^{-1} (meV in parentheses) for WO_3 and STO.

ω_{LO}		ω_{TO}	
WO_3	STO	WO_3	STO
892 (111)	796 (99)	570 (70)	560 (69)
387 (48)	448 (55)	292i (36i)	169 (21)
	161 (21)		25 (3)

in first-principles calculations.

The calculation of electron-phonon matrix elements [Eq. (3.12)] requires the high-frequency dielectric constant. Our calculations yield ε^{∞}=10.14. As a check, we performed calculations for the room-temperature monoclinic phase; averaging over the principal Cartesian directions we find $\varepsilon^{\infty} = 5.75$. This compares well with the experimentally measured value of ε^{∞}=5 [155]. In STO, we calculate $\varepsilon^{\infty} = 6.41$ (experiment: $\varepsilon^{\infty} = 5.59$, Ref. [176]).

6.3.2 Electron-phonon Matrix Elements

We first present our results for electron-phonon matrix elements. While all phonon modes are included in our calculations, we focus on the polar LO modes as they significantly impact mobility at room temperature [77].

In Fig. 6.2 we plot the electron-phonon matrix elements for the LO modes along the high-symmetry paths of the Brillouin zone. As expected from Eq. (3.12), we observe a $1/q$ dependence in the matrix elements for small q. Deviations from the $1/q$ behavior away from Γ in Fig. 6.2 arise from the short-range contribution $g^{S}_{mn,\nu}$. The plot includes all scattering processes, but for interband transitions the magnitude of the matrix element in Eq. (3.12) is suppressed; transitions between states with different band indices are weaker due to the overlap factor $\langle \psi_{m,\mathbf{k+q}} \left| e^{i(\mathbf{q+G})\cdot\mathbf{r}} \right| \psi_{n,\mathbf{k}} \rangle$, which is typically less than

unity.

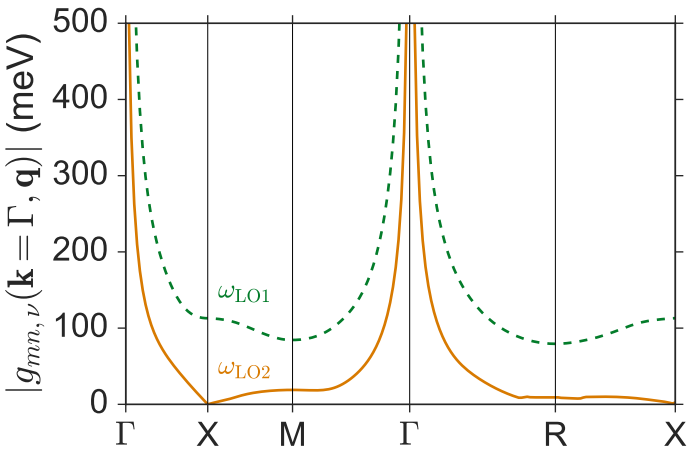

Figure 6.2: Magnitude of electron-phonon matrix elements $|g_{mn,\nu}(\mathbf{k},\mathbf{q})|$ plotted along high-symmetry $\mathbf{q}$ points for $\mathbf{k}$=Γ in WO_3. Values are shown for the highest (dashed green) and second-highest LO polar (solid orange) modes and for transitions amongst t_{2g} states. $|g_{mn,\nu}|$ is averaged over all degenerate electronic and vibronic states.

6.3.3 Scattering Rate and Mobility

Using the calculated electron-phonon matrix elements [Eq. (3.11)], we evaluate the scattering rates of the conduction electrons [Eq. (3.31)]. In Fig. 6.3 we plot the scattering rates referenced to the CBM along with the position of the Fermi level.

Only states with energies close to the Fermi level are involved in scattering. As shown in the equation for conductivity $\sigma_{\alpha\beta}$ [Eq. (3.30)], this is due to the factor $\left(-\partial f_{n\mathbf{k}}/\partial\epsilon_{n\mathbf{k}}\right)$, which is nonzero only in a range of a few kT (around 0.2 eV for room-temperature) around the Fermi level and falls rapidly away from the Fermi level.

For 10^{18} and 10^{19} cm^{-3} doping, we see in Fig. 6.3 that the main difference in relevant scattering events within the energy window of interest is due to the position of the Fermi level. As the Fermi level becomes degenerate with the conduction band, there are

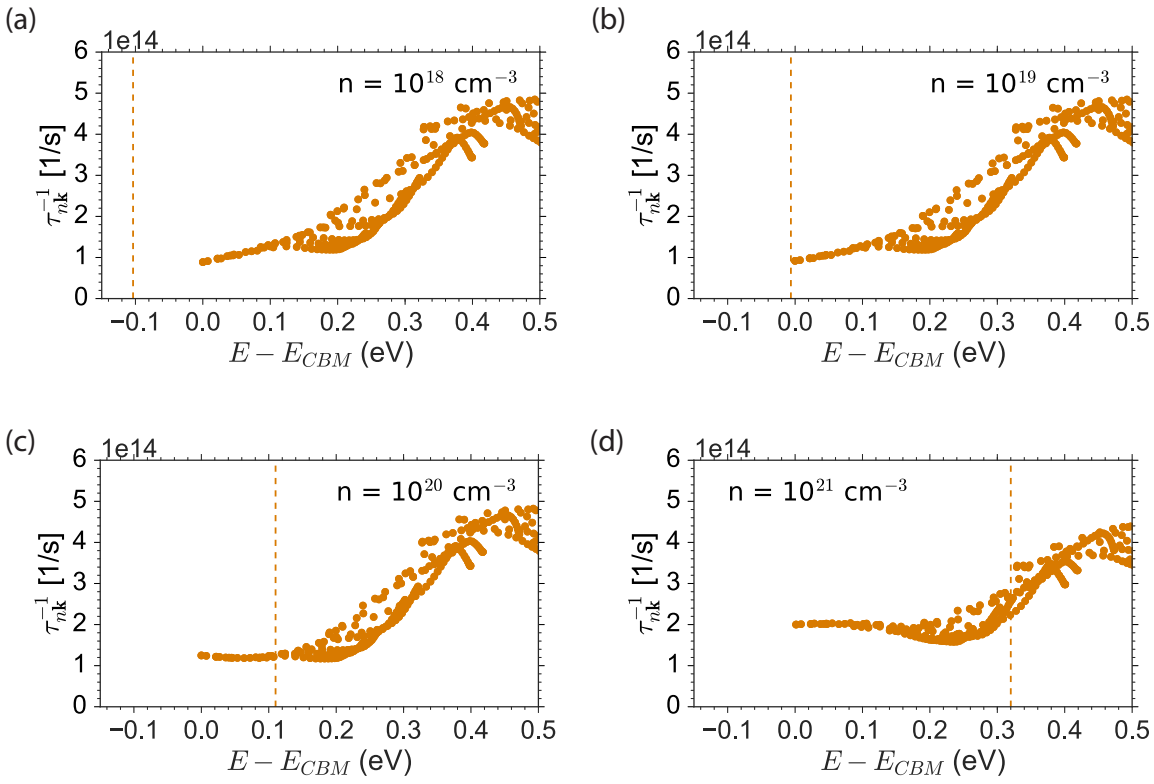

Figure 6.3: The electron-phonon scattering rate in cubic WO_3 for (a) 10^{18}, (b) 10^{19}, (c) 10^{20}, and (d) 10^{21} cm^{-3} doping. Electron energies are referenced to the CBM. The Fermi level is indicated with a dotted line.

now electronic states above and below the Fermi level that can contribute to scattering. Thus, for 10^{20} and 10^{21} cm^{-3} doping, scattering events exist both above and below the Fermi level. The scattering rate increases for 10^{21} compared to 10^{20}, since more states become available for scattering. This leads to a decrease in the mobility.

Table 6.3 presents the (unscreened) mobilities for WO_3 as a function of doping. Mobilities for WO_3 range between 66 and 238 cm^2/V·s for doping levels ranging between 10^{18} and 10^{21} cm^{-3}. The trends in mobility as function of carrier concentration can be understood by considering both the scattering rates (Fig. 6.3) and the band velocities (Fig. 6.4) [see Eq. (3.30)]. When the carrier concentration is increased from 10^{18} to 10^{19} cm^{-3}, conduction-band states at higher energy become occupied, which leads to

higher band velocities (Fig. 6.4). These higher velocities more than compensate for the increase in scattering, thus leading to higher mobility. When the carrier concentration is increased further to 10^{20} cm^{-3}, the increase in scattering rate counteracts the increase in band velocities, so that the mobility stays roughly constant. Increasing the carrier concentration to 10^{21} cm^{-3} leads to a decrease in the mobility, as the increase in band velocities is overshadowed by the increase in scattering.

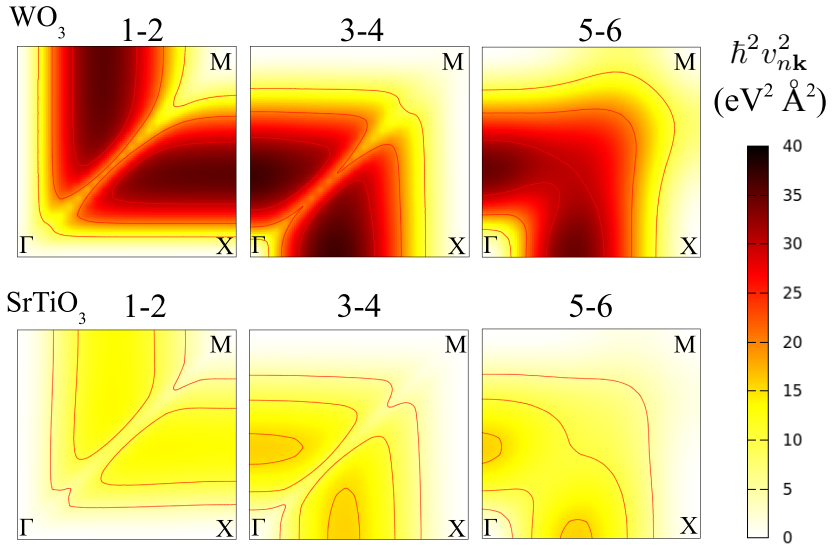

Figure 6.4: Band velocity $v_{n\mathbf{k}}^2$ values plotted in the $k_z = 0$ plane in the Brillouin zone, comparing WO_3 and STO. High-symmetry points in the Brillouin zone are indicated. Each of the t_{2g} states is shown, with the number above each panel indicating the corresponding band index, counting from the lowest conduction band. Band indices correspond to spin channels.

6.3.4 Comparison with STO

We now compare the results for WO_3 with STO, a prototype perovskite that also has conduction bands derived from d states. In our calculations for STO we neglect the effects of SOC, since it is very small (ΔSOC = 0.028 eV, Refs. [177] and [178]). Our calculated mobilities for STO are around 10 cm^2/V·s for doping levels up to $n =$

Table 6.3: Calculated mobilities in $cm^2/V{\cdot}s$ for WO_3 and STO as a function of electron doping.

n (cm^{-3})	WO_3	STO
10^{18}	66	9.0
10^{19}	232	9.6
10^{20}	238	7.3
10^{21}	101	1.9

$10^{20}\,cm^{-3}$, much lower than the values for WO_3 (see Table 6.3). This difference can be attributed to a difference in scattering rates, as well as to a difference in effective masses, which are related to the band velocities in Eq. (3.30).

Our calculated scattering rate in STO is around $\tau_{n\mathbf{k}}^{-1} \approx 10^{16}\ s^{-1}$, more than an order of magnitude larger than in WO_3 (see Fig. 6.3). Comparing $\omega_{LO,1}$ and $\omega_{LO,2}$ between WO_3 and STO, we find that the electron-phonon coupling strengths are comparable in magnitude. Thus, this enhanced scattering rate is due to other factors; we have identified three contributions.

First, the number and frequencies of LO modes. In WO_3 the number of polar LO modes is two, compared to three in STO, and thus one fewer scattering channel enters in Eq. (3.31). This is a result of the missing A-site atom in WO_3. The frequencies of the three LO modes in STO are listed in Table 6.2. The additional LO mode in STO actually has the lowest frequency, $\omega_{LO,1} = 161\ cm^{-1}$ (21 meV), which means the phonon occupation factor will be higher at rom temperature, and this mode can contribute strongly to scattering. In fact, many of the phonon frequencies in STO are lower than in WO_3 (see Table 6.2). Lower frequencies mean higher phonon occupation factors [see Eq. 3.31] and larger scattering rates.

Second, in WO_3, one of the t_{2g} states is lifted due to SOC, whereas in STO it remains degenerate with the other t_{2g} states (at Γ). This leads to a reduction of possible scattering events in WO_3, leading to smaller scattering rates.

Third, the conduction-band states in STO are comprised of Ti $3d$ states, as opposed to W $5d$ states in WO_3. W $5d$ orbitals are less localized than $3d$ orbitals of Ti, leading to larger bandwidths, more dispersion, and larger band velocities in WO_3. As Eq. (3.30) depends quadratically on band velocities, this has a substantial effect on the electrical conductivity. The effect of $3d$ versus $5d$ band character can be observed in the effective masses. The effective masses (in units of the free electron mass, and calculated with inclusion of spin-orbit coupling, Ref. [177]) for the three lowest-lying conduction bands along the $\Gamma \rightarrow$ X direction in STO are 0.99, 0.39, and 0.55; along the $\Gamma \rightarrow$ M direction the values are are 0.74, 0.46, and 0.56. As can be seen from Table 6.1, these effective masses are a factor of two or more larger than those in WO_3.

These effective masses probe the band structure only in the vicinity of the CBM; band dispersion at higher energies also plays a role in mobilities, particularly at higher doping levels. We therefore explicitly inspect band velocities $v^2_{n\mathbf{k}}$ throughout the Brillouin zone, as plotted in Fig. 6.4. The conduction-band velocities in WO_3 are indeed much larger than those in STO, for each of the t_{2g} bands.

This combination of factors leads to a larger scattering rate and lower mobility in STO.

6.4 Conclusions

In conclusion, we have used first-principles calculations to investigate the transport properties in WO_3. We consider the full $\mathbf{k}$ dependence of the scattering rates to compute the conductivity tensor based on Boltzmann transport theory. Mobilities were calculated as a function of doping level for carrier concentrations ranging from 10^{18} to 10^{21} cm^{-3}. We find (unscreened) mobilities as high as 238 cm^2/V·s at 10^{20} cm^{-3} doping. Finally, we show that the enhanced mobilities in WO_3 relative to the widely-studied STO can

be attributed to one fewer polar LO mode, larger phonon frequencies, a larger splitting of the t_{2g} states due to SOC, and larger band velocities for WO_3.

Chapter 7

Influence of Structural Disorder on Optical Absorption

In the following chapter, we investigate the optical response of excess carriers in the system. We find that the first-order linear response of such carriers contributes significantly to the optical absorption. The content of this Chapter has been submitted for publication to the journal *MRS Communications.* [W. Wang, H. Peelaers, J.-X. Shen, and C.G. Van de Walle. "Carrier-Induced Absorption as a Mechanism for Electrochromism in WO_3."]

Electrochromic materials are a subset of what are known as chromogenic materials. Chromogenic materials are those that have reversible changes in optical transmittance upon application of some external stimuli (e.g., temperature for thermochromism or light for photochromism). The external stimulus for electrochromic materials is an applied electric field, which drives dopants such as Li into the active layer of the device.

In our study of defects and dopants in Chapter 4, we found evidence that suggested the transitions of excess carriers to higher empty states as an alternate mechanism for electrochromic behavior. In this chapter, we perform explicit first-principles calculations

to evaluate this hypothesis.

7.1 Motivation

The introduction of dopants to the system (typically monovalent dopants such as H, Li, or Na [179, 180]) leads to a strong decrease in transmittance at infrared and visible wavelengths, and typically blue coloration. Surprisingly, the mechanism of electrochromism is still poorly understood. A number of mechanisms have been proposed to explain electrochromism in WO_3, including absorption by deep defect levels [130] or by small polarons [147, 18]. Here we propose an alternative explanation, which is consistent with all the experimental observations: the absorption of light in momentum-conserving (i.e., direct) transitions of electrons filling conduction-band states. Indeed, the intercalation of dopants leads to the introduction of carriers in the conduction band [149, 150], as evidenced by the observation of higher electrical conductivities [181, 182]. It was noted [148, 149, 180] that these carriers can lead to an increase in IR reflectivity; however, to our knowledge the impact of carrier absorption on absorption at visible wavelengths has not been explored to date. Carriers introduced by doping can absorb photons and be excited to higher-lying conduction-band states. In this chapter, we demonstrate that carrier-induced absorption significantly contributes to the optical absorption not only at infrared but also at visible wavelengths. We analyze how this absorption depends on doping level, and demonstrate the correlation between the absorption coefficient and the structure of the material.

Our proposal for the role of carrier-induced absorption is also consistent with the observation that oxygen vacancies lead to electrochromic behavior [122]. In Chapter 4, we established that oxygen vacancies act as shallow donors and introduce electrons in the conduction band (as opposed to forming deep levels or giving rise to polarons). By

invoking carrier-induced absorption, the enhancement of electrochromism due to oxygen deficiency can then be explained at the same level as the effects caused by dopant intercalation of alkali metals.

First-principles investigations on the optical properties of WO_3 have focused on undoped phases [183]. Other experimental and computational studies invoked the phenomenological Drude model to analyze optical spectra of intercalated WO_3 [148, 149, 150, 180]. The Drude model involves fitting parameters to experiment and is not suitable for describing optical behavior in the visible. Our objective is thus to use first-principles calculations to quantify carrier-induced absorption across the IR and visible spectrum, and build an understanding of the dependence on doping level and structural distortions.

We focus on direct optical transitions in which the crystal momentum is conserved and the initial states are occupied with doping-induced carriers, which we shall refer to as carrier-induced absorption. Indirect transitions, usually assisted by phonons, can also cause absorption, but are typically smaller in magnitude than direct transitions; indirect transitions tend to dominate in materials in which direct transitions are suppressed due to the lack of final states [184]. We will see that the conduction-band structure of WO_3 offers many opportunities for final states of such direct transitions, and these will dominate the absorption.

We apply our formalism to the cubic, monoclinic, and disordered phases of WO_3 in order to understand the influence of structural distortions. Our results demonstrate that carrier-induced optical transitions lead to significant absorption in the infrared in the crystalline phases of WO_3. Structural distortions lead to enhanced absorption at visible wavelengths; such distortions occur in the monoclinic phase, and are particularly large in the disordered phase. We relate the changes in the optical transition matrix elements to changes in bonding caused by structural distortions. Our results allow us to conclude that carrier-induced absorption plays a significant role in the optical absorption and

coloration of WO_3, and we quantify these effects.

7.2 Calculation Methodology

7.2.1 Computational Details

We calculate the optical spectra according to the equations in Section 3.5.1. The dipole transition (or optical) matrix elements are calculated using the matrix elements of the velocity operator [92, 112]. We use Wannier functions [63] in order to efficiently sample the Brillouin zone to calculate band structures and dielectric functions [110]. In all calculations, we use the screened hybrid functional of Heyd, Scuseria, and Ernzerhof (HSE) [53]. Our calculation parameters are identical to those described in Section 2.6.

Optical properties are calculated using a 100×100×100 **k**-point mesh for the cubic phase, 30×30×30 for the monoclinic phase, and 10×10×10 for the amorphous phase.

7.2.2 Determination of Fermi Level

In our calculations for both crystalline and disordered structures, we use the rigid band approximation. We adjust the Fermi level to achieve a particular electron concentration using the calculated density of states. We first fix what the target doping concentration is based on number of excess electrons per unit volume. Using the fact that the total electron concentration n in the system is

$$n = \int d\epsilon \, g(\epsilon) \cdot f(\epsilon), \tag{7.1}$$

where $g(\epsilon)$ is the density of states and $f(\epsilon)$ is the Fermi-Dirac distribution, we find the corresponding Fermi level ϵ_F that gives the desired the target doping concentration.

Table 7.1: Fermi level ϵ_F (eV) with respect to the conduction band minimum for crystalline structures. In parentheses is the corresponding number of electrons per formula unit.

n (cm^{-3})	Cubic	Monoclinic
10^{18}	-0.14 (5.43×10^{-5})	-0.11 (5.51×10^{-5})
10^{19}	-0.081 (5.43×10^{-4})	-0.047 (5.51×10^{-4})
10^{20}	-0.0039 (5.43×10^{-3})	0.034 (5.51×10^{-3})
10^{21}	0.17 (5.43×10^{-2})	0.30 (5.51×10^{-2})

Table 7.2: Fermi level ϵ_F (eV) with respect to the conduction band minimum for disordered structures. The equivalent number of electrons per formula unit is 5.43×10^{-2}.

Structure	ϵ_F (eV)
A	0.047
B	0.32
C	0.051

Tables 7.1 and 7.2 give the Fermi level for the structures considered. For each of the disordered structures, the states within the grey region as shown in Fig. 7.3 are omitted.

7.2.3 Generation of Disordered Structures

To generate disordered structures we use molecular dynamics simulations as described in Section 2.5, following the general procedure outlined in Ref. [142]. The disordered phase is constructed from a 3×3×3 supercell of the cubic structure (equivalent to 27 formula units). A **k**-point mesh of 2×2×2 is used; higher meshes of 3×3×3 were tested, leading to energy differences of less than 5 meV. The amorphous phase is quenched from a "melted" phase. This melted phase is achieved with a microcanonical ensemble that is allowed to equilibrate at T = 5000 K. The time step was $\Delta t = 2.0$ fs. In order to ensure any order has vanished, structures were sampled once atoms moved

on average at least one nearest-neighbor distance. As the W atom is much more massive than the O atom, it moves more slowly in molecular dynamics simulations. This is circumvented by reducing the W mass to 40 amu [142]. After equilibration, every 250 time steps a structure was taken and rapidly quenched to room temperature. We choose a structure every 250 time steps in order to ensure that structures are distinct from each other. Quenching occurred for 1000 time steps and the structure was then allowed to equilibrate at room temperature for an additional 500 steps.

GGA is used for molecular dynamics simulations, followed by a single self-consistent HSE calculation for calculating optical properties. We performed this procedure to obtain 3 structures, which we label as Structures A, B, and C. The range of bond lengths and angles for the structures generated are comparable to those reported in Ref. [142].

7.3 Atomic and Electronic Structure of Disordered Phases

The electronic and structural parameters for the cubic and monoclinic phases are described in Chapters 1 and 5. Here, we describe the electronic and structural parameters of the disordered phases, using the monoclinic phase as a reference.

Our objective is to capture representative structural features of the disordered solid, not to provide a comprehensive description of the disordered phase. The disordered structure differs from the crystalline phases in that bond lengths have a wider distribution and deviations from 6-fold coordination become possible. In Fig. 7.1 we compare W-O and W-W bond lengths in the monoclinic and amorphous phases. Results for amorphous reflect values accumulated for Structures A, B, and C. The W-O distances peak

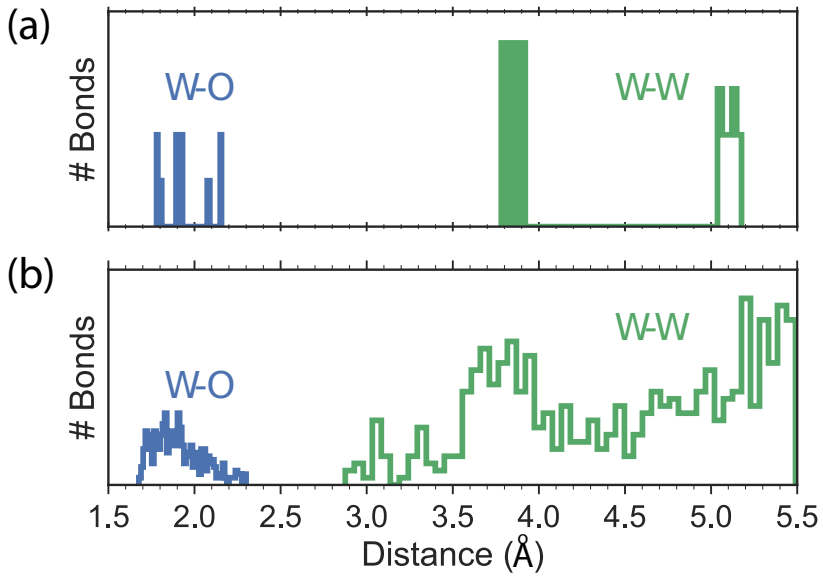

Figure 7.1: Distribution of W-O and W-W bond lengths in the (a) monoclinic and (b) disordered structures, using a cutoff of $r = 2.30$ Å for W-O and $r = 5.5$ Å for W-W distances.

at approximately 1.89 Å (the bond length in the cubic phase) and display a broadening that tails off around 2.3 Å; they show distinct broadening compared to the crystalline phase. Similar observations apply to the W-W distances, which peak around 3.78 Å (the lattice constant of the cubic phase).

The O-W-O bond-angle distribution is shown in Fig. 7.2. In the cubic phase the bond angles are 90°; in the monoclinic phase the angles spread between approximately 80° and 100°. This range is significantly broadened in the amorphous structures [Fig. 7.2(b)]. The wide range of possible O-W-O bond angles is indicative of the disrupted octahedral structure. These changes and distributions are consistent with those observed in previous studies of the amorphous phase [142].

Other major changes to the atomic structure occur upon amorphization. Melting disrupts the 6-fold coordination of W, leading to a distribution of possible coordinations. Unlike in the cubic and monoclinic phases where all W are 6-fold coordinated, 4-, 5-, and 6-fold coordinations are found in the amorphous structure. We consider W and O to

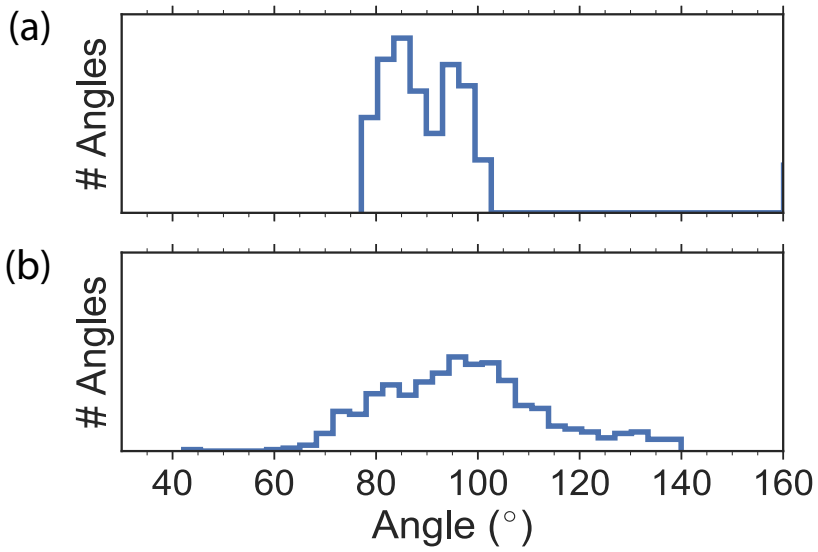

Figure 7.2: Distribution of relative number of O-W-O bond angles for the (a) monoclinic and (b) disordered structures.

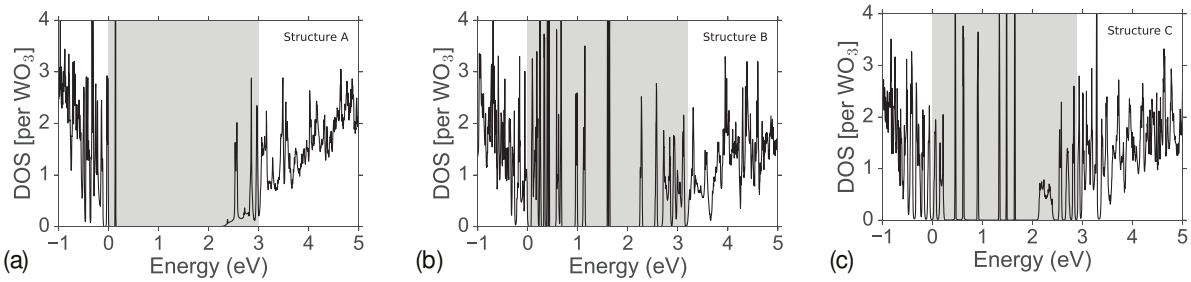

Figure 7.3: Total density of states for the three disordered structures, (a) Structure A, (b) Structure B, and (c) Structure C. The zero of energy corresponds to the VB maximum. The edges of the shaded region corresponds to the VB maximum and CB minimum; states within this region are ignored in calculated optical spectra.

be part of an octahedron if they are less than 2.3 Å apart from each other. Among the three structures sampled, around 33% of the possible W centers are 4-fold coordinated, 50% are 5-fold coordinated, and the remaining are 6-fold coordinated.

The changes in the crystal structure lead to significant changes in the electronic structure. We observe a band narrowing compared to crystalline phases. The band width of the W d states (combined t_{2g} and e_g states) is 13.2 eV in the cubic phase; 8.9 eV in the monoclinic phase; and 8.4 eV, 8.4 eV, and 7.3 eV for the amorphous structures. Similar band narrowing has been found previously for amorphous WO_3 [142].

Figure 7.3 shows the electronic density of states for the amorphous structures. As expected, states appear in the band gap, corresponding to localization and/or the formation of defects in the disordered structure. For purposes of analyzing the electronic structure and absorption spectra, we identify a band gap by checking the degree of localization of states. For both the VB and CB, we take the band edge to be the first electronic state not associated with any particular defect or localized state of the structure. Inspection of the charge density indicates whether a state is localized (on the scale of a few atoms) versus delocalized (distributed over a majority of atoms in the supercell). Our choice of band edges is shown in the shaded regions in Fig. 7.3.

Structure A is free of localized states far from the band edges, while Structures B and C have localized states throughout the gap. In Structure A, the localized states near the VB are primarily from undercoordinated O, and those near the CB come from edge-sharing octahedra or undercoordinated W. In contrast, in Structure B the states in the gap at slightly less than 1 eV above the VB arise from neighboring oxygen atoms in configurations with small W-O-W bond angles; these oxygens interact more strongly within the same octahedra (smallest separation distance is 1.47 Å). They can also arise from interactions between oxygens in two separate octahedra. The gap state just above 1 eV is associated with several undercoordinated O, in addition to a pair of W-W separated

by 2.77 Å in edge-sharing octahedra. This W-W distance is less than that in the bulk and leads to greater hybridization between the adjacent W, resulting in a gap state.

Like Structures A and B, the localized states in Structure C near the VB maximum are derived from undercoordinated oxygens and interactions of two oxygens in separate octahedra spaced closer than the typical O-O distance. The states near mid-gap arise from atoms positioned in edge-sharing octahedra and from undercoordinated W. While edge-sharing octahedra are also present in Structure A, the W of edge-sharing octahedra in Structure C are spaced closer together (by up to 0.1 Å). This smaller separation of edge-sharing W in Structure C leads to localized states further from the CB edge.

While it is informative to examine the character of these defect states, the concentration at which they occur in our simulations is much higher than expected in a realistic disordered solid due to the limited size of our supercells. These defects would therefore have a spuriously large impact on the optical absorption. For purposes of analyzing the absorption spectra, we have therefore removed these localized states from our calculations, by omitting them from the sum over bands in Eq. (3.34).

The inclusion of localized states does not change our conclusions. We show an explicit calculation of CB $\rightarrow$ CB transitions for different choices of band edges for Structure B in Fig. 7.4. The detailed features that occur at specific energies are due to the specifics of the disordered structure (modeled in a modest-size supercell); on average, the absorption changes by less than a factor of 2. In a real system, the concentration of localized or defect states would be far smaller than in our models, and would have an even smaller impact on absorption.

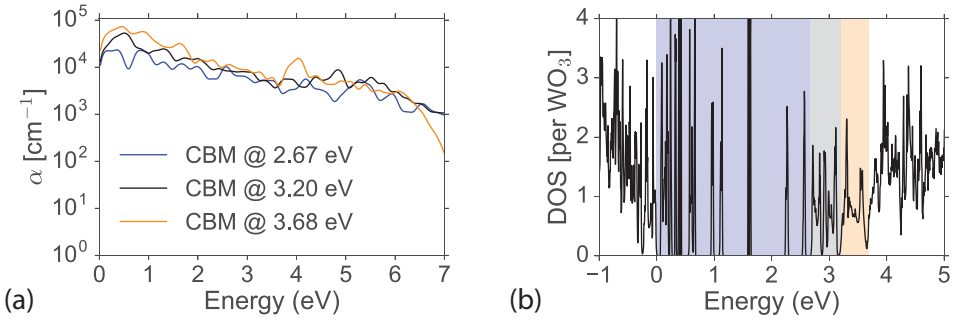

Figure 7.4: (a) Absorption spectra for disordered Structure B for three different choices of conduction-band edge. (b) Choice of conduction-band edge illustrated within the total density of states for Structure B. The valence-band edge is kept fixed (and chosen as the zero of energy). Each colored box corresponds to a different choice of the CB edge.

7.4 Results on Optical Spectra

We next report results for doping up to 10^{21} cm^{-3}. In order to elucidate the contribution of induced carriers to absorption, we distinguish between transitions from valence to conduction states (VB $\rightarrow$ CB) and transitions between initial states filled with induced carriers and higher-lying conduction bands; we refer to these as CB $\rightarrow$ CB transitions.

7.4.1 Crystalline WO_3

First, we consider the cubic and monoclinic phases. While the cubic phase has no structural distortion, the monoclinic phase contains rotations of the octahedra and displacement of the W atom from the center of the octahedra. Our calculated lattice parameters and band gaps for the crystalline phases are in good agreement with experimental results and with previous computational investigations based on HSE (see Ref. [156]). The band structures, along with information about optical transition matrix elements, are presented in Fig. 7.5. The calculated band gap is 1.53 eV in the cubic and 2.56 eV in the monoclinic phase. The valence bands have predominantly O $2p$ character, and the conduction bands are comprised primarily of W $5d$ states, separated into t_{2g}

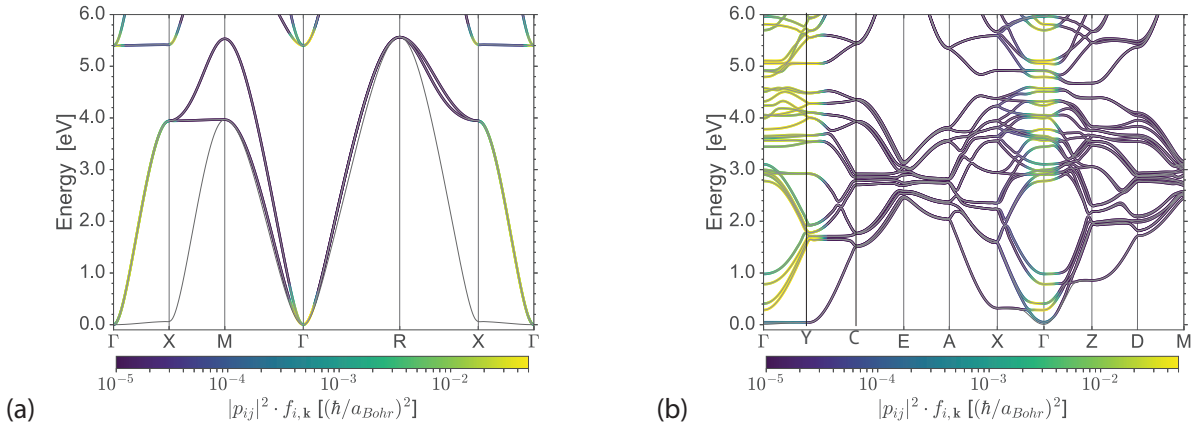

Figure 7.5: Electronic band structure of conduction bands in (a) cubic and (b) monoclinic phases of WO_3 calculated with HSE. The zero of energy is set at the CB minimum. Conduction bands are colored according to the strength of optical transitions to higher-lying bands weighted by the occupation factor, i.e., according to the sum of $|p_{ij}|^2$ for CB $\rightarrow$ CB transitions weighted by the occupation factor $f_{i,\mathbf{k}}$. i is the initial occupied state, and j is the band in question. Occupations are at room temperature based on 10^{21} cm^{-3} doping.

and e_g states due to crystal-field splitting in an octahedral environment.

The calculated imaginary part of the dielectric function ε_2 for both phases is shown in Figs. 7.6(a) and 7.6(b). The corresponding absorption spectra are shown in Fig. 7.7. Our ε_2 spectra for the undoped case compare well with spectra based on the G_0W_0 and Bethe-Salpeter approximation [183], as well as those derived from experimental reflectivity spectra [185]. The onset of VB $\rightarrow$ CB absorption occurs at much higher energy in monoclinic compared to cubic; this is due to a suppression of optical transitions from the highest VBs to the lowest CBs. Our calculations show that each order of magnitude increase in doping leads to roughly an order of magnitude increase in absorption for CB $\rightarrow$ CB transitions, as shown in Figs. 7.7(a) and 7.7(b).

We first focus on the cubic phase [Figs. 7.6(a) and 7.7(a)]. A notable feature is the Burstein-Moss shift, which is the increase in optical band gap due to electrons occupying the lower CB states. This shift is minimal for doping up to 10^{19} cm^{-3}. At 10^{20} cm^{-3} the Burstein-Moss shift is 0.01 eV, and it increases to 0.16 eV for 10^{21} cm^{-3}. These shifts

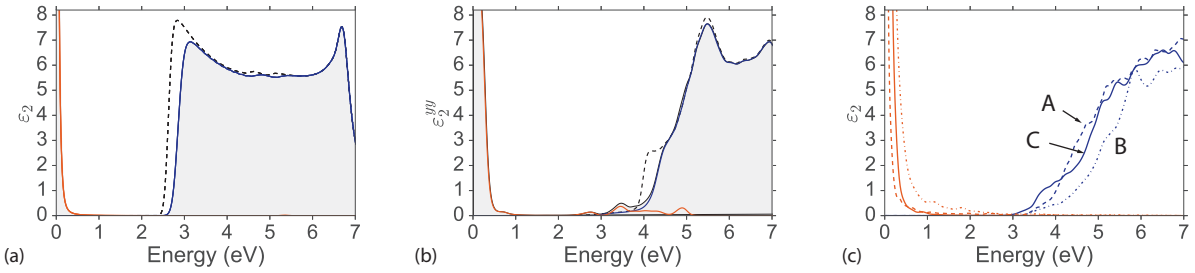

Figure 7.6: Imaginary part of the dielectric function ε_2 for (a) the cubic phase, (b) the monoclinic phase (yy-component only), and (c) three disordered structures of WO_3, at 10^{21} cm^{-3} doping. VB $\rightarrow$ CB contributions are shown in blue, CB $\rightarrow$ CB in orange. The respective undoped spectrum (dotted black line) is shown for the crystalline phases.

are modest, even at the highest doping levels, due to the presence of the low-dispersion conduction band along the $\Gamma \rightarrow$ X direction, which sustains a high density of states. The peak in ε_2 at 2.75 eV coincides with VB $\rightarrow$ CB energies from the flat valence bands to the flat portions of the lower-lying t_{2g} conduction-band states along the $\Gamma \rightarrow$ X direction [Fig. 7.5(a)].

Figures 7.6(a) and 7.7(a) show that the introduction of excess carriers leads to strong absorption in the infrared. At a doping level of 10^{21} cm^{-3}, α reaches 10^4 cm^{-1}, and then tails off to 10^2 cm^{-1} in the visible range before another peak emerges above 5.0 eV. The peak above 5.0 eV corresponds to transitions to e_g states.

In the monoclinic structure, the structural distortions break the degeneracies in electronic states of the cubic phase, leading to additional allowed transitions. The Burstein-Moss shift is small for doping up to 10^{20} cm^{-3}, and amounts to 0.07 eV for 10^{21} cm^{-3}. Similar to the cubic phase, these shifts are small due to the flat bands along the $\Gamma \rightarrow$ Y direction [Fig. 7.5(b)]. Absorption is strongest corresponding to ε_{yy}; ε_{xx} is comparable to ε_{yy}, but ε_{zz} is an order of magnitude smaller. Absorption of light polarized along the Cartesian x and y directions is about an order of magnitude stronger than along the z direction.

Figure 7.7(b) shows the absorption spectra as a function of doping in the monoclinic phase. At 10^{20} cm^{-3}, carrier-induced absorption reaches almost 10^3 cm^{-1} in the infrared; in the visible, absorption exceeding 10^3 cm^{-1}) occurs in the blue region of the spectrum. These features are enhanced at the higher doping level of 10^{21} cm^{-3}: absorption in the infrared exceeds 10^4 cm^{-1}, and in the visible it is higher than 10^3 cm^{-1}, rising to above 10^4 cm^{-1} in the blue.

Focusing on the visible regime, we see that absorption in the cubic phase tapers off at higher energies, while in the monoclinic phase it is more constant and shows a peak just below 3 eV. This blue peak originates from strong transitions to a set of t_{2g} bands around 2.8 eV above the CB minimum, as can be seen in Fig. 7.5. No such transitions occur in the cubic phase; they become allowed due to the structural distortions present in the monoclinic phase.

7.4.2 Disordered WO_3

Since the enhancement of CB $\rightarrow$ CB absorption in the monoclinic phase is due to the presence of distortions, we expect even stronger absorption in amorphous structures. The disorder introduces defects which lead to localized states in the band gap; as discussed in Section 7.3, for the purposes of calculating absorption we neglect these states and take the band edge to be the first electronic state not associated with a defect or localized state of the structure. We verified that our results for optical absorption are not sensitive to the exact choice of the band edges. We generate three disordered structures, referring to them as Structures A, B, and C, with band gaps 3.01, 3.20, and 2.90 eV.

Figure 7.6(c) shows ε_2 and Fig. 7.7(c) the carrier-induced absorption spectra for the three disordered structures. We focus on a carrier concentration of 10^{21} cm^{-3}, which is a typical doping level [167]. Relative to the crystalline phases, the spectra are

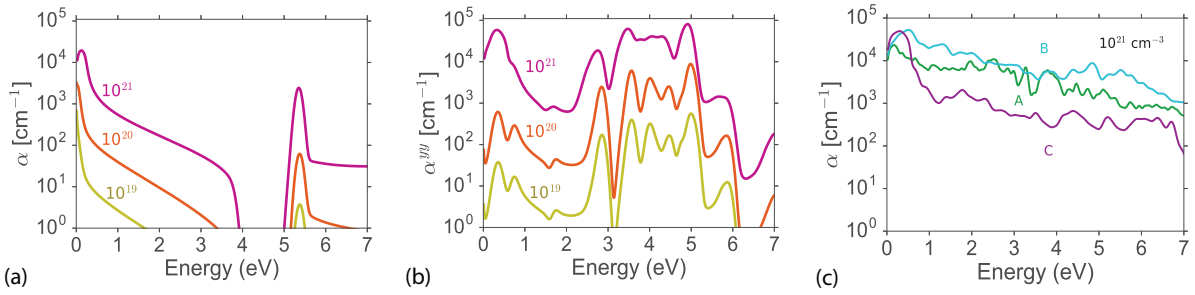

Figure 7.7: Absorption spectra (on a logarithmic scale) for CB → CB transitions for (a) the cubic, (b) the monoclinic phase, and (c) for three disordered structures of WO_3. For the cubic and monoclinic phases, results are shown for three doping levels (10^{19}, 10^{20}, and 10^{21} cm^{-3}); for the disordered phase, the doping level is 10^{21} cm^{-3}.

broadened, with strong absorption across all photon energies. This broadening reflects the wider distribution of atomic bond lengths and angles in the disordered structures (see Section 7.3).

7.4.3 Microscopic Origins of Enhanced Optical Absorption

We now discuss how the electronic structure and optical matrix elements contribute to carrier-induced optical transitions. Transitions in the infrared occur due to the presence of multiple conduction-band states with small energy differences. The $1/\omega^2$ factor in ε_2 [Eq. (3.34)] leads to a large peak as the photon energy approaches zero (Fig. 7.6). This enhancement is not present in the absorption coefficient α, which is proportional to $1/\omega$.

To correlate the enhancement of absorption in the visible with structure distortion, we examine the dipole matrix elements, which measure the strength of the optical transitions. Information about these matrix elements is included in Fig. 7.5. Transitions can only take place if initial states are occupied, and therefore the strength of optical transitions is weighted by the Fermi occupation (for a doping level of 10^{21} cm^{-3}) of the conduction-band states. As multiple bands can be occupied at 10^{21} cm^{-3} doping, we

sum the occupation-weighted square of the matrix elements associated with transitions originating from these occupied states. If the conduction bands had purely W-5d character, all optical transitions would be forbidden because of the selection rule that requires $|\Delta l|$=1. Hybridization between the W 5d and O 2p states relaxes this restriction, and leads to transitions between conduction bands that are remarkably strong.

This can be seen when comparing cubic and monoclinic WO_3. The transition strength relates to the nature of the initial and final states. In cubic WO_3, strong transitions occur along $\Gamma \rightarrow$ X, $\Gamma \rightarrow$ R, and $\Gamma \rightarrow$ M (in Fig. 7.5 the transition strength is weighted by the occupation of the initial states). Such transitions are still present in the monoclinic phase, but they are supplemented by transitions in the visible that become allowed due to symmetry lowering. The distortions of the monoclinic structure cause increased mixing of W d and O p states, in particular allowing transitions to states around 2.8 eV above the CB minimum.

In the disordered structures, the extent of hybridization further increases due to larger structural distortions, leading to even larger absorption. The trends in Fig. 7.7 clearly indicate that larger structural distortions, through enhanced hybridizations, lead to a strong increase in the strength of the optical transitions.

7.5 Comparison with the Drude Model

Several studies have performed fits to the Drude model as a means of explaining measured optical behavior of excess carriers [150, 186, 180, 187]. It is thus instructive to perform a comparison of our first-principles calculations with the phenomenological Drude model as presented in Section 3.1.1.

Before delving into a case study of WO_3, a note on semantics is necessary. The Drude model as presented here is a classical model for describing electron conductiv-

ity and response. It bears resemblance to the plasma response of a metallic system, which describes the collective excitation of electrons. The Drude response is a distinct phenomenon compared to the single-particle excitations described in direct absorption. Thus, a comparison would not be meaningful. Nevertheless, because the Drude model is often invoked, it is insightful to see what qualitative and quantitative differences arise when trying to describe a highly-doped semiconductor as a simple metal. A useful summary for understanding the various contributions to the linear response of electrons may be found in Ref. [188].

Here, we use experimental parameters or typical values as input to the Drude model for WO_3. The scattering rate is taken to be 10^{-14} s^{-1}, which is a typical value for oxides [189] and representative of the scattering rate in WO_3. The mobility is varied between 10 and 200 $cm^2/V{\cdot}s$, which covers the range of typical and relevant mobilities found for WO_3 as discussed in Chapter 6. For mobilities based on the Drude model, the effective mass m^* is taken to be $0.25m_0$ - $1.0m_0$. This range of effective masses is meant to reflect on average the effective masses of the cubic and monoclinic phases, as presented in Table 7.3. Mobilities calculated from the Drude model in Eq. 3.27 range between 17 and 70 $cm^2/V{\cdot}s$.

In Fig. 7.8, the range of variation in ε_2 and absorption coefficient of treating WO_3 in the Drude approximation is shown. The calculated plasma frequencies for 10^{18} - 10^{21} cm^{-3} doping are $\omega_p = 0.03, 0.09, 0.30, 0.96$ eV, well within the infrared regime. Comparing Fig. 7.8 with the spectra in crystalline and amorphous WO_3 in Section 7.4, it is clear the Drude model does not capture the band-structure induced features in the dielectric function that are found in our calculations and also have been measured experimentally [185]. These results emphasize that the Drude model is inadequate to describe the optical properties of WO_3.

Table 7.3: Band effective masses for cubic (reproduced for convenience) and monoclinic phases of WO_3 for the three lowest-lying conduction bands as calculated using the hyperbolic fit, as described in Chapter 6. Effective masses m_i^* are indexed by band i, starting from the lowest-lying band. SOC is included.

	m_1^*	m_2^*	m_3^*
RT Monoclinic, $P2_1/c$			
$\Gamma \rightarrow$ X	0.29	0.25	0.44
$\Gamma \rightarrow$ Y	1.07	14.8	0.36
$\Gamma \rightarrow$ Z	0.29	0.25	1.81
Cubic, $Pm\bar{3}m$			
$\Gamma \rightarrow$ X	0.17	0.18	0.20
$\Gamma \rightarrow$ R	0.18	0.14	0.17
$\Gamma \rightarrow$ M	0.22	0.17	0.26

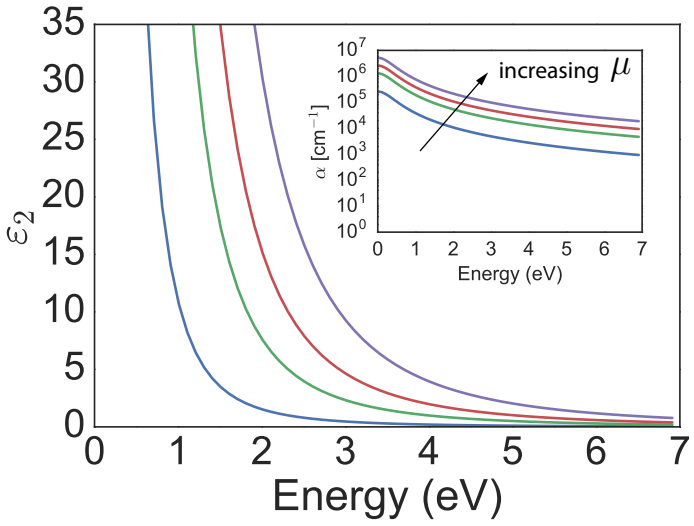

Figure 7.8: Imaginary part of the dielectric function and corresponding absorption coefffcient using the Drude model with different parameters at 10^{21} cm^{-3} doping. The different curves correspond to varying mobilities [cm^2/V·s]: 10 (blue), 50 (green), 100 (red), 200 (purple).

7.5.1 A Mechanism for Coloration

As an electrochromic material, WO_3 has been reported to change color upon intercalation of alkali dopants [190, 180] and in the presence of oxygen deficiencies [122, 191]. Several mechanisms for the coloration have been proposed. In the first mechanism [147, 192], excess carriers are proposed to form polarons, reducing the formal oxidation state of W^{6+} to W^{5+} or W^{4+}. Absorption would occur when polarons hop between sites. This is a valid mechanism, but the energy absorbed in polaron hopping is relatively small, typically below 0.5 eV [192]. So, while this could explain the observed absorption in the infrared, it cannot be responsible for coloration at visible wavelengths. In addition, we have previously shown that small polarons are not stable in crystalline WO_3 [156].

In the second proposed mechanism, sub-band-gap defect states lead to absorption [130]. Transitions from a defect level to the band edge would occur at energies well below the band-gap energy and again cannot explain absorption in the visible. We have also shown that oxygen vacancies, which have been commonly suggested as the source of deep defect levels [130], are actually shallow donors in crystalline WO_3, with defect states resonant with the conduction band [116]. These mechanisms therefore do not explain the strong absorption in the visible that is necessary to explain coloration.

In the present work we focus on a third mechanism, namely the absorption of photons by carriers that are induced by doping. Free-carrier absorption has been suggested before [149, 150, 180], but only in the context of the phenomenological Drude model, which cannot be expected to produce reliable results at visible wavelengths. The carrier-induced absorption mechanism studied here leads to significant absorption not just in the infared but also at visible wavelengths.

We note that direct absorption by excess carriers is not limited to electrons that

are in extended states; even if localization occurs (which is more likely in disordered structures), excitation of electrons out of such states into higher-lying conduction-band states will give rise to similar absorption spectra as described above (see Fig. 7.3 for spectra calculated with localized states included).

For practical applications, the transmittance is the quantity of interest, which can be correlated with the calculated carrier-induced absorption. The expected fraction of incident light transmitted can be calculated with $T = e^{-\alpha d}$, where α is the absorption coefficient and d is the thickness of the material; we neglect any reflection and assume normal incident light. Typical sample thicknesses range from 100 nm to a few microns; for such thicknesses, absorption coefficients need to be significantly larger than 10^2 cm^{-1} to result in perceptible darkening. We calculated that at a doping level of 10^{21} cm^{-3}, α in amorphous samples can be 10^4 cm^{-1} or higher in the visible range, with higher values in the red region of the spectrum. Even for a relatively thin film, with a thickness of 100 nm, this leads to a 10% drop in transmittance and perceptible darkening. This confirms that carrier-induced direct absorption is the likely mechanism for coloration.

We next take our calculated spectra and explicitly compute the associated color, as described in the following section.

7.6 From Optical Spectra to Human Perception of Color

A key finding in this work is that direct transitions from excess carriers contribute significantly to absorption in the visible range. While it is quantitatively useful to compute the optical spectra, it is difficult to predict how that translates to the coloration of the sample. In this section, we discuss the framework for converting quantitative

spectra into color as perceived by humans.

The mathematical mapping from standard illumination and observation conditions to color as perceived by humans was standardized in the early 1930s by the CIE (Commission Internationale de l'Eclairage) [193]. While various extensions and improvements were made later, the CIE 1931 standard remains a popular choice. The CIE color space has been extended into various mathematical representations (e.g., RGB, XYZ); for the purpose of this dissertation, we use the XYZ-coordinate space as they can be directly computed from optical spectra. We shall cover the basic components behind the CIE 1931 standard of optical spectra to human-perceived color.

We begin with a brief description of the anatomy of the human eye. The human eye is lined with photoreceptors that are categorized as either rods or cones, depending on the proteins present. Rods operate at low levels of light and contribute to our night vision. Cones are activated at high levels of light and are responsible for our perception of color. A simple schematic illustrating the anatomy of the human eye is shown in Fig. 7.9(a). Three types of cones are present; each activates in a different part of the visible spectrum. The statistically representative relative activity of the three types of cones in the human population are shown in Fig. 7.9(b). These relative activities are known as the tristimulus values, which are a measure of the spectral sensitivity of cones at short, medium, and long wavelengths.

The color matching tristimulus functions are used to compute the corresponding coordinates in the XYZ-color space from a transmittance spectra. The coordinates can be obtained directly from knowing the color matching functions $(\bar{x}, \bar{y}, \bar{z})$, choosing an

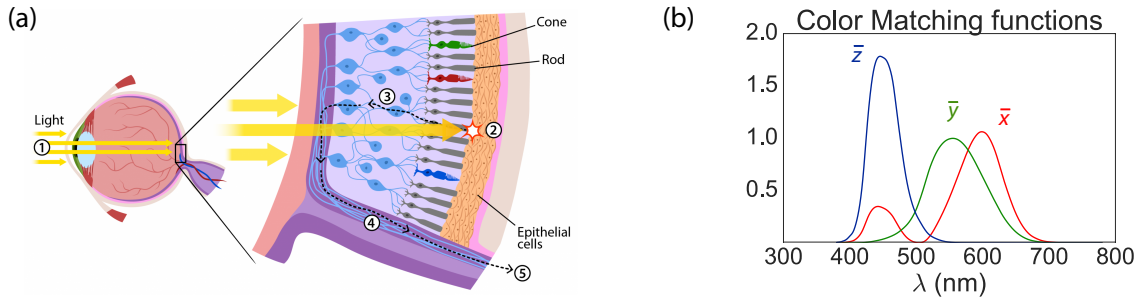

Figure 7.9: (a) Schematic of the anatomy of the human eye, illustrating light hitting the eye and being detected by the rods and cones. From Ref. [194]. (b) Tristimulus color matching functions in the visible spectrum for a standard observer in CIE 1931 standard.

illuminant I, and having the transmittance spectra S, defined as

$$X = \frac{1}{N}\int d\lambda\, \bar{x}(\lambda)\, S(\lambda)\, I(\lambda), \tag{7.2a}$$

$$Y = \frac{1}{N}\int d\lambda\, \bar{y}(\lambda)\, S(\lambda)\, I(\lambda), \tag{7.2b}$$

$$Z = \frac{1}{N}\int d\lambda\, \bar{z}(\lambda)\, S(\lambda)\, I(\lambda), \tag{7.2c}$$

$$N = \int d\lambda\, \bar{y}(\lambda)\, I(\lambda). \tag{7.2d}$$

Together, X, Y, and Z define a three-dimensional color space. Another coordinate space is the xyY-chromaticity coordinates, defined as

$$x = \frac{X}{X+Y+Z}, \tag{7.3a}$$

$$y = \frac{y}{X+Y+Z}, \tag{7.3b}$$

$$Y = Y, \tag{7.3c}$$

in which x and y represent a slice of the chromaticity diagram [see Fig. 7.10(b)] and Y corresponds to the illumination of the object, i.e., how dark or light the shading is. The color space can be plotted in three dimensions as a chromaticity plot, shown in Fig. 7.10.

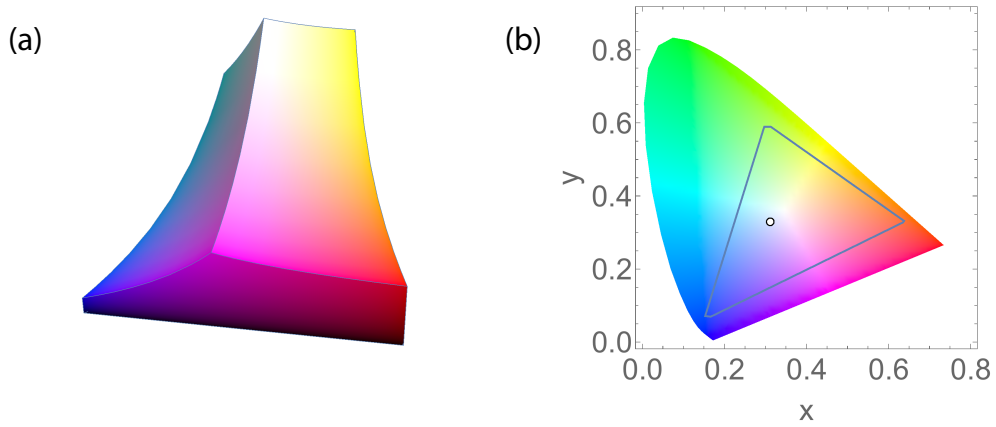

Figure 7.10: (a) 3D chromaticity plot in the CIE 1931 standard. (b) a two-dimensional slice of (a) in xy-plane of xyY-color space. The triangle corresponds to the range of colors available to a standard computer monitor, and the small circle represents the point corresponding to the color white

We now calculate the transmittance spectra of the cubic, monoclinic, and amorphous phases. Typical thicknesses range between 100 nm to several μm. In all transmittance plots, we assume $n = 10^{21}$ cm^{-3} doping and thickness of 500 nm.

Figure 7.11 shows the calculated transmittance for the cubic, monoclinic, and a representative disordered structure, as well as the anticipated perceived coloration. The color expected from the total transmittance (i.e., both VB $\rightarrow$ CB and CB $\rightarrow$ CB) is also displayed. As structural distortions increase, the color due to excess carriers becomes more blue. The greenish colors in the crystalline phases arise from the smaller optical band gaps compared to the disordered phases.

Amorphous WO_3 films are the most useful in electrochromic applications, as they are transparent in the visible. The blue we find for disordered WO_3 from our calculations is consistent with experimental observations of the blue coloration for doping WO_3 [195, 142, 124, 181].

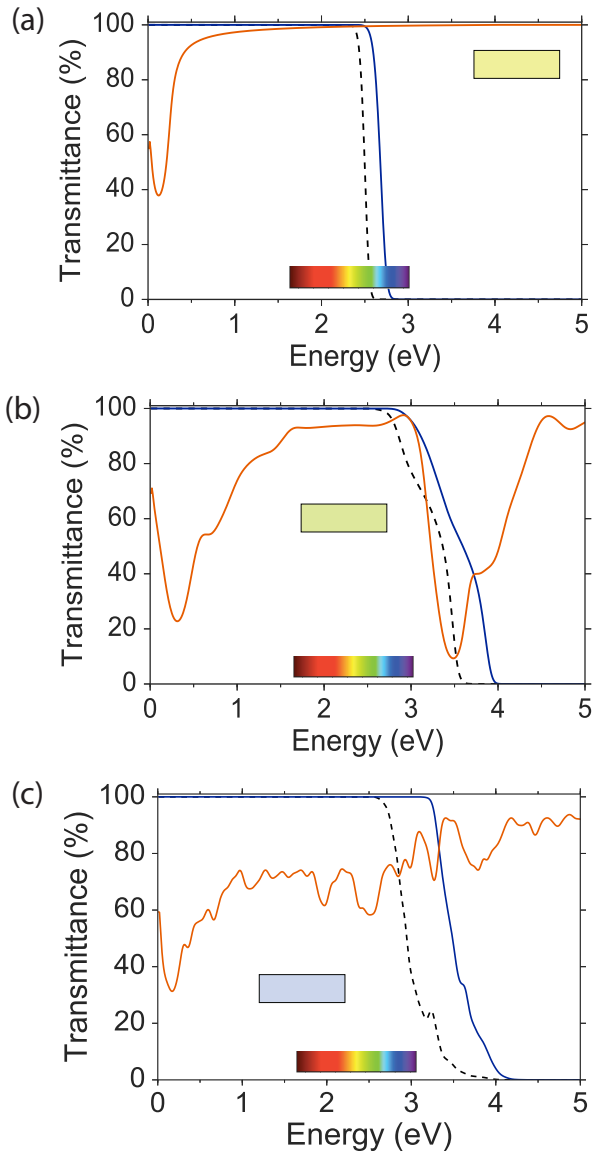

Figure 7.11: Calculated transmittance for $n = 10^{21}$ doping through a 500 nm sample of the (a) cubic, (b) monoclinic, and (c) Structure A of disordered configurations. The dotted black line corresponds to the transmittance of the undoped sample; blue and orange lines associated with VB $\rightarrow$ CB and CB $\rightarrow$ CB transitions, respectively. The predicted perceived color is shown in the colored boxes, corresponding to the color resulting from the total spectrum. For reference, the visible spectrum is superimposed on the horizontal axis.

7.7 Conclusions

We perform state-of-the-art first-principles calculations on the optical properties of WO_3 and investigate the influence of structural distortions in cubic, monoclinic, and disordered WO_3. Our calculations show that strong carrier-induced direct absorption occurs at infrared and visible wavelengths, scaling with the level of doping. We find that structural distortions lead to enhanced absorption due to an increase of hybridization between the W and O states, explaining the increase in absorption strength in going from cubic to monoclinic to disordered structures. Our results demonstrate that carrier-induced absorption provides a consistent explanation for electrochromism.

Chapter 8

Summary and Outlook

8.1 Insights Gained

In this dissertation, a multifaceted look at the influence of high carrier concentrations on the electronic, structural, transport, and optical properties on WO_3 is presented. Using first-principles techniques ranging from density functional theory to molecular dynamics, we developed an understanding of the microscopic effects of excess carriers in WO_3.

1. We have shown that monovalent dopants and oxygen vacancies in WO_3 behave as shallow donors, and that the formation of polarons in the crystalline phase is unlikely. Our study elucidates the microscopic origins of the shallow-donor behavior, connecting atomic relaxations with electronic structure. Our results contribute to a holistic picture of the electronic behavior of these defects and dopants. In the process, we carefully examined the computational treatment of charged defects and the impact of supercell size and choice of functional in DFT.

2. We extended the study of point defects to include the influence of pure electron

doping. From our calculations, we show electron doping is sufficient to reproduce the structural phase transformations from low to high symmetries observed experimentally. Through mapping the phase diagram associated with this phase transformation, we document in detail various parameters for measuring structural distortion in perovskites. In decomposing the energetics of the phase transformation, we demonstrate that the phase transformation arises from the conduction-band offsets between the cubic and monoclinic structures. This work also provides a framework for decomposing electronic-energy gains versus strain-energy costs involved in phase transformations at different doping levels.

Based on the insights we gained on the electronic behavior of defects and dopants, we considered next the transport and optical response of these excess carriers.

3. For transport calculations, we investigate electron-phonon coupling and mobilities using Boltzmann transport theory. We consider electron-phonon scattering as the dominant scattering mechanism at room temperature. Our calculated (unscreened) mobilities are large, higher than the prototypical perovskite STO. We elucidate the underlying factors in the electronic and vibronic structure that lead to such higher mobilities. Our study indicates WO_3 is a promising material for device applications.

4. Finally, we study the influence of structural disorder on absorption due to excess carriers using Wannier interpolation and the random phase approximation. We demonstrate absorption due to excess carriers as an alternate mechanism for electrochromism that wholly explains the drop in transmittance in the infrared and visible, as well as the experimentally observed blue coloration. Cubic, monoclinic, and disordered phases are considered. Our results illustrate how increasing the degree of structural disorder enhances this absorption. Excess carriers introduce

absorption in the infrared and near-infrared wavelengths. The absorption spectra are then converted into transmittance spectra and corresponding human-perceived color.

8.2 Future Directions

Here we outline a number of possible directions for further investigations.

1. Our study of n-type dopants focused on monovalent impurities, specifically the alkali metals. A natural extension would be to examine doping with alkaline earth metals. For applications in which diffusion of dopants is not required, substitutional doping with transition metals could also be considered. While some studies have already been performed [196, 197, 198, 199, 200, 201, 202], a rigorous investigation of these impurities as dopants is still lacking.

2. Our study of charge doping could be extended to investigate the structural changes resulting from including the dopant atoms. Our preliminary investigation found that the size of the dopant has a significant impact on the resulting structural distortion and volume. The presence of the positively charged dopants could counteract the volume expansion, which influences the degree of octahedral distortions present. A more detailed study into this mechanism would elucidate the role of the dopant itself and help resolve differences in predicted phase transition points.

3. An in-depth study could be performed of the effects of oxygen stoichiometry. This could include varying the concentration of oxygen vacancies and studying its effect on coloration. Another interesting aspect would be exploring oxygen interstitials. Oxygen interstitials have been proposed to be responsible for the intercalation cycling degradation in WO_3 devices [203, 204, 205, 206]. Other possibilities include

a detailed analysis of defect complexes, such as with hydrogen. The methods presented in Chapter 4 for studying defects and dopants would be well-suited for such a task.

4. Another natural direction for future investigation is the study of other transition metal perovskites in the same series as WO_3, such as MoO_3, VO_2, or V_2O_5. One issue of particular interest would be an examination of the tendency for polarons to affect transport and optical properties.

5. With respect to the vibrational properties, we found imaginary frequencies in cubic WO_3, which are a sign of a dynamically unstable system. However, it is possible to stabilize the cubic phase either through doping or as a thin film on a cubic substrate. Developing an understanding of the mechanisms by which this crystal structure is stabilized would be of interest. This may require collaboration with experimental measurements of vibrational frequencies, such as Raman and IR spectroscopy.

Longer-term issues that would require more elaborate research efforts include:

1. Relating to transport: 1) inclusion of other forms of scattering, such as ionized impurity scattering; and 2) the impact of screening on results for mobility.

2. Relating to optical absorption, the results presented were only on direct absorption. Indirect absorption should also be considered. Indirect absorption involves electron-phonon interactions, which can be extracted in a similar way to the matrix elements used in Chapter 6. Unlike typical transparent conducting oxides for which there is a singly-degenerate band well separated from the conduction-band manifold [184, 92], the d states in perovskites have many electronic bands with complicated dispersion in the energy range of interest. Thus, a framework

for accurately evaluating both the optical and electron-phonon matrix elements is needed. Practical implementations would rely on parallelization and judicious memory management.

Many of the methodologies used in this dissertation are generalizable to other materials systems and properties. In many device applications, the properties of a material change with carrier doping levels. In this dissertation, we provide an overarching narrative and understanding of how several materials properties are influenced with doping and what microscopic factors contribute to the observed differences. In summary, it is the author's hope that some useful physical insights have been gained in this exercise for understanding the nature and response of excess carriers in a complex oxide system.

Bibliography

[1] B. R. K. Cavin, P. Lugli, and V. V. Zhirnov, "Science and Engineering Beyond Moore's Law." *Proc. IEEE* **100**, 1720 (2012).

[2] P. Zubko, S. Gariglio, M. Gabay, P. Ghosez, and J.-M. Triscone, "Interface Physics in Complex Oxide Heterostructures." *Annu. Rev. Condens. Matter Phys.* **2**, 141 (2011).

[3] J. A. Sulpizio, S. Ilani, P. Irvin, and J. Levy, "Nanoscale Phenomena in Oxide Heterostructures." *Annu. Rev. Mater. Res.* **44**, 117 (2014).

[4] L. Bjaalie, B. Himmetoglu, L. Weston, A. Janotti, and C. G. Van de Walle, "Oxide interfaces for novel electronic applications." *New J. Phys.* **16** (2014).

[5] B. Keimer, S. A. Kivelson, M. R. Norman, S. Uchida, and J. Zaanen, "From quantum matter to high-temperature superconductivity in copper oxides." *Nature* **518**, 179 (2015).

[6] C. N. R. Rao, A. Sundaresan, and R. Saha, "Multiferroic and Magnetoelectric Oxides: The Emerging Scenario." *J. Phys. Chem. Lett.* **3**, 2237 (2012).

[7] L. Bjaalie, A. Janotti, B. Himmetoglu, and C. G. Van de Walle, "Turning $SrTiO_3$ into a Mott insulator." *Phys. Rev. B* **90**, 195117 (2014).

[8] M. Imada, A. Fujimori, and Y. Tokura, "Metal-insulator transitions." *Rev. Mod. Phys.* **70**, 1039 (1998).

[9] T. Wolfram and S. Ellialtioglu, *Electronic and Optical Properties of d-band Perovskites*. Cambridge University Press, Cambridge, UK, 1st edition (2006).

[10] S. Deb, "A Novel Electrophotographic System." *Mater. Lett.* **149**, 127 (1969).

[11] G. A. Niklasson, L. Berggren, and A.-L. Larsson, "Electrochromic tungsten oxide : the role of defects." *Sol. Energy Mater. Sol. Cells* **84**, 315 (2004).

[12] A.-L. Larsson, B. E. Sernelius, and G. A. Niklasson, "Optical absorption of Li-intercalated polycrystalline tungsten oxide films: comparison to large polaron theory." *Solid State Ionics* **165**, 35 (2003).

[13] C.G. Granqvist, "Electrochromic devices." *J. Eur. Ceram. Soc.* **25**, 2907 (2005).

[14] C. Yang, J.-F. Chen, X. Zeng, and D. Cheng, "Enhanced near-infrared shielding ability of (Li,K)-codoped WO_3 for smart windows: DFT prediction validated by experiment." *Nanotechnology* **27**, 75203 (2016).

[15] B. W. Brown and E. Banks, "The Sodium Tungsten Bronzes." *J. Am. Chem. Soc.* **76**, 963 (1954).

[16] Q. Zhong, J. R. Dahn, and K. Colbow, "Lithium intercalation into WO_3 and the phase diagram of Li_xWO_3." *Phys. Rev. B* **46**, 2554 (1992).

[17] A. Hjelm, C. G. Granqvist, and J. M. Wills, "Electronic structure and optical properties of WO_3, $LiWO_3$, $NaWO_3$, and HWO_3." *Phys. Rev. B* **54**, 2436 (1996).

[18] C. G. Granqvist, "Electrochromic tungsten oxide films: Review of progress 1993-1998." *Sol. Energy Mater. Sol. Cells* **60**, 201 (2000).

[19] A. Staerz, U. Weimar, and N. Barsan, "Understanding the Potential of WO_3 Based Sensors for Breath Analysis." *Sensors* **16**, 1815 (2016).

[20] S. Moulzolf, L. LeGore, and R. Lad, "Heteroepitaxial growth of tungsten oxide films on sapphire for chemical gas sensors." *Thin Solid Films* **400**, 56 (2001).

[21] Y. Ping, Y. Li, F. Gygi, and G. Galli, "Tungsten Oxide Clathrates for Water Oxidation: A First Principles Study." *Chem. Mater.* **24**, 4252 (2012).

[22] J. Takashima, N. Oka, and Y. Shigesato, "Photocatalytic Activity of WO_3 Films Crystallized by Postannealing in Air." *Jpn. J. Appl. Phys.* **51**, 055501 (2012).

[23] S. Yoon, C. Jo, S. Y. Noh, C. W. Lee, J. H. Song, and J. Lee, "Development of a high-performance anode for lithium ion batteries using novel ordered mesoporous tungsten oxide materials with high electrical conductivity." *Phys. Chem. Chem. Phys.* **13**, 11060 (2011).

[24] K. Mahmood, B. S. Swain, A. R. Kirmani, and A. Amassian, "Highly efficient perovskite solar cells based on a nanostructured WO_3-TiO_2 core-shell electron transporting material." *J. Mater. Chem. A* **3**, 9051 (2015).

[25] P. Yu and M. Cardona, *Fundamental of semiconductors: Physics and Materials Properties* (2010).

[26] N. W. Ashcroft and N. D. Mermin, *Solid State Physics*. Saunders College, Philadelphia (1976).

[27] J. J. Solyom, *Fundamentals of the physics of solids. Volume I, Structure and dynamics*. Springer-Verlag, Berlin (2007).

[28] J. J. Solyom and A. Piroth, *Fundamentals of the physics of solids. Volume 2, Electronic properties*. Springer-Verlag, Berlin (2009).

[29] K. R. Locherer, I. P. Swainson, and E. K. H. Salje, "Phase transitions in tungsten trioxide at high temperatures - a new look." *J. Phys. Condens. Matter* **11**, 6737 (1999).

[30] A. M. Glazer, "The classification of tilted octahedra in perovskites." *Acta Crystallogr.* **B28**, 3384 (1972).

[31] M. A. Islam, J. M. Rondinelli, and J. E. Spanier, "Normal mode determination of perovskite crystal structures with octahedral rotations: theory and applications." *J. Phys. Condens. Matter* **25**, 175902 (2013).

[32] A. Garg, *Growth and characterization of epitaxial oxide thin films*. Ph.D. thesis, University of Cambridge (2001).

[33] H. Hamdi, E. K. H. Salje, P. Ghosez, and E. Bousquet, "First-principles reinvestigation of bulk WO_3." *Phys. Rev. B* **94**, 245124 (2016).

[34] F. Wang, C. Di Valentin, and G. Pacchioni, "Electronic and structural properties of WO_3: A systematic hybrid DFT study." *J. Phys. Chem. C* **115**, 8345 (2011).

[35] R. Sivakumar, R. Gopalakrishnan, M. Jayachandran, and C. Sanjeeviraja, "Preparation and characterization of electron beam evaporated WO_3 thin films." *Opt. Mater. (Amst).* **29**, 679 (2007).

[36] F. P. Koffyberg, K. Dwight, and A. Wold, "Interband transitions of semiconducting oxides determined from photoelectrolysis spectra." *Solid State Commun.* **30**, 433 (1979).

[37] G. Hodes, D. Cahen, and J. Manassen, "Tungsten trioxide as a photoanode for a photoelectrochemical cell (PEC)." *Nature* **260**, 312 (1976).

[38] R. D. Bringans, H. Höchst, and H. R. Shanks, "Defect states in WO_3 studied with photoelectron spectroscopy." *Phys. Rev. B* **24**, 3481 (1981).

[39] T. Vogt, P. M. Woodward, and B. A. Hunter, "The High-Temperature Phases of WO_3." *J. Solid State Chem.* **144**, 209 (1999).

[40] W. Kehl, R. Hay, and D. Wahl, "The Structure of Tetragonal Tungsten Trioxide." *J. Appl. Phys.* **212**, 4 (1952).

[41] W. A. Crichton, P. Bouvier, and A. Grzechnik, "The first bulk synthesis of ReO_3-type tungsten trioxide, WO_3, from nanometric precursors." *Mater. Res. Bull.* **38**, 289 (2003).

[42] R. M. Martin, *Electronic Structure: Basic Theory and Practical Methods*. Cambridge University Press, New York (2008).

[43] J. B. Varley, *First-principles calculations of conductivity in transparent semiconducting oxides*. Ph.D. thesis, University of California, Santa Barbara (2011).

[44] P. Hohenberg and W. Kohn, "Inhomogeneous Electron Gas." *Phys. Rev.* **136**, B864 (1964).

[45] W. Kohn and L. J. Sham, "Self-Consistent Equations Including Exchange and Correlation Effects." *Phys. Rev.* **140**, A1133 (1965).

[46] J. P. Perdew and K. Schmidt, "Jacob's ladder of density functional approximations for the exchange-correlation energy." *AIP Conf. Proc.* **5771**, 154104 (2001).

[47] J. P. Perdew, A. Ruzsinszky, J. Tao, V. N. Staroverov, and G. E. Scuseria, "Prescription for the design and selection of density functional approximations: More constraint satisfaction with fewer fits." *J. Chem. Phys. J. Chem. Phys* **123**, 62201 (2005).

[48] M. Marsman, J. Paier, A. Stroppa, and G. Kresse, "Hybrid functionals applied to extended systems." *J. Phys. Condens. Matter* **20**, 064201 (2008).

[49] G. Kresse and D. Joubert, "From ultrasoft pseudopotentials to the projector augmented-wave method." *Phys. Rev. B* **59**, 1758 (1999).

[50] J. P. Perdew, W. Yang, K. Burke, Z. Yang, E. K. U. Gross, M. Scheffler, G. E. Scuseria, T. M. Henderson, I. Y. Zhang, A. Ruzsinszky, H. Peng, J. Sun, E. Trushin, and A. Görling, "Understanding band gaps of solids in generalized KohnSham theory." *Proc. Natl. Acad. Sci.* **114**, 2801 (2017).

[51] M. Gerosa, C. E. Bottani, C. Di Valentin, G. Onida, and G. Pacchioni, "Accuracy of dielectric-dependent hybrid functionals in the prediction of optoelectronic properties of metal oxide semiconductors: a comprehensive comparison with many-body GW and experiments." *J. Phys. Condens. Matter* **30**, 044003 (2018).

[52] J. Heyd, G. E. Scuseria, and M. Ernzerhof, "Hybrid functionals based on a screened Coulomb potential." *J. Chem. Phys.* **118**, 8207 (2003).

[53] J. Heyd, G. E. Scuseria, and M. Ernzerhof, "Erratum: Hybrid functionals based on a screened Coulomb potential [J. Chem. Phys. 118, 8207 (2003)]." *J. Chem. Phys.* **124**, 219906 (2006).

[54] J. Perdew, K. Burke, and M. Ernzerhof, "Generalized Gradient Approximation Made Simple." *Phys. Rev. Lett.* **77**, 3865 (1996).

[55] P. E. Blöchl, "Projector augmented-wave method." *Phys. Rev. B* **50**, 17953 (1994).

[56] N. A. W. Holzwarth, G. E. Matthews, R. B. Dunning, A. R. Tackett, and Y. Zeng, "Comparison of the projector augmented-wave, pseudopotential, and linearized augmented-plane-wave formalisms for density-functional calculations of solids." *Phys. Rev. B* **55**, 2005 (1997).

[57] C. Freysoldt, J. Neugebauer, and C. G. Van de Walle, "Fully Ab Initio Finite-Size Corrections for Charged-Defect Supercell Calculations." *Phys. Rev. Lett.* **102**, 016402 (2009).

[58] C. Freysoldt, B. Grabowski, T. Hickel, J. Neugebauer, G. Kresse, A. Janotti, and C. G. Van de Walle, "First-principles calculations for point defects in solids." *Rev. Mod. Phys.* **86**, 253 (2014).

[59] G. H. Wannier, "The Structure of Electronic Excitation Levels in Insulating Crystals." *Phys. Rev.* **52**, 191 (1937).

[60] N. Marzari and D. Vanderbilt, "Maximally-localized generalized Wannier functions for composite energy bands." *Phys. Rev. B* **56**, 12847 (1997).

[61] I. Souza, N. Marzari, and D. Vanderbilt, "Maximally-localized Wannier functions for entangled energy bands." *Phys. Rev. B* **65**, 13 (2001).

[62] A. A. Mostofi, J. R. Yates, G. Pizzi, Y.-S. Lee, I. Souza, D. Vanderbilt, and N. Marzari, "An updated version of wannier90: A tool for obtaining maximally-localised Wannier functions." *Comput. Phys. Commun.* **185**, 2309 (2014).

[63] N. Marzari, A. A. Mostofi, J. R. Yates, I. Souza, and D. Vanderbilt, "Maximally localized Wannier functions: Theory and applications." *Rev. Mod. Phys.* **84**, 1419 (2012).

[64] R. LeSar, *Introduction to computational materials science : fundamentals to applications*. Cambridge University Press, New York (2013).

[65] M. P. Allen, "Introduction to Molecular Dynamics Simulation." *Comput. Soft Matter From Synth. Polym. to Proteins* **23**, 1 (2004).

[66] W. C. Swope, H. C. Andersen, P. H. Berens, and K. R. Wilson, "A computer simulation method for the calculation of equilibrium constants for the formation of physical clusters of molecules: Application to small water clusters." *J. Chem. Phys.* **76**, 637 (1982).

[67] H. J. C. Berendsen, J. P. M. Postma, W. F. Van Gunsteren, A. DiNola, and J. R. Haak, "Molecular dynamics with coupling to an external bath." *J. Chem. Phys.* **81**, 3684 (1984).

[68] H. C. Andersen, "Molecular dynamics simulations at constant pressure and/or temperature." *J. Chem. Phys.* **72**, 2384 (1980).

[69] S. Nosé, "A unified formulation of the constant temperature molecular dynamics methods." *J. Chem. Phys.* **81**, 511 (1984).

[70] W. G. Hoover, "Canonical dynamics: Equilibrium phase-space distributions." *Phys. Rev. A* **31**, 1695 (1985).

[71] P. H. Hünenberger, "Thermostat Algorithms for Molecular Dynamics Simulations." "Adv. Polym. Sci," volume 173, 105–149 (2005).

[72] D. J. Evans and B. L. Holian, "The Nose-Hoover thermostat." *J. Chem. Phys.* **83**, 4069 (1985).

[73] C. R. Sweet, *Hamiltonian Thermostatting Techniques for Molecular Dynamics Simulation*. Ph.D. thesis, University of Leicester (2004).

[74] R. Car and M. Parrinello, "Unified Approach for Molecular Dynamics and Density-Functional Theory." *Phys. Rev. Lett.* **55**, 2471 (1985).

[75] G. Kresse and J. Furthmüller, "Efficient iterative schemes for *ab initio* total-energy calculations using a plane-wave basis set." *Phys. Rev. B* **54**, 11169 (1996).

[76] P. Giannozzi, S. Baroni, N. Bonini, M. Calandra, R. Car, C. Cavazzoni, D. Ceresoli, G. L. Chiarotti, M. Cococcioni, I. Dabo, A. Dal Corso, S. de Gironcoli, S. Fabris, G. Fratesi, R. Gebauer, U. Gerstmann, C. Gougoussis, A. Kokalj, M. Lazzeri, L. Martin-Samos, N. Marzari, F. Mauri, R. Mazzarello, S. Paolini, A. Pasquarello, L. Paulatto, C. Sbraccia, S. Scandolo, G. Sclauzero, A. P. Seitsonen, A. Smogunov, P. Umari, and R. M. Wentzcovitch, "QUANTUM ESPRESSO: a modular and open-source software project for quantum simulations of materials." *J. Phys. Condens. Matter* **21**, 395502 (2009).

[77] J. Ziman, *Electrons and phonons: The Theory of Transport Phenomena in Solids*. Oxford University Press (1967).

[78] W. A. Harrison, *Solid State Theory*. Dover Publications (1979).

[79] D. Emin, *Polarons*. Cambridge University Press (2013).

[80] D. Emin, "Small polarons." *Phys. Today* **35**, 34 (1982).

[81] A. Janotti, C. Franchini, J. B. Varley, G. Kresse, and C. G. Van de Walle, "Dual behavior of excess electrons in rutile TiO_2." *Phys. Status Solidi - Rapid Res. Lett.* **7**, 199 (2013).

[82] S. Baroni, S. de Gironcoli, A. Dal Corso, and P. Giannozzi, "Phonons and related crystal properties from density-functional perturbation theory." *Rev. Mod. Phys.* **73**, 515 (2001).

[83] M. Dresselhaus, "Applications of Group Theory to the Physics of Solids." (2002).

[84] X. Gonze and C. Lee, "Dynamical matrices, Born effective charges, dielectric permittivity tensors, and interatomic force constants from density-functional perturbation theory." *Phys. Rev. B* **55**, 355 (1997).

[85] N. Mounet, *Structural, vibrational and thermodynamic properties of carbon allotropes from first-principles: diamond, graphite, and nanotubes*. Ph.D. thesis, Massachusetts Institute of Technology (2005).

[86] H. Frölich, "Electrons in Lattice Fields." *Adv. Phys.* **3**, 325 (1954).

[87] K. Krishnaswamy, L. Bjaalie, B. Himmetoglu, A. Janotti, L. Gordon, and C. G. Van de Walle, "$BaSnO_3$ as a channel material in perovskite oxide heterostructures." *Appl. Phys. Lett.* **108**, 083501 (2016).

[88] S. Poncé, E. R. Margine, C. Verdi, and F. Giustino, "EPW: Electronphonon coupling, transport and superconducting properties using maximally localized Wannier functions." *Comput. Phys. Commun.* **209**, 116 (2016).

[89] P. Vogl, "Microscopic theory of electron-phonon interaction in insulators or semiconductors." *Phys. Rev. B* **13**, 694 (1976).

[90] J. Sjakste, N. Vast, M. Calandra, and F. Mauri, "Wannier interpolation of the electron-phonon matrix elements in polar semiconductors: Polar-optical coupling in GaAs." *Phys. Rev. B* **92**, 054307 (2015).

[91] C. Verdi and G. Giustino, "Frölich Electron-Phonon Vertex from First Principles." *Phys. Rev. Lett.* **115**, 176401 (2015).

[92] H. Peelaers, E. Kioupakis, and C. G. Van de Walle, "Free-carrier absorption in transparent conducting oxides: Phonon and impurity scattering in SnO_2." *Phys. Rev. B* **92**, 235201 (2015).

[93] E. Kioupakis, P. Rinke, A. Schleife, F. Bechstedt, and C. G. Van de Walle, "Free-carrier absorption in nitrides from first principles." *Phys. Rev. B* **81**, 241201 (2010).

[94] B. Himmetoglu, A. Janotti, H. Peelaers, A. Alkauskas, and C. G. Van de Walle, "First-principles study of the mobility of $SrTiO_3$." *Phys. Rev. B* **90**, 241204(R) (2014).

[95] B. Himmetoglu and A. Janotti, "Transport properties of $KTaO_3$ from first-principles." *J. Phys. Condens. Matter* **065502**, 65502 (2015).

[96] K. Krishnaswamy, B. Himmetoglu, Y. Kang, A. Janotti, and C. G. Van de Walle, "First-principles analysis of electron transport in $BaSnO_3$." *Phys. Rev. B* **95**, 205202 (2017).

[97] Y. Kang, K. Krishnaswamy, H. Peelaers, and C. G. Van de Walle, "Fundamental limits on the electron mobility of β-Ga_2 O_3." *J. Phys. Condens. Matter* **29**, 234001 (2017).

[98] F. Giustino, "Electron-phonon interactions from first principles." *Rev. Mod. Phys.* **89**, 015003 (2017).

[99] H. Kroemer, *Quantum Mechanic For Engineering: Materials Science and Applied Physics*. Prentice Hall, Englewood Cliffs, NJ (1994).

[100] H. Smith and H. H. Jensen, *Transport phenomena*. Clarendon Press (1989).

[101] A. Dal Corso and A. M. Conte, "Spin-orbit coupling with ultrasoft pseudopotentials: Application to Au and Pt." *Phys. Rev. B* **71**, 1 (2005).

[102] G. K. Madsen and D. J. Singh, "BoltzTraP. A code for calculating band-structure dependent quantities." *Comput. Phys. Commun.* **175**, 67 (2006).

[103] J.-J. Zhou and M. Bernardi, "Ab initio electron mobility and polar phonon scattering in GaAs." *Phys. Rev. B* **94**, 201201 (2016).

[104] J. Zhou, B. Liao, and G. Chen, "First-principles calculations of thermal, electrical, and thermoelectric transport properties of semiconductors." *Semicond. Sci. Technol* **31**, 043001 (2016).

[105] T.-H. Liu, J. Zhou, B. Liao, D. J. Singh, and G. Chen, "First-principles mode-by-mode analysis for electron-phonon scattering channels and mean free path spectra in GaAs." *Phys. Rev. B* **95**, 075206 (2017).

[106] M. S. Dresselhaus, "Solid State Physics Part II Optical Properties of Solids." (1999).

[107] M. Gajdoš, K. Hummer, G. Kresse, J. Furthmüller, and F. Bechstedt, "Linear optical properties in the projector-augmented wave methodology." *Phys. Rev. B* **73**, 1 (2006).

[108] F. Bassani and G. Pastori Parravicini, *Electronic States and Optical Transitions in Solids*. Pergamon, New York (1975).

[109] B. K. Ridley, *Quantum Processes in Semiconductors*. Oxford University Press, 3rd edition (1993).

[110] H. Peelaers and C. G. Van de Walle, "Sub-band-gap absorption in Ga_2O_3." *Appl. Phys. Lett.* **111**, 182104 (2017).

[111] B. Kusse and E. Westwig, *Mathematical physics : applied mathematics for scientists and engineers*. Wiley-VCH (2006).

[112] J. R. Yates, X. Wang, D. Vanderbilt, and I. Souza, "Spectral and Fermi surface properties from Wannier interpolation." *Phys. Rev. B* **75**, 195121 (2007).

[113] X. Wang, J. R. Yates, I. Souza, and D. Vanderbilt, "Ab initio calculation of the anomalous Hall conductivity by Wannier interpolation." *Phys. Rev. B* **74**, 195118 (2006).

[114] D. J. Griffiths, *Introduction to quantum mechanics*. Pearson Prentice Hall (2005).

[115] J. J. Sakurai and J. Napolitano, *Modern Quantum Mechanics*. Addison-Wesley, Pearson, San Francisco, 2nd edition (2014).

[116] W. Wang, A. Janotti, and C. G. Van de Walle, "Role of oxygen vacancies in crystalline WO_3." *J. Mater. Chem. C* **4**, 6641 (2016).

[117] W. Wang, H. Peelaers, J.-X. Shen, A. Janotti, and C. G. Van de Walle, "Impact of point defects on electrochromism in WO_3." F. H. Teherani, D. C. Look, and D. J. Rogers (eds.), "Oxide-based Mater. Devices IX," volume 120, 103, SPIE (2018).

[118] Y. Chen, N. Pryds, J. E. Kleibeuker, G. Koster, J. Sun, E. Stamate, B. Shen, G. Rijnders, and S. Linderoth, "Metallic and Insulating Interfaces of Amorphous $SrTiO_3$-Based Oxide Heterostructures." *Nano Lett.* **11**, 3774 (2011).

[119] C. Freysoldt, J. Neugebauer, and C. G. Van de Walle, "Electrostatic interactions between charged defects in supercells." *Phys. Status Solidi B* **248**, 1067 (2011).

[120] A. D. Mah, "The Heats of Formation of Tungsten Trioxide and Tungsten Dioxide." *J. Am. Chem. Soc.* **81**, 1582 (1959).

[121] J. G. Allpress, R. J. D. Tilley, and M. J. Sienko, "Examination of substoichiometric WO_{3-x} crystals by electron microscopy." *J. Solid State Chem.* **3**, 440 (1971).

[122] J. M. Berak and M. J. Sienko, "Effect of oxygen-deficiency on electrical transport properties of tungsten trioxide crystals." *J. Solid State Chem.* **2**, 109 (1970).

[123] L. Berggren, *Optical Absorption and Electrical Conductivity in Lithium Intercalated Amorphous Tunsten Oxide Films*. Ph.D. thesis, Uppsala University (2004).

[124] S.-H. Lee, H. M. Cheong, C. E. Tracy, A. Mascarenhas, A. W. Czanderna, and S. K. Deb, "Electrochromic coloration efficiency of a-WO_{3-y} thin films as a function of oxygen deficiency." *Appl. Phys. Lett.* **75**, 1541 (1999).

[125] S. K. Deb, "Opportunities and challenges in science and technology of WO_3 for electrochromic and related applications." *Sol. Energy Mater. Sol. Cells* **92**, 245 (2008).

[126] R. Chatten, A. V. Chadwick, A. Rougier, and P. J. D. Lindan, "The oxygen vacancy in crystal phases of WO_3." *J. Phys. Chem. B* **109**, 3146 (2005).

[127] E. Iguchi and H. Miyagi, "A study on the stability of polarons in monoclinic WO_3." *J. Phys. Chem. Solids* **54**, 403 (1993).

[128] G. Hoppmann and E. Salje, "Optical and Electrical Properties of H^+ Doped WO_3 Single Crystals." *Phys. Status Solidi B* **37**, K187 (1976).

[129] M. B. Johansson, B. Zietz, G. A. Niklasson, and L. Österlund, "Optical properties of nanocrystalline WO_3 and WO_{3-x} thin films prepared by DC magnetron sputtering." *J. Appl. Phys.* **115**, 213510 (2014).

[130] F. Wang, C. Di Valentin, and G. Pacchioni, "Semiconductor-to-metal transition in WO_{3-x}: Nature of the oxygen vacancy." *Phys. Rev. B* **84**, 073103 (2011).

[131] D. B. Migas, V. L. Shaposhnikov, V. N. Rodin, and V. E. Borisenko, "Tungsten oxides. I. Effects of oxygen vacancies and doping on electronic and optical properties of different phases of WO_3." *J. Appl. Phys.* **108**, 093713 (2010).

[132] S. Z. Karazhanov, Y. Zhang, A. Mascarenhas, S. Deb, and L.-W. Wang, "Oxygen vacancy in cubic WO_3 studied by first-principles pseudopotential calculation." *Solid State Ionics* **165**, 43 (2003).

[133] C. Lambert-Mauriat and V. Oison, "Density-functional study of oxygen vacancies in monoclinic tungsten oxide." *J. Phys. Condens. Matter* **18**, 7361 (2006).

[134] W. Setyawan and S. Curtarolo, "High-throughput electronic band structure calculations: Challenges and tools." *Comput. Mater. Sci.* **49**, 299 (2010).

[135] H. R. Shanks, P. H. Sidles, and G. C. Danielson, "Electrical Properties of the Tungsten Bronzes." *Adv. Chem.* **39**, 237 (1963).

[136] S. Kück and H. Werheit, "Supplement to Vol. III/17g (Print Version) Revised and Updated Edition of Vol. III/17g (CD-ROM)." O. Madelung (ed.), "Non-Tetrahedrally Bond. Bin. Compd. II," 535, Springer (2000).

[137] O. F. Schirmer and E. Salje, "The W^{5+} polaron in crystalline low temperature WO_3 ESR and optical absorption." *Solid State Commun.* **33**, 333 (1980).

[138] M. F. Saenger, T. Höing, B. W. Robertson, R. B. Billa, T. Hofmann, E. Schubert, and M. Schubert, "Polaron and phonon properties in proton intercalated amorphous tungsten oxide thin films." *Phys. Rev. B* **78**, 245205 (2008).

[139] M. A. Butler, "Photoelectrolysis and Physical Properties of the Semiconducting Electrode WO_3." *J. Appl. Phys.* **48**, 1914 (1977).

[140] J. Kleperis, J. Zubkans, and A. R. Lusis, "The nature of fundamental absorption edge of WO_3." E. A. Silinsh, A. Medvids, A. R. Lusis, and A. O. Ozols (eds.), "Proc. SPIE 2968, Opt. Org. Semicond. Inorg. Mater.", volume 2968, 186–191 (1997).

[141] P. P. González-Borrero, F. Sato, A. N. Medina, M. L. Baesso, A. C. Bento, G. Baldissera, C. Persson, G. A. Niklasson, C. G. Granqvist, and A. Ferreira da Silva, "Optical band-gap determination of nanostructured WO_3 film." *Appl. Phys. Lett.* **96**, 061909 (2010).

[142] G. A. de Wijs and R. A. de Groot, "Structure and electronic properties of amorphous WO_3." *Phys. Rev. B* **60**, 16463 (1999).

[143] J. Paier, M. Marsman, and G. Kresse, "Why does the B3LYP hybrid functional fail for metals?" *J. Chem. Phys.* **127**, 024103 (2007).

[144] H. Peelaers and C. G. Van de Walle, "First-principles study of van der Waals interactions in MoS_2 and MoO_3." *J. Phys. Condens. Matter* **26**, 305502 (2014).

[145] H. Ding, H. Lin, B. Sadigh, F. Zhou, V. Ozoliņš, and M. Asta, "Computational investigation of electron small polarons in α-MoO_3." *J. Phys. Chem. C* **118**, 15565 (2014).

[146] S. H. Lee, M. J. Seong, H. M. Cheong, E. Ozkan, E. C. Tracy, and S. K. Deb, "Effect of crystallinity on electrochromic mechanism of Li_xWO_3 thin films." *Solid State Ionics* **156**, 447 (2003).

[147] O. F. Schirmer, V. Wittwer, G. Baur, and G. Brandt, "Dependence of WO_3 Electrochromic Absorption on Crystallinity." *J. Electrochem. Soc. Solid-State Sci. Technol.* **124**, 749 (1977).

[148] R. B. Goldner, D. H. Mendelsohn, J. Alexander, W. R. Henderson, D. Fitzpatrick, T. E. Haas, H. H. Sample, R. D. Rauh, M. A. Parker, and T. L. Rose, "High near-infrared reflectivity modulation with polycrystalline electrochromic WO_3 films." *Appl. Phys. Lett.* **43**, 1093 (1983).

[149] R. B. Goldner, P. Norton, K. Wong, G. Foley, E. L. Goldner, G. Seward, and R. Chapman, "Further evidence for free electrons as dominating the behavior of electrochromic polycrystalline WO_3 films." *Appl. Phys. Lett.* **47**, 536 (1985).

[150] D. H. Mendelsohn and R. B. Goldner, "Ellipsometry Measurements as Direct Evidence of the Drude Model for Polycrystalline Electrochromic WO_3 Films." *J. Electrochem. Soc.* **131**, 857 (1984).

[151] M. V. Limaye, J. S. Chen, S. B. Singh, Y. C. Shao, Y. F. Wang, C. W. Pao, H. M. Tsai, J. F. Lee, H. J. Lin, J. W. Chiou, M. C. Yang, W. T. Wu, J. J. Wu, M. H. Tsai, and W. F. Pong, "Correlation between electrochromism and electronic structures of tungsten oxide films." *RSC Adv.* **4**, 5036 (2014).

[152] S. Hashimoto and H. Matsuoka, "Mechanism of electrochromism for amorphous WO_3 thin films." *J. Appl. Phys.* **69**, 933 (1991).

[153] L. Berggren, A. Azens, and G. A. Niklasson, "Polaron absorption in amorphous tungsten oxide films." *J. Appl. Phys.* **90**, 1860 (2001).

[154] F. Di Quarto, A. Di Paola, and C. Sunseri, "Semiconducting properties of anodic WO3 amorphous films." *Electrochim. Acta* **26**, 1177 (1981).

[155] S. K. Deb, "Optical and photoelectric properties and colour centres in thin films of tungsten oxide." *Philos. Mag.* **27**, 801 (1973).

[156] W. Wang, A. Janotti, and C. G. Van de Walle, "Phase transformations upon doping in WO_3." *J. Chem. Phys.* **146**, 214504 (2017).

[157] R. Clarke, "New Sequence of Structural Phase Transitions in Na_xWO_3." *Phys. Rev. Lett.* **39**, 1550 (1977).

[158] Z. Li, S. Wu, Z. Wang, and Y. Fu, "Doping Induced Structural Transformation in Tungsten Trioxide." *J. Alloys Compd.* **672**, 155 (2016).

[159] Z. Wang, Y. He, M. Gu, Y. Du, S. X. Mao, and C. Wang, "Electron Transfer Governed Crystal Transformation of Tungsten Trioxide upon Li Ions Intercalation." *ACS Appl. Mater. Interfaces* **8**, 24567 (2016).

[160] F. Corà, M. G. Stachiotti, C. R. A. Catlow, and C. O. Rodriguez, "Transition Metal Oxide Chemistry: Electronic Structure Study of WO_3 , ReO_3 , and $NaWO_3$." *J. Phys. Chem. B* **101**, 3945 (1997).

[161] S. Tosoni, C. Di Valentin, and G. Pacchioni, "Effect of Alkali Metals Interstitial Doping on Structural and Electronic Properties of WO_3." *J. Phys. Chem. C* **118**, 3000 (2014).

[162] A. Walkingshaw, N. Spaldin, and E. Artacho, "Density-functional study of charge doping in WO_3." *Phys. Rev. B* **70**, 165110 (2004).

[163] R. Egdell and M. Hill, "Investigation of the fermi edge in sodium tungsten bronzes by photoelectron spectroscopy." *Chem. Phys. Lett.* **85**, 140 (1982).

[164] K. Robinson, G. V. Gibbs, and P. H. Ribbe, "Quadratic Elongation: A Quantitative Measure of Distortion in Coordination Polyhedra." *Science (80-.).* **172**, 567 (1971).

[165] C. G. Van de Walle and R. M. Martin, "Theoretical calculations of heterojunction discontinuities in the Si/Ge system." *Phys. Rev. B* **34**, 5621 (1986).

[166] J. Paier, M. Marsman, K. Hummer, G. Kresse, I. C. Gerber, and J. G. Ángyán, "Screened hybrid density functionals applied to solids." *J. Chem. Phys.* **124**, 154709 (2006).

[167] R.-T. Wen, C. G. Granqvist, and G. A. Niklasson, "Eliminating degradation and uncovering ion-trapping dynamics in electrochromic WO_3 thin films." *Nat. Mater.* **14**, 996 (2015).

[168] Y. Du, M. Gu, T. Varga, C. Wang, M. E. Bowden, and S. A. Chambers, "Strain Accommodation by Facile WO_6 Octahedral Distortion and Tilting during WO_3 Heteroepitaxy on $SrTiO_3$ (001)." *ACS Appl. Mater. Interfaces* **6**, 14253 (2014).

[169] A. Garg and Z. H. Leake, J ABarber, "Epitaxial growth of WO_3 films on $SrTiO_3$ and sapphire." *J. Phys. D. Appl. Phys.* **33**, 1048 (2000).

[170] F. Giustino, M. L. Cohen, and S. G. Louie, "Electron-phonon interaction using Wannier functions." *Phys. Rev. B* **76**, 165108 (2007).

[171] J. Son, P. Moetakef, B. Jalan, O. Bierwagen, N. J. Wright, R. Engel-Herbert, and S. Stemmer, "Epitaxial $SrTiO_3$ films with electron mobilities exceeding 30,000 cm^2 $V^{-1}s^{-1}$." *Nat. Mater.* **9**, 482 (2010).

[172] N. Troullier and J. L. Martins, "Efficient pseudopotentials for plane-wave calculations." *Phys. Rev. B* **43**, 1993 (1991).

[173] M. S. Dresselhaus, G. Dresselhaus, and A. Jorio, *Group Theory: Applications to the Physics of Condensed Matter*. Springer-Verlag, Berlin (2008).

[174] J. L. Servoin, Y. Luspin, and F. Gervais, "Infrared dispersion in $SrTiO_3$ at high temperature." *Phys. Rev. B* **22**, 5501 (1980).

[175] W. G. Stirling and R. Currat, "Experimental verification of the phonon dispersion curves of strontium titanate." *J. Phys. C Solid State Phys.* **9**, L519 (1976).

[176] W. G. Spitzer, R. C. Miller, D. A. Kleinman, and L. E. Howarth, "Far Infrared Dielectric Dispersion in $BaTiO_3$, $SrTiO_3$, and TiO_2." *Phys. Rev.* **126**, 1710 (1962).

[177] A. Janotti, D. Steiauf, and C. G. Van de Walle, "Strain effects on the electronic structure of $SrTiO_3$: Toward high electron mobilities." *Phys. Rev. B* **84**, 201304 (2011).

[178] M. Marques, L. K. Teles, V. Anjos, L. M. R. Scolfaro, J. R. Leite, V. N. Freire, G. A. Farias, and E. F. da Silva, "Full-relativistic calculations of the $SrTiO_3$ carrier effective masses and complex dielectric function." *Appl. Phys. Lett.* **82**, 3074 (2003).

[179] B. Ingham, S. Hendy, S. Chong, and J. Tallon, "Density-functional studies of tungsten trioxide, tungsten bronzes, and related systems." *Phys. Rev. B* **72**, 075109 (2005).

[180] Y. Xue, Y. Zhang, and P. Zhang, "Theory of the color change of Na_xWO_3 as a function of Na-charge doping." *Phys. Rev. B* **79**, 205113 (2009).

[181] A. Deneuville and P. Gerard, "Influence of Substoichiometry, hydrogen content and crystallinity on the optical and electrical properties of H_xWO_y thin films." *J. Electron. Mater.* **7**, 559 (1978).

[182] L. Berggren, J. Ederth, and G. A. Niklasson, "Electrical conductivity as a function of temperature in amorphous lithium tungsten oxide." *Sol. Energy Mater. Sol. Cells* **84**, 329 (2004).

[183] Y. Ping, D. Rocca, and G. Galli, "Optical properties of tungsten trioxide from first-principles calculations." *Phys. Rev. B* **87**, 165203 (2013).

[184] H. Peelaers, E. Kioupakis, and C. G. Van de Walle, "Fundamental limits on optical transparency of transparent conducting oxides: Free-carrier absorption in SnO_2." *Appl. Phys. Lett.* **100**, 011914 (2012).

[185] D. Lynch, R. Rosei, J. Weaver, and C. Olson, "The optical properties of some alkali metal tungsten bronzes from 0.1 to 38 eV." *J. Solid State Chem.* **8**, 242 (1973).

[186] J. F. Owen, K. J. Teegarden, and H. R. Shanks, "Optical properties of the sodium-tungsten bronzes and tungsten trioxide." *Phyiscal Rev. B* **18**, 3827 (1978).

[187] C. Yang, J.-F. Chen, X. Zeng, D. Cheng, and D. Cao, "Design of the Alkali-Metal-Doped WO_3 as a Near-Infrared Shielding Material for Smart Window." *Ind. Eng. Chemsitry Res.* **53**, 17981 (2014).

[188] A. M. Brown, R. Sundararaman, P. Narang, W. A. Goddard Iii, and H. A. Atwater, "Nonradiative Plasmon Decay and Hot Carrier Dynamics: Effects of Phonons, Surfaces, and Geometry." *ACS Nano* **10**, 957 (2016).

[189] S. James Allen, S. Raghavan, T. Schumann, K.-M. Law, and S. Stemmer, "Conduction band edge effective mass of La-doped $BaSnO_3$." *Appl. Phys. Lett.* **108**, 252107 (2016).

[190] R. J. Mortimer, "Electrochromic Materials." *Annu. Rev. Mater. Res.* **41**, 241 (2011).

[191] S.-H. Lee, R. Deshpande, P. A. Parilla, K. M. Jones, B. To, A. H. Mahan, and A. C. Dillon, "Crystalline WO_3 nanoparticles for highly improved electrochromic applications." *Adv. Mater.* **18**, 763 (2006).

[192] N. Bondarenko, O. Eriksson, and N. V. Skorodumova, "Polaron mobility in oxygen-deficient and lithium-doped tungsten trioxide." *Phys. Rev. B* **92**, 165119 (2015).

[193] T. Smith and J. Guild, "The C.I.E. colorimetric standards and their use." *Trans. Opt. Soc.* **33**, 73 (1931).

[194] K. Cooper and C. Kazilek, "ASU- Ask a Biologist: Seeing color." (2010).

[195] R. U. Kirss and L. Meda, "Chemical vapor deposition of tungsten oxide." *Appl. Organomet. Chem.* **12**, 155 (1998).

[196] E. Lassner, W.-D. Schubert, E. Lüderitz, and H. U. Wolf, "Tungsten, Tungsten Alloys, and Tungsten Compounds." "Ullmann's Encycl. Ind. Chem.", 498–533, Wiley-VCH Verlag GmbH & Co. KGaA, Weinheim, Germany (2000).

[197] S. Dey, R. A. Ricciardo, H. L. Cuthbert, and P. M. Woodward, "Metal-to-Metal Charge Transfer in AWO_4 (A = Mg, Mn, Co, Ni, Cu, or Zn) Compounds with the Wolframite Structure." *Inorg. Chem.* **53**, 4394 (2014).

[198] F. Wang, C. Di Valentin, and G. Pacchioni, "Doping of WO_3 for Photocatalytic Water Splitting: Hints from Density Functional Theory." *J. Phys. Chem. C* **116**, 8901 (2012).

[199] T. Zhang, Z. Zhu, H. Chen, Y. Bai, S. Xiao, X. Zheng, Q. Xue, and S. Yang, "Iron-doping-enhanced photoelectrochemical water splitting performance of nanostructured WO_3: a combined experimental and theoretical study." *Nanoscale* **7**, 2933 (2015).

[200] M. Denk, D. Kuhness, M. Wagner, S. Surnev, F. R. Negreiros, L. Sementa, G. Barcaro, I. Vobornik, A. Fortunelli, and F. P. Netzer, "Metal Tungstates at the Ultimate Two-Dimensional Limit: Fabrication of a $CuWO_4$ Nanophase." *ACS Nano* **8**, 3947 (2014).

[201] S. M. Zawawi, R. Yahya, A. Hassan, H. N. M. E. Mahmud, and M. N. Daud, "Structural and optical characterization of metal tungstates (MWO_4; M=Ni, Ba, Bi) synthesized by a sucrose-templated method." *Chem. Cent. J.* **7**, 80 (2013).

[202] P. Rodríguez-Hernández, J. López-Solano, S. Radescu, A. Mujica, A. Muñoz, D. Errandonea, J. Pellicer-Porres, A. Segura, C. Ferrer-Roca, F. Manjón, R. Kumar, O. Tschauner, and G. Aquilanti, "Theoretical and experimental study of $CaWO_4$ and $SrWO_4$ under pressure." *J. Phys. Chem. Solids* **67**, 2164 (2006).

[203] T. J. Vink, E. P. Boonekamp, R. G. F. A. Verbeek, and Y. Tamminga, "Lithium trapping at excess oxygen in sputter-deposited *a*-WO_3 films." *J. Appl. Phys.* **85**, 1540 (1999).

[204] T. J. Knowles, "Optical regeneration of aged WO_3 electrochromic cells." *Appl. Phys. Lett.* **31**, 817 (1977).

[205] G. A. Niklasson and C. G. Granqvist, "Electrochromics for smart windows: thin films of tungsten oxide and nickel oxide, and devices based on these." *J. Mater. Chem.* **17**, 127 (2007).

[206] C.-G. Granqvist, "Electrochromic materials: Out of a niche." *Nat. Mater.* **5**, 89 (2006).